12-5-2014

Experimental Studies of Turbulent Local Extinction

Marc D. Schneider
University of Connecticut - Storrs, marc.schneider@uconn.edu

Experimental Studies of Turbulent Local Extinction

Marc Donald Schneider

B.S., University of Connecticut, 2013

A Thesis

Submitted in Partial Fulfillment of the

Requirements for the Degree of

Master of Science

At the

University of Connecticut

2014

APPROVAL PAGE

Master of Science Thesis

Experimental Studies of Turbulent Local Extinction

Presented by:

Marc D. Schneider, B.S.

Major Advisor: _____
Dr. Michael W. Renfro

Associate Advisor: _____
Dr. Baki M. Cetegen

Associate Advisor: _____
Dr. Tianfeng Lu

University of Connecticut
2014

Acknowledgements

I would like to acknowledge the NSF for the financial support for this research.

I would like to thank my major advisor, Dr. Michael Renfro for his excellent advising skills. Without him this research would not have been possible.

I would like to thank Dr. Baki Cetegen and Dr. Tianfeng Lu for serving on my committee.

I would like to thank my co-workers and lab mates past and present: Kathryn Gosselin, Chris Perron, Martin Hawron, Steven Grib, Nicholas Wixom, Josh Stoddard, and WeiLai Lu for their comic relief, excellent technical advice, and extra hands when I needed them.

To Dr. Steve Tuttle, I extend my eternal gratitude for writing a MATLAB interpretation of many non-linear diffusion filters.

I would like to express my undying gratitude to my parents and brother for being supportive throughout the process of pursuing higher education.

I would also like to thank Sophie for being my best friend, spirit guide, and source of endless hours of distraction.

Table of Contents

Abstract

In this study, a novel burner for the creation of a quasi-stationary extinction edge in a non-premixed flame sheet is presented. The design process of this burner is outlined and results are presented from laminar simulations using a commercial CFD code. Non-reacting simulations were performed for parametric analysis of the burner design using peak scalar dissipation rate downstream of flame stabilization as a design goal. Reacting simulations using a one-step methane-air mechanism were used to predict the existence of a negative flame edge. Particle Imaging Velocimetry (PIV) was used to quantify the boundary conditions and the flow field inside the burner. A novel technique for extracting chemiluminescence profiles from PIV image pairs is presented using the differing intensities of seed particles and chemiluminescence from images acquired without a laser line filter. This technique also uses non-linear spatial filtering to smooth the image and provide a flame edge. Statistics of flame position in the burner and velocities at the flame edge in both individual frames and the average flow field are presented. This thesis is intended to lay out a preliminary analysis of negative flame edges in turbulent flow, while making recommendations to expand the understanding of the turbulent local extinction process.

Chapter 1: Introduction

In the design of practical combustors, it is desirable to burn the fuel in such a manner that minimizes pollutant emissions and maximizes efficiency of the burning process. Operating a combustor under lean premixed conditions accomplishes these goals, yielding a shorter flame than under non-premixed conditions. These premixed conditions do have drawbacks, including flashback and acoustically driven oscillations inside the combustor leading to mechanical damage or flame extinction. Many of the benefits of the premixed flame can be observed in a non-premixed combustor if the mixing of the fuel and oxidizer is sufficiently rapid to create partially premixed conditions. In order to create these high mixing rates, strong gradients must be imposed in the flow field. These gradients include velocity gradients and species gradients. High vorticity and turbulence is inherent in these types of flows. When a flame sheet is exposed to large enough gradients, local extinction can occur (Rolon 1995). In many applications, this is undesirable and may lead to global flame extinction.

In non-premixed combustion, the reaction zone is located along a relatively thin sheet where the concentrations of fuel and oxidizer are equivalent in ratio to the stoichiometric mixture (*Figure1.1*). This sheet is relatively thin in both laminar and turbulent cases. If this sheet is exposed to high enough gradients, a hole will form in the sheet where the chemical reactions cease. This has been observed experimentally using simultaneous CH and OH planar induced laser fluorescence (PLIF) in experiments involving vortices interacting with diffusion flame sheets (Nguyen,1996). In addition, this has been observed numerically with a pair of counter-rotating vortices impinging on a laminar flame sheet (Favier and Vervisch 2001). The aforementioned flame holes can display a number of behaviors. The can grow in size and propagate throughout the flame sheet and cause global extinction, be convected downstream of the flame and have minimal effect on global flame stability, or the can heal and combustion will resume and a continuous sheet will be reformed. The behavior of the flame at the edge of the hole determines which behavior the hole will exhibit.

Flame holes consist of three types of edges (*Figure 1.2*). The most studied type of flame edge is the forwardly propagating flame edges (a) in which the edge is moving towards the interior of the hole relative to the flow velocity. This leads to a flow of unburned reactants into the flame edge. This type of edge commonly exhibits a 'triple flame' structure as observed experimentally(Kioni et al. 1993; Kĩoni et al. 1999)in a burner with a stoichiometry gradient at the inlet of a divergent section, and predicted numerically in a plane mixing layer(Im and Chen 1999)and in a round coflow jet burner(Xu and Smooke 1993). This type of edge can be readily observed in a 'lifted' jet flame and is fairly well understood. The second type of edge is the stationary edge (b). This edge has no flow of reactants or products through the edge. This was stabilized in an intentionally misaligned slot burner (Shay and Ronney 1998), but it is not of particular interest in this study. The final type of flame edge is the negatively propagating edge (c), which is characterized by a flow of hot products through the flame edge. This type of edge propagates away from the flame hole center, and tends to expand the hole. This type of edge is often transient, and difficult to analyze. This type of edge has been stabilized in an off-axis extinction point in a counterflow burner (Carnell and Renfro 2005)and in a 'twin slot' counterflow burner (Yang et al. 2009). Both of these burners operate under laminar conditions.

The full reaction pathways in the combustion of the simplest hydrocarbon fuels are complicated, and computationally expensive to simulate. A reduced order model that accurately predicts flame stabilization and extinction over a range of flow conditions and Reynolds numbers would greatly improve the design process, yielding more efficient and reliable combustors. This modeling requires detailed study of both extinction and ignition flame edges. In non-premixed combustion, a measure of species gradient, known as scalar dissipation rate, has been proposed as a key parameter governing extinction (Bilger, Stårner, and Kee 1990). Results from past study has shown that there is an effect of advective heat fluxes on the extinction scalar dissipation rate for extinction(Carnell and Renfro 2006), thus proving that a single one-dimensional extinction scalar dissipation rate alone is not sufficient to accurately predict flame extinction in all flows. Attempts to model extinction in highly complex turbulent flows have been made, usually using the flamelet model (Pitsch, Cha, and Fedotov 2003), which assumes the reaction is analogous to a laminar flame sheet. This has questionable validity under some conditions where the reaction zone may be larger than the smallest vortices in the flow(Li et al. 2010).

In order to fully validate the proposed turbulence-chemistry interaction models, as well as develop new models, detailed study of the conditions surrounding flame extinction is necessary. In prior work, detailed measurements have been taken in a counterflow geometry to characterize the conditions leading up to and post extinction. These include temperature profiles via Raman scattering (Carnell 2007) and formaldehyde (Carnell et al. 2009)and OH PLIF (Carnell and Renfro 2005) to determine reaction rate. These measurements were limited to laminar conditions. In order to perform the same type of detailed measurements in a turbulent flame, it is desirable to stabilize a turbulent extinction edge in a stationary region to facilitate laser diagnostics that require high spatial resolution. The stationary extinction zone presented in this work avoids the highly transient nature of the extinction phenomena, as the lifetime of a receding edge can be on the order of a few milliseconds until global extinction (Biswas et al. 2013). While the turbulent extinction presented here is not steady-state, it is statistically stationary, and occurs within a relatively small space (on the order of one centimeter), allowing more detailed analysis than previously performed on this type of turbulent phenomena.

In this thesis, a new burner to create a statistically stationary turbulent extinction edge is presented. This burner was designed using mainly non-reacting CFD and validated with a reacting simulation. Experimental data characterizing the inlet boundary conditions and velocity field in the region of the flame edge is presented. The velocity field is analyzed in conjunction with a chemiluminescence technique used to find the flame edge , , to provide a statistical representation of the edge speed. to. This edge speed as a function of scalar dissipation is important in the prediction of the temporal evolution of flame holes. This speed has not been quantitatively reported, as referenced in the literature review.

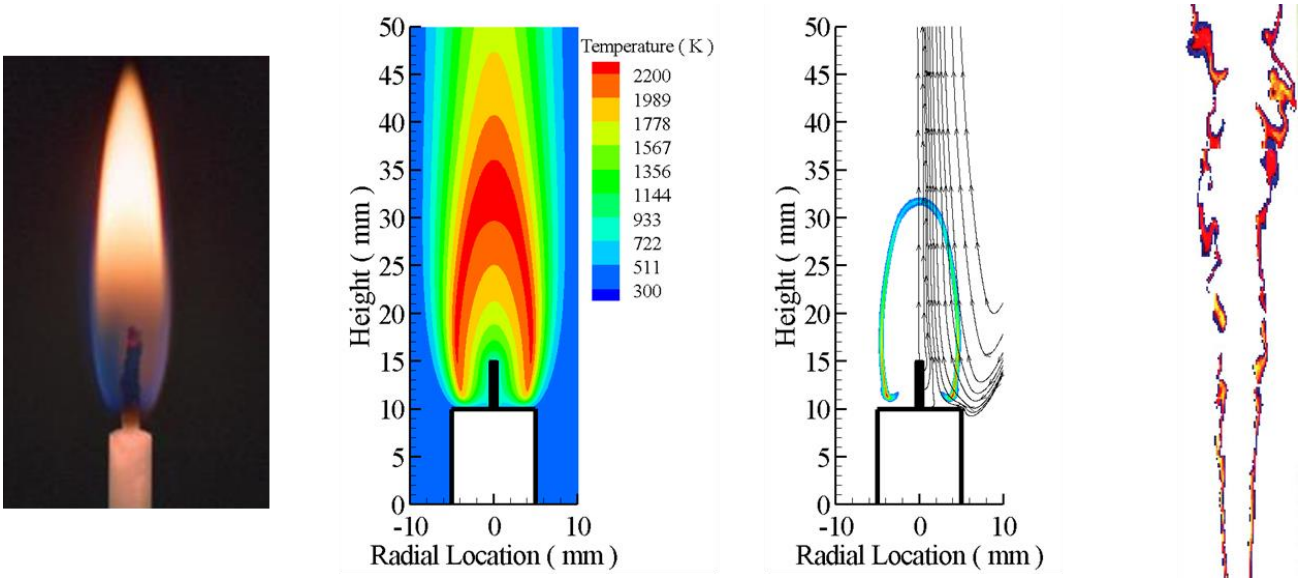

Figure 1.1 Depiction of a laminar diffusion flame (candle). First image on left is chemiluminescence and emission from soot, second is simulated temperature profile, third is heat release, showing the candle flame as a thin reaction layer. (Carnell 2006)*Right most image is OH PLIF image showing the thin reaction zone found in a turbulent jet flame* (Bergmann et al. 1998)

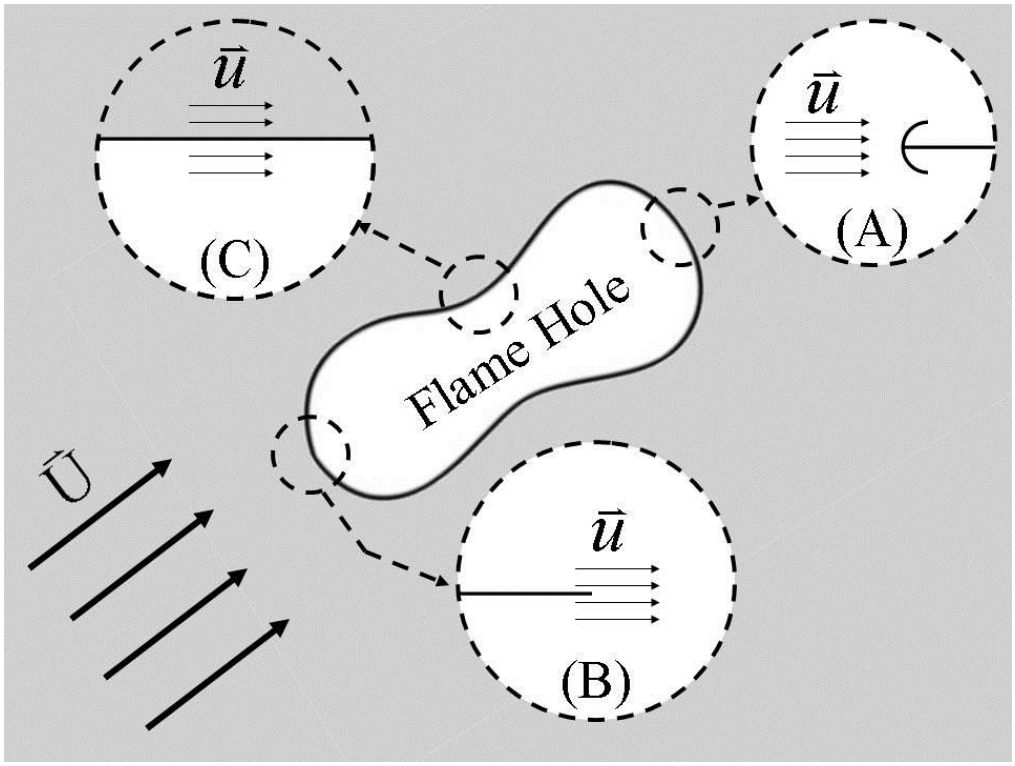

Figure 1.2 Hole in flame sheet showing forwardly propagating (A), retreating (B), and stationary (C) flame edges (Carnell 2006)

Chapter 2: Literature Review

Observations of Flame Holes in Turbulent Studies of Non-premixed Flames

In many turbulent experiments, flame holes have been observed. Unfortunately, due to the temporal resolution of the measurements, the formation and evolution of these holes is not well captured. In the work by Bergmann, breaks in the OH and CH layers of a turbulent jet diffusion flame consisting of methane, hydrogen, and nitrogen were observed (Bergmann et al. 1998). Also observed was a low temperature region in the shear layer via Rayleigh scattering (*Figure 2.1*). These images point to the existence of a flame hole. These measurements were not time resolved, and do no show the transient behavior of the flame edges.

The same type of flame sheet discontinuity was observed by Watson *et al.* in CH Planar Laser Induced Fluorescence (PLIF) images in a turbulent methane jet diffusion flame (*Figure 2.2*). (K. A. Watson et al. 1999)These images were overlaid with simultaneous Particle Imaging Velocimetry (PIV) results to characterize the flow field around the flame edge (*Figure 2.3*).However, because these measurements were not time resolved, the edge velocity was not determined, and it is uncertain if the edges are propagating forwardly or retreating. In addition, simultaneous OH and CH PLIF (*Figure 2.4*) were performed in order to compare the signals in the extinction region. This study found that both CH and OH are reasonable markers of flame edge in this flow. In other work, this group performed simultaneous Rayleigh thermometry showing vortex-flame interaction causing local extinction (*Figure 2.5*)

Measurements with higher temporal resolution were performed by Hult *et al.* in a high Reynolds number free jet composed of hydrogen, methane, and nitrogen (Hult et al. 2005). A stereoscopic PIV system was used to gather velocity data that corresponded to one frame of high speed OH PLIF. This PLIF was taken as a series of 6 shots at 33 kHz, with the PIV data corresponding to the 4^{th} PLIF frame. These results were overlaid, and provide additional insight into the temporal behavior of the flame holes (*Figure 2.6*). While this data represents an improvement in the understanding of flame hole resolution, the detailed structure of the edges of the holes is not resolved, and no edge velocities are reported.

Further progress was made by Boxx *et al.* in a lifted propane jet flame. Simultaneous high speed OH PLIF and stereoscopic PIV were applied with a repetition rate of 1.5 kHz (*Figure 2.7*) (Boxx et al. 2009). These measurements offer improvements in the interpretation of 2 dimensional laser measurements in highly 3 dimensional flows. The researchers determined that some observed flame edges result from out of plane velocity contributions convecting existing holes into the measurement plane. This shows that simple 2 dimensional measurements are insufficient to perform in-depth analysis of highly three dimensional flame structures.

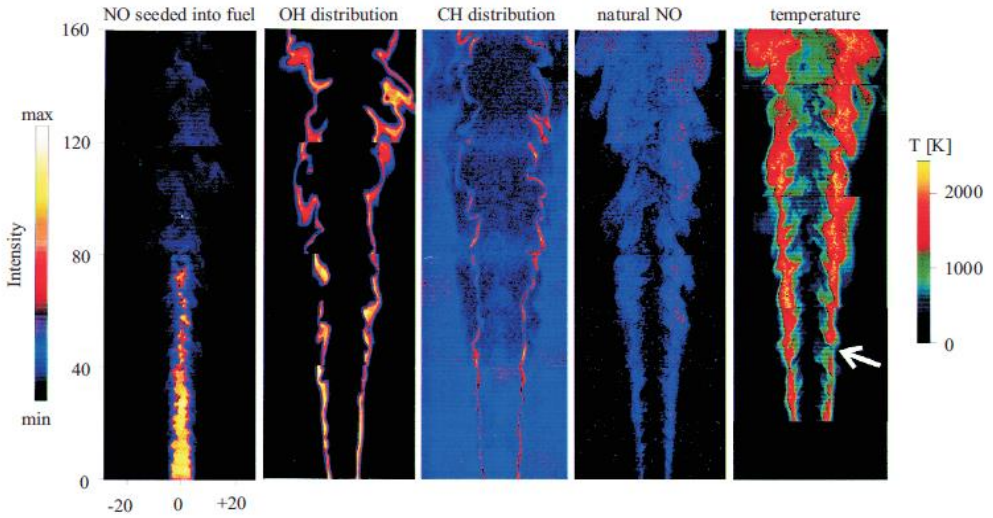

Figure 2.1 Breaks in the OH and CH PLIF images point to the existence of a flame hole. In the right most temperature image, a low temperature region is highlighted showing the existence of a flame hole. (Bergmann et al. 1998)

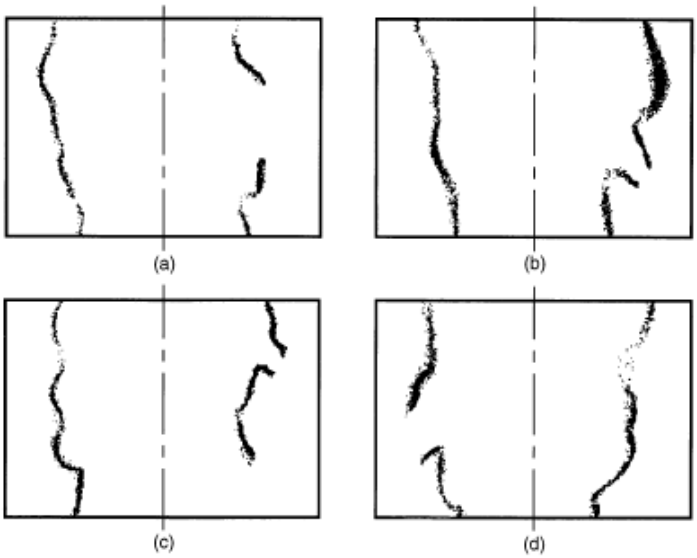

Figure 2.2 CH PLIF measurements showing flame holes in the flame sheet indicating local extinction in a lifted turbulent methane jet flame. (K. A. Watson et al. 1999)

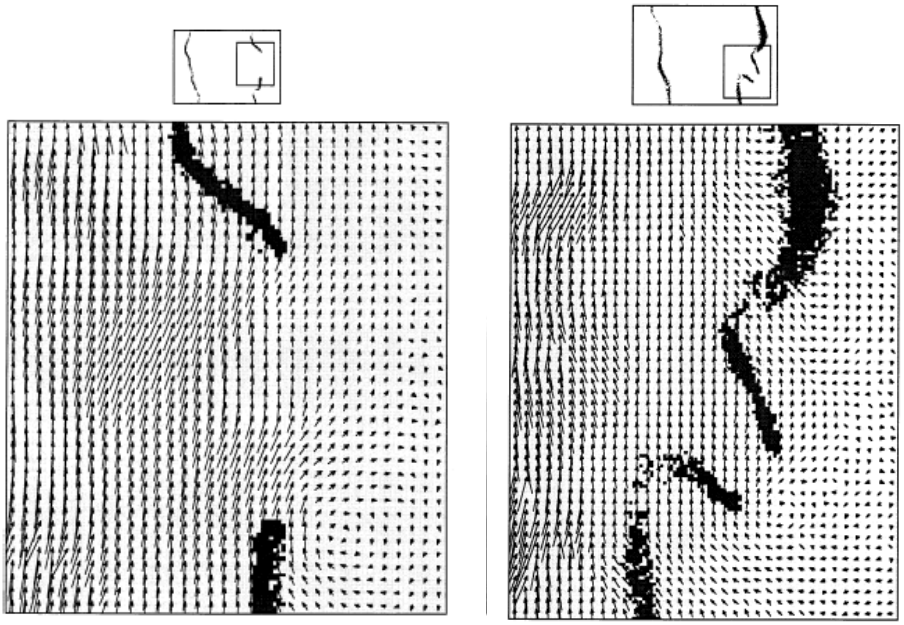

Figure 2.3 Overlaid CH PLIF and PIV Results from flame holes in the experiment of (K. A. Watson et al. 1999)

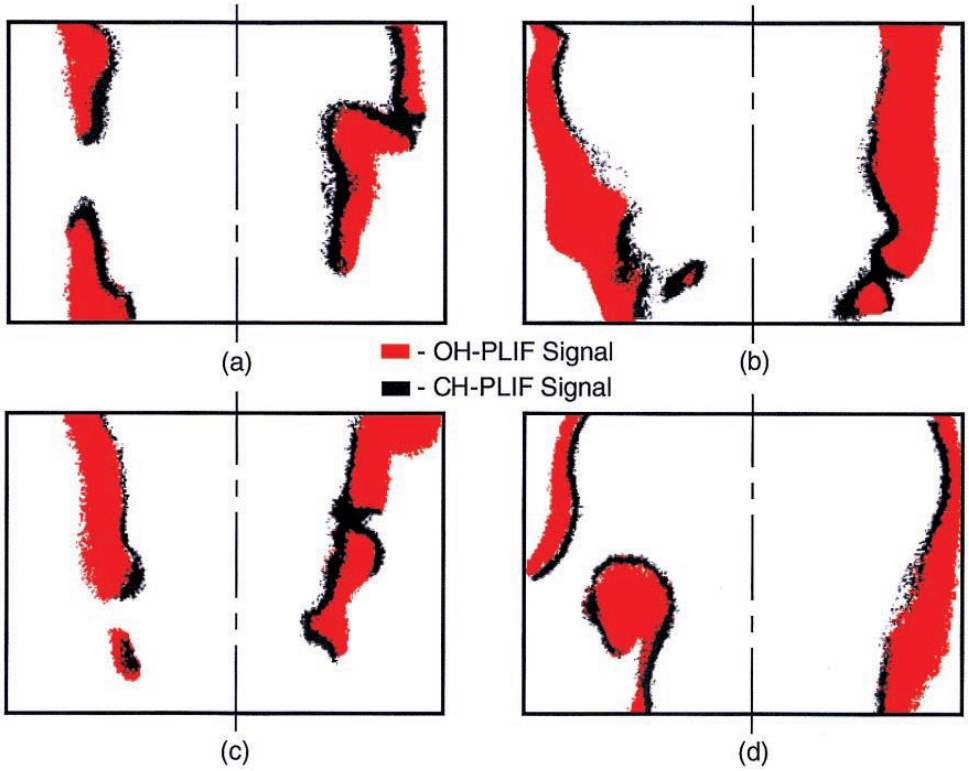

Figure 2.4 Simultaneous CH and OH PLIF signal from the work of Watson et al. Both profiles show the existence of flame holes, pointing to local extinction. (K. A. Watson et al. 1999)

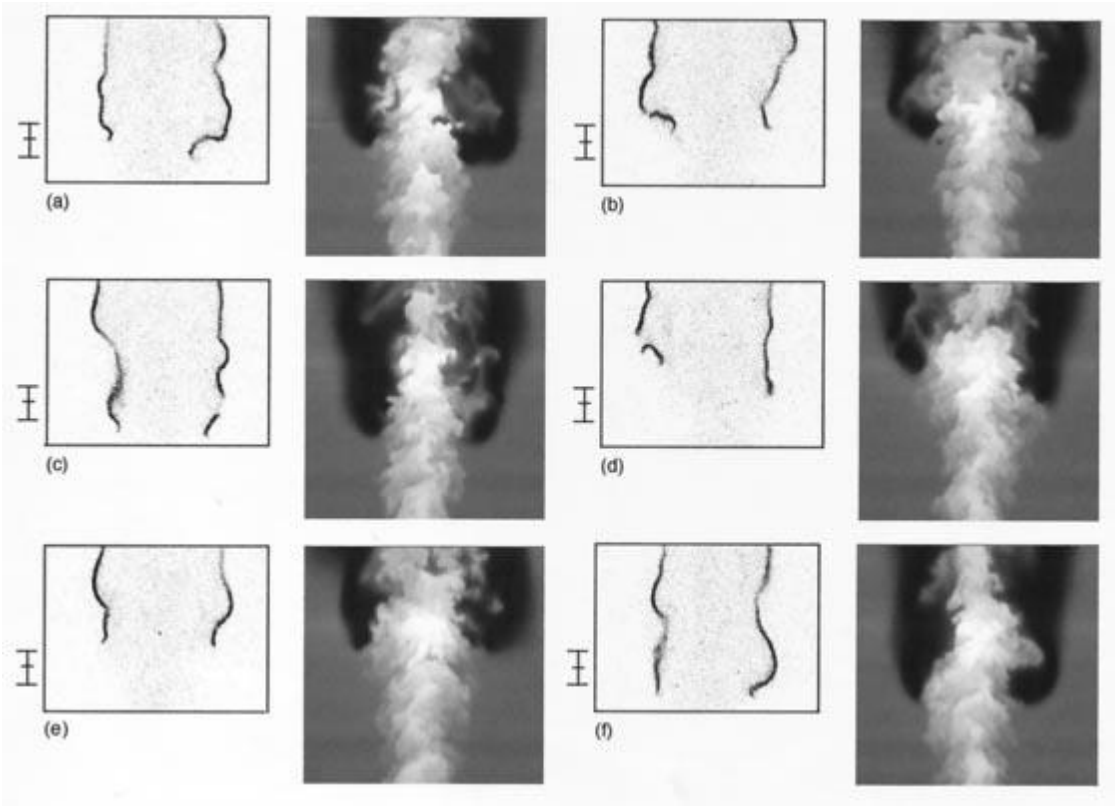

Figure 2.5 Vortex-Flame interaction in simultaneous CH PLIF and Rayleigh scattering images taken in a lifted jet flame (Watson et al. 2000)

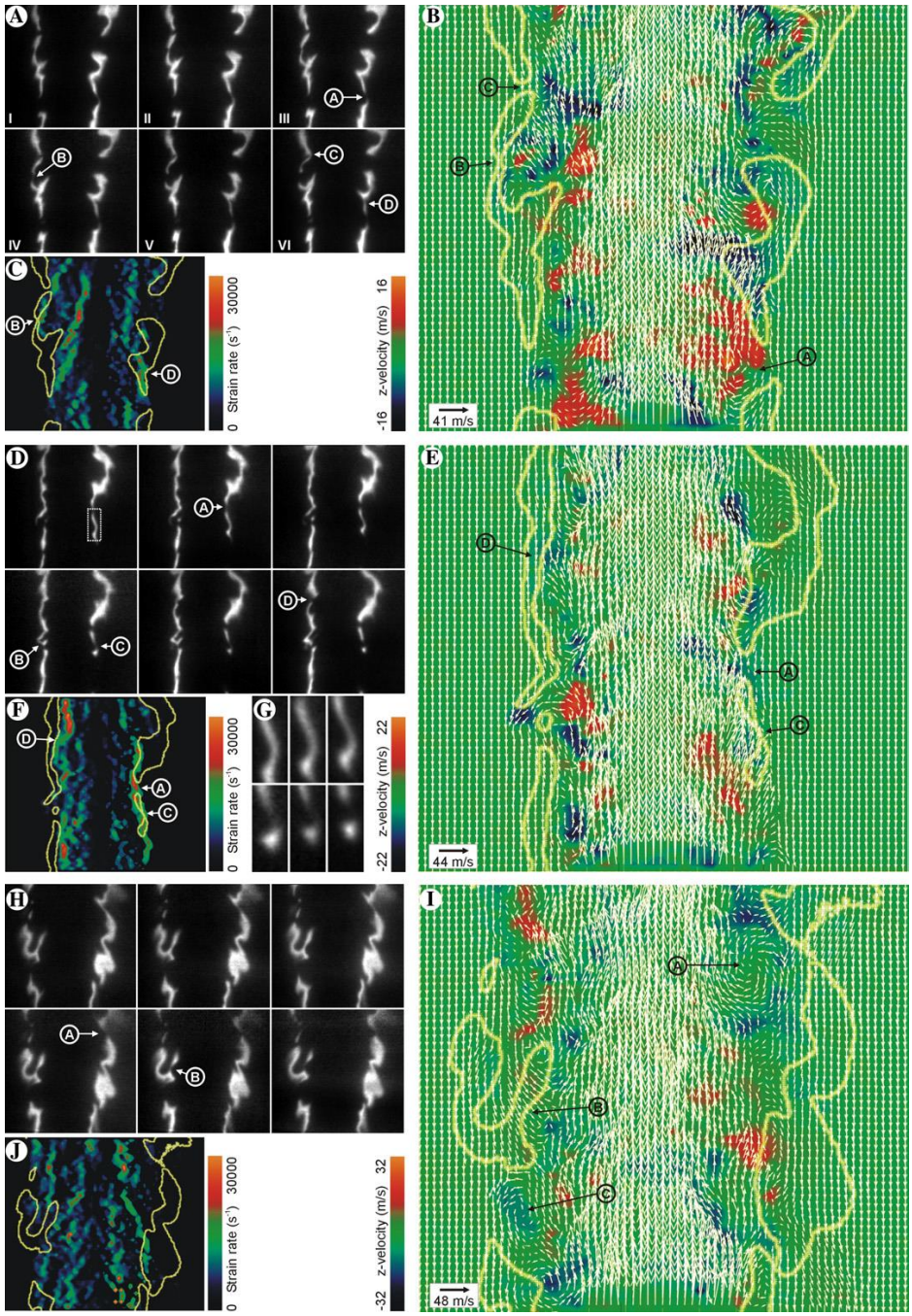

Figure 2.6 (A, D, and H) Three examples of OH time sequences. The time difference between individual images is 30 microseconds, and the image region corresponds to 32 · 30 mm^2 ((A and D) x/D = 4.5–8.25;(H) x/D = 8–11.75). (B, E, and I) PIV images recorded corresponding to the 3rd frame in the OH sequences. (C, F, and J) Maximum principal strain rates. (G)Magnified view of the region indicated by rectangle in (D). (Hult et al. 2005)

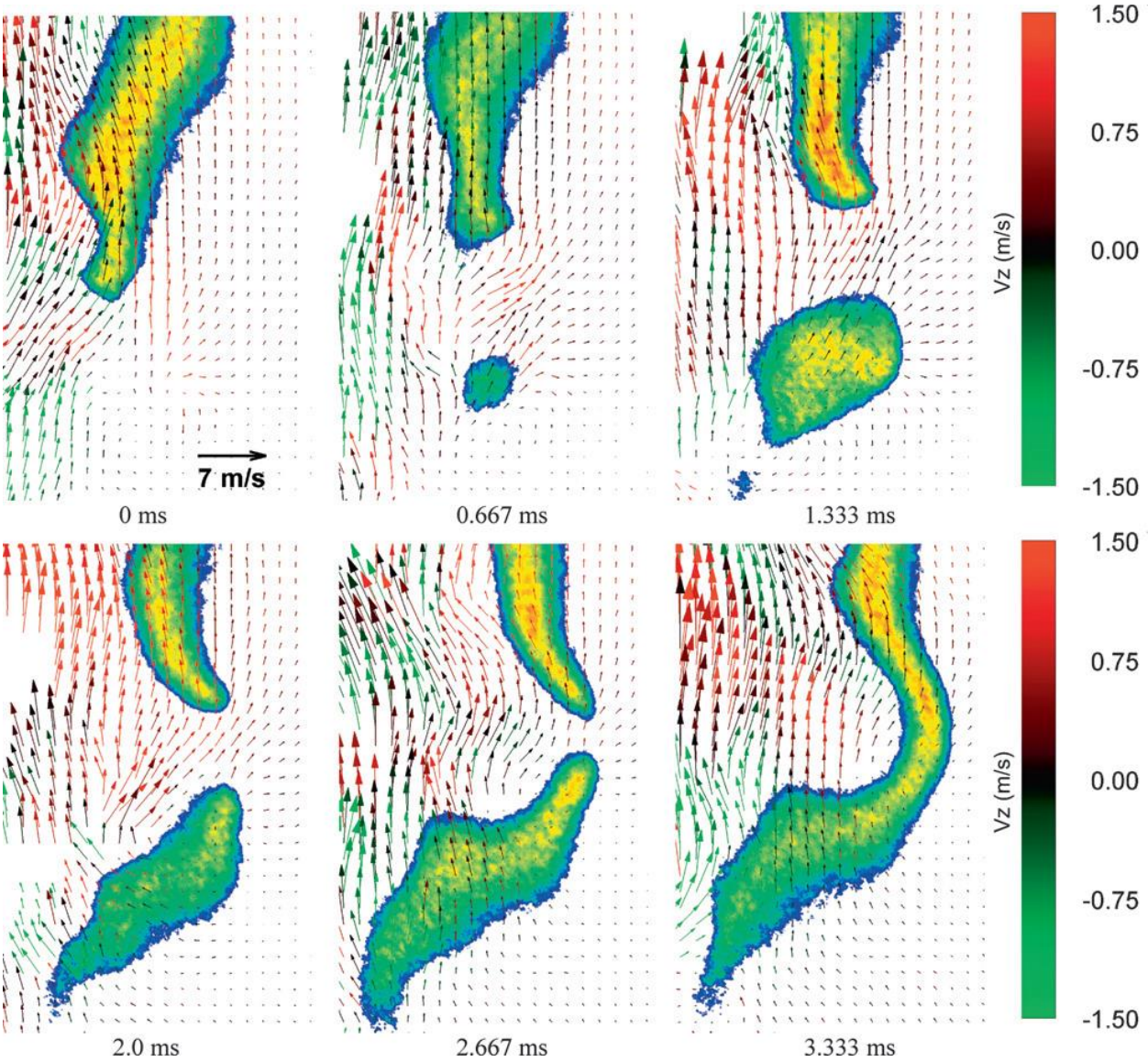

Figure 2.7 OH PLIF/PIV measurement sequences highlighting the formation, distortion, and merging of a flame island. (Boxx et al. 2009)

Global Simulation of Turbulent Flames

The complex chemistry and flow fields in fully turbulent flames with local extinction are computationally expensive to study. This was attempted in a non-premixed methane-air planar jet flame with simplified chemistry (Pantano 2004). This simulation used over 100 million grid points. The behavior of the flame holes in this flame was assumed to be controlled by the edge velocity. Joint probability density functions (PDFs) of edge velocity and scalar dissipation were presented, and it was determined that the edge velocity is largely controlled by scalar dissipation.

Kim and Kim attempted another technique using the results from previous edge flame experiments (Shay and Ronney 1998)and a constant density assumption to predict the edge speed in a turbulent

lifted non-premixed flame(Kim 2006). This simulation extracted the scalar dissipation rate directly from the DNS flow field and determined that edge velocity was the governing factor in flame hole behavior.

Direct numerical simulation has also been used to extract flame edge statistics in turbulent mixing layers (Zhang, Yang, and Wang 2012). This simulation provided spatial and temporal information about the structure and behavior of flame edges. However, it is difficult to compare the results of this transient simulation to experimental results. This arises due to the difficulty of matching the boundary conditions used in these simulations in a practical turbulent experiment.

One limitation of these kinds of studies is that the simulations can take months to complete, making parametric studies of edge flames impractical. In the simulations, the existence of flame holes is transient, like the experiments discussed earlier in this Chapter. Thus, the observation of flames holes is limited in the full simulation. A computational technique to isolate a flame hole and study it in detail would therefore be very beneficial.

Numerical Flame Hole Studies

Favier and Vervisch predicted a diffusion flame sheet undergoing extinction using 1-step chemistry (Favier 2001). This flame was formed by the pinching of two counter-rotating vortices (*Figure 2.8*). In this study, Damkohler number and scalar dissipation rate (Bilger 1990) were examined as the flame hole evolved. Damkohler number is the ratio of a relevant chemical timescale to the flow timescale. Scalar dissipation rate is computed from the gradient of a conserved scalar (mixture fraction) multiplied by a thermal diffusive term. The calculation of scalar dissipation rate is discussed in the next chapter. This study found that reaction rate increased with scalar dissipation rate, and the extinction event occurs at a defined one-dimensional 'flamelet quenching' scalar dissipation rate.

Flame holes have been formed in other simulations, usually those replicating the vortex-diffusion flame interactions found in experiments on the centerline of a counterflow burner. Simulations were performed on a methane-air diffusion jet flame impinged on by a vortex, and detailed species concentrations, temperature distributions, and velocity fields were reported (*Figure 2.9*). The counterflow geometry was exactly modeled, and detailed chemistry models along with a reduced chemistry model were compared (*Figure 2.10*) (Oh 2006).

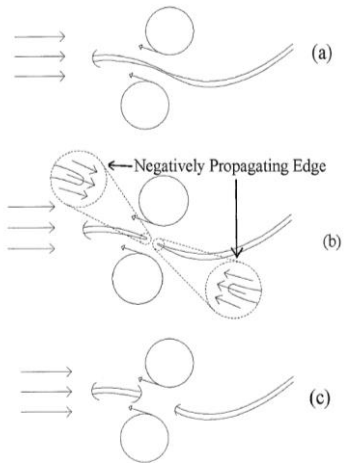

Figure 2.8 Evolution of a flame holes following the work of Favier and Vervisch (Favier 2001): (a) flame hole creation by impinging vortices, (b) flame hole growth via receding edge flames, and (c) flame hole recovery via forwardly propagating edge flames. (Carnell 2006)

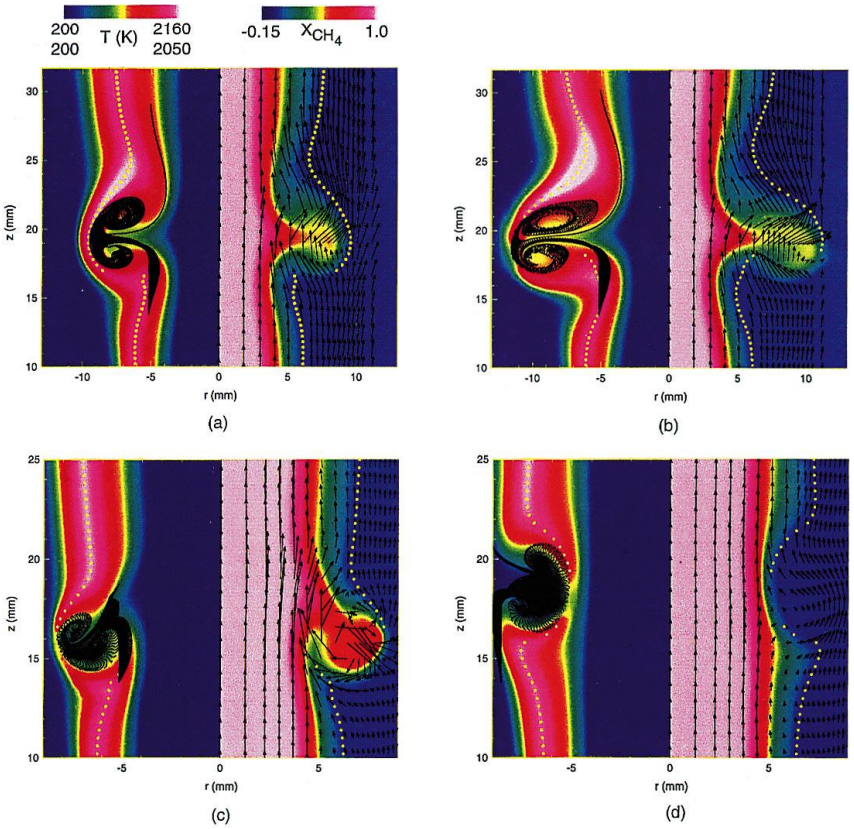

Figure 2.9 Color coded temperature fields (left) and methane mole fraction field with superimposed velocity vectors (right) showing the simulated temporal evolution of the vortex-flame interaction simulated by Takahashi (Takahashi 1996)

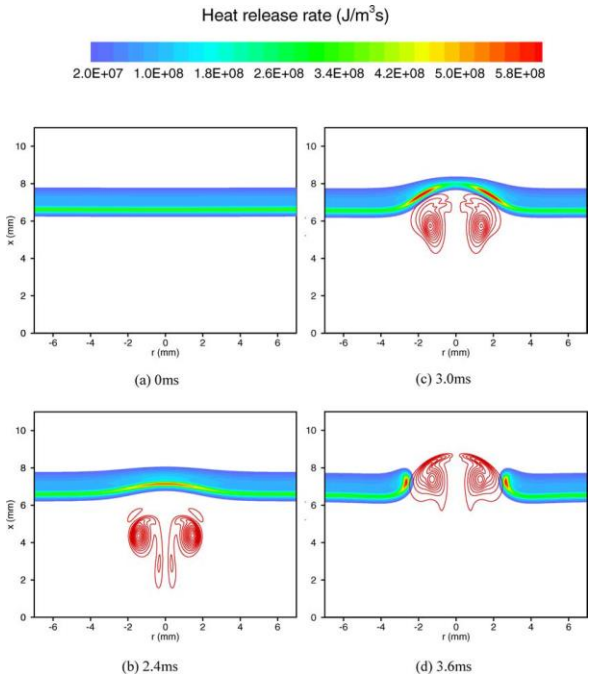

Figure 2.10 Instantaneous heat release rate and vorticity plots from the vortex-flame interaction simulated by Oh et al. (Oh 2006)

Counterflow Global Extinction Experiments

A convenient geometry for the study of strain based extinction is the counterflow burner. A comprehensive review has been provided by Tsuji detailing four different counterflow geometries used in laminar flow conditions (Tsuji 1982). Type I and II are counterflow jet flames, while type III and IV are porous media stabilized diffusion flames. Extinction in all of these burners is almost strictly a global phenomenon, and is transient, since local extinction first occurs at the stagnation point and the direction of velocity is away from this point. This prevents the detailed study of the flames leading up to and through extinction. Many groups have performed studies in which the gas velocities in these counterflow burners are increased slowly until the flame experiences global extinction. This was observed with varying concentrations of hydrogen (Pellett 1998) in a type II burner. Studies have been done using PIV on global extinction for methane, ethylene, propylene, and n-butane in a type 1 burner (Sarnacki 2012). This study concluded that the 1 dimensional extinction strain rate was consistent within experimental uncertainty for varying jet separations and diameters. Additionally, studies were done using n-propanol, iso-propanol, and propane to assess the effects of the hydroxyl radical in the fuel structure (Veloo 2011). The effects of high pressures on extinction in a counterflow diffusion flame were studied up to 2.0 Mpa (Neimann 2014). In addition, the effects of inhibitors (Takahashi 1983) (MacDonald 1999) (Chelliah 2003), diluence (Chen 2000), and water concentration (Lentati 1998) have all been studied on the global extinction limits. The effects of low gravity have been studied in conjunction with carbon dioxide diluence (Takahashi 2008). The effects of turbulence parameters on the global extinction of counterflow flames has been studied as well (Sardi 2000) (Kitajima 2000) (Korusoy 2002). The large repository of data from these studies provides a good understanding of one

dimensional extinction limits, but fails to provide detailed information as to the mechanism of flame extinction due to the transient nature of the extinction event. More importantly, these studies only provide a global indication of extinction and do not enable a study of the extinguishing edge flame structure that can occur in turbulent flames.

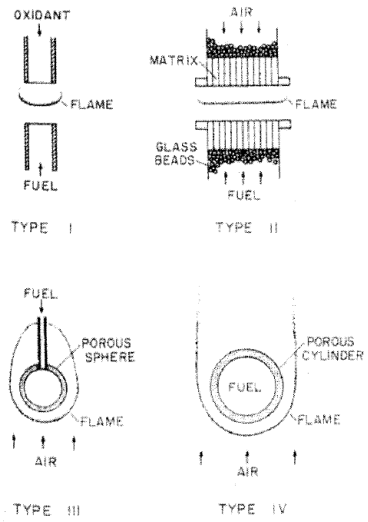

Figure 2.11 Overview of laminar counterflow burner geometries. (Tsuji 1982)

Numerical Counterflow Global Extinction Studies

Numerous extinction studies focus on the one-dimensional centerline extinction in a counterflow burner. These studies are performed in the same manner as the experimental counterflow centerline extinction studies. The numerical solution just before extinction occurs is treated as near-extinction conditions and characterizes an extinction strain rate. Balakrishnan *et al.* used this technique to investigate the effects of the chemistry model used for a hydrogen-air mixture (*Balakrishnan 1995*). This type of modeling is as pervasive as the experimental equivalent, and many of the same parameters were studied. Oscillating boundary conditions (Im 1996), pressure (Sohn 2000), radiative heat flux (Daguse 1996), inhibitors (Seshadri 1995), and flame structure (Du 1996) have all been examined. These simulations provide the same kind of stability data that the counterflow centerline extinction experiments provide. The chemical structure of the flame just prior to extinction can be analyzed and additional insight to the chemical pathways that take place leading up to extinction can be better understood.

A particularly useful one dimensional simulation of this phenomenon was developed using the detailed chemistry solver CHEMKIN (Lutz 1997). This program solves for temperature, species mass fractions, velocity field, and pressure gradient. This detailed simulation is of considerable utility in predicting global flame extinction in a counterflow geometry.

Flame Sheet Vortex Interaction Experiments

Due to the shortcomings of the global extinction limit studies mentioned in the previous section, the interaction between a laminar diffusion flame sheet and a vortex or vortex pair has been studied to attempt to provide more detailed information about extinction events. This type of experiment can provide a localized extinction event without having global flame extinction.

The interaction between a premixed flame sheet and a vortex was studied (*Figure 2.12*) by Nguyen and Paul (Nguyen and Paul 1996)This experiment used phase-locking to produce images of CH (*Figure 2.13*) and OH (*Figure 2.*14) radicals. This experiment allowed more detailed analysis of the flame hole formation and propagation, but flow field data was not gathered, limiting the utility of this data in developing or refining models. This work showed the CH was a good marker for primary reaction. This study also pointed out that the CH and OH structures found in the transient behavior leading to flame hole formation were different than the structures found in strained laminar flames or flamelets.

One of the most common ways to study the transient interaction between a strained laminar non-premixed flame sheet and a vortex is to stabilize a diffusion flame in a counterflow burner and use a pulse of fluid to send a vortex into the flame sheet along the burner centerline. This was pioneered by Rolon *et al.* using a piston and actuator (Rolon 1995). Laser Doppler anemometry (LDA) measurements were made to characterize the velocity profiles in this transient process (*Figure 2.15*). This geometry was used extensively, including studies using formaldehyde LIF (Santoro, Liñán, and Gomez 2000). This study measured flame front velocity and gas velocity. This allows the identification of forward and negative flame edges. Brockhinke *et al.* applied OH PLIF to obtain concentration measurements in unperturbed and vortex affected flames (*Figure 2.*16). Meyer *et al.* presented simultaneous PIV and OH PLIF results (*Figure 2.17*) in a hydrogen-air diffusion flame. This provided strain rates at the flame edge. Amantini performed simultaneous OH and CO LIF experiments with vortices impinging on a flame sheet from both sides of the flame sheet (*Figure 2.18*). This experiment provided time evolution of a flame hole, including formation and healing (*Figure 2.19*) (Amantini et al. 2005).

While these measurements provided valuable insight into the extinction process, they still represent a transient process. The phase locking technique was effective in showing the temporal evolution of breaks in the flame sheet. This technique is not applicable to turbulent flows, and therefore is limited to laminar studies. Amantini attempted to resolve the negatively propagating edge flame and found that even in these phase-locked transient experiments, the negative flame edge existed for too short a period for detailed measurement and was not adequately resolved.

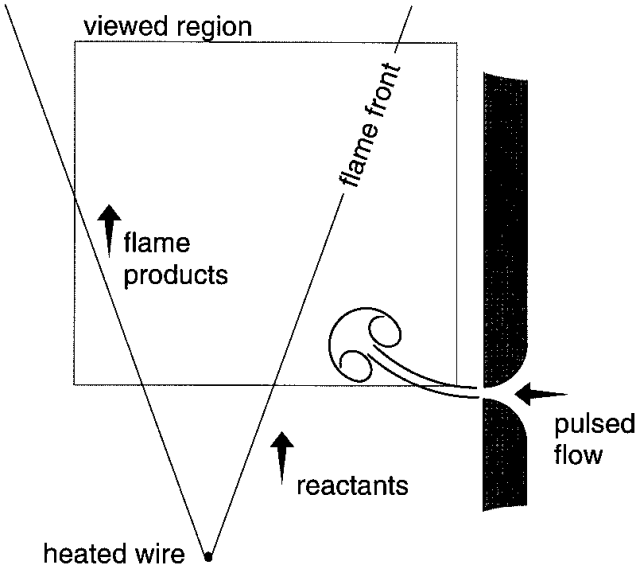

Figure 2.12 Cartoon of flame sheet-vortex interaction in premixed flames (Nguyen and Paul 1996)

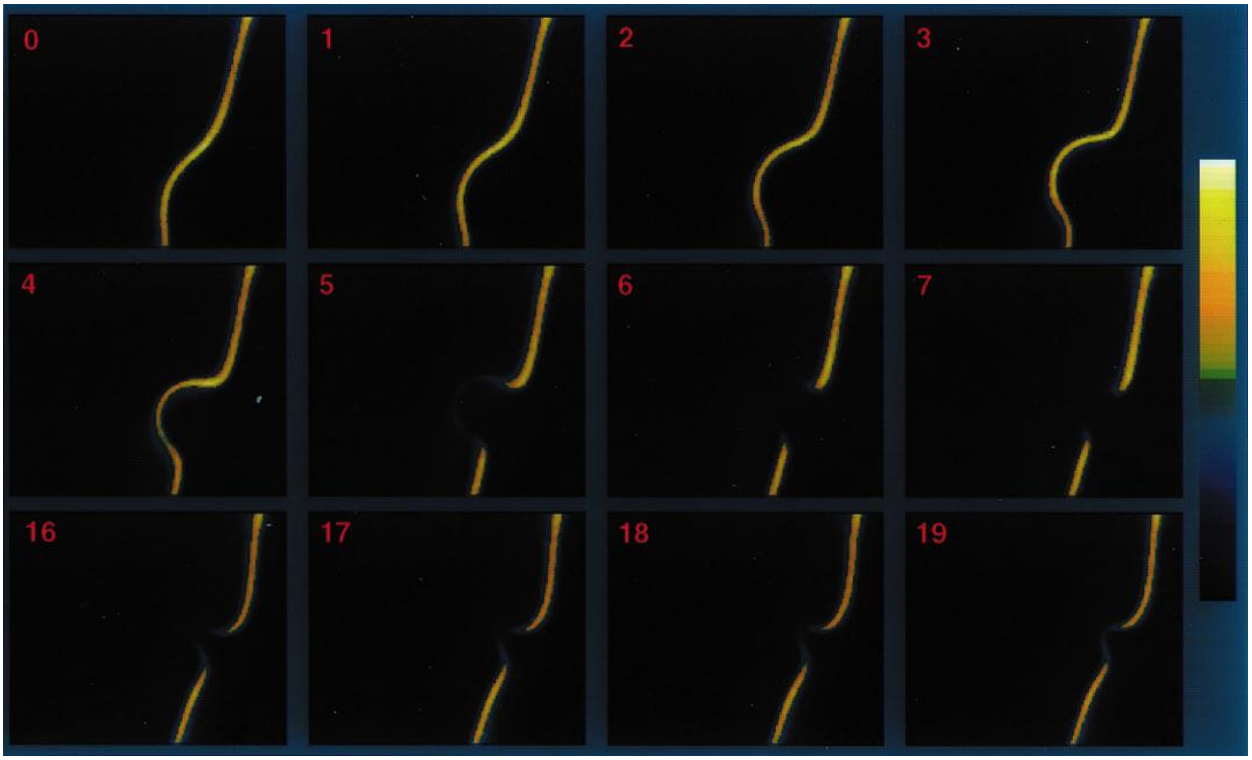

Figure 2.13 Phase sampled CH PLIF showing the evolution of a flame hole (Nguyen and Paul 1996)

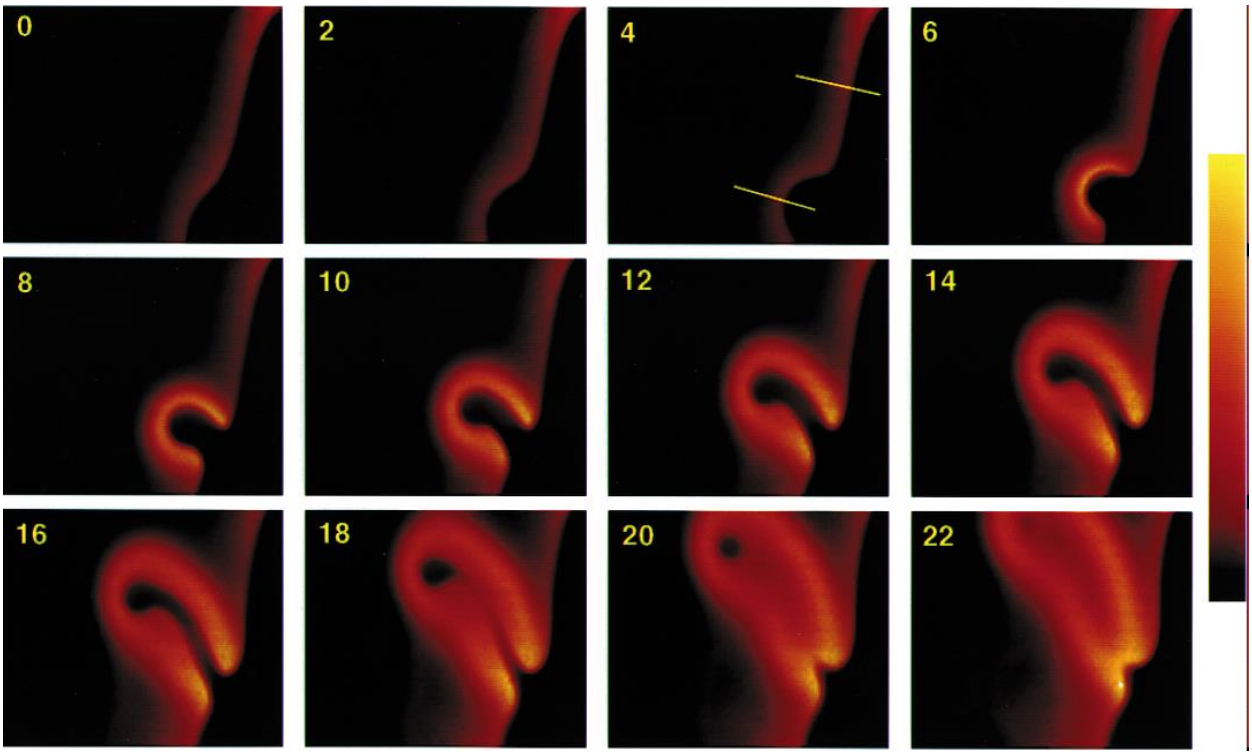

Figure 2.14 Phase sampled OH PLIF showing the evolution of a flame hole (Nguyen and Paul 1996)

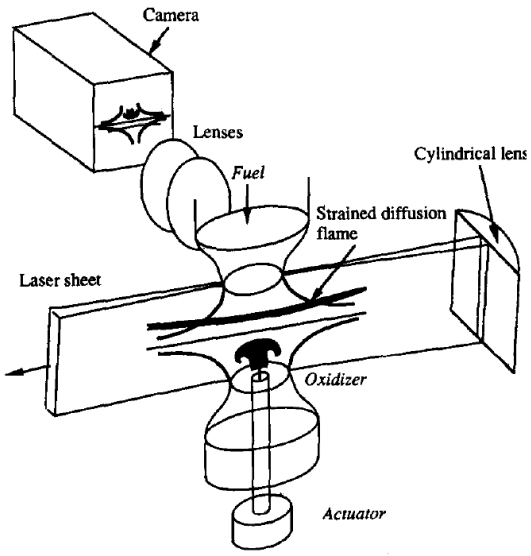

Figure 2.15 Experimental setup of Rolon et al. showing LDA setup and burner geometry (Rolon 1995)

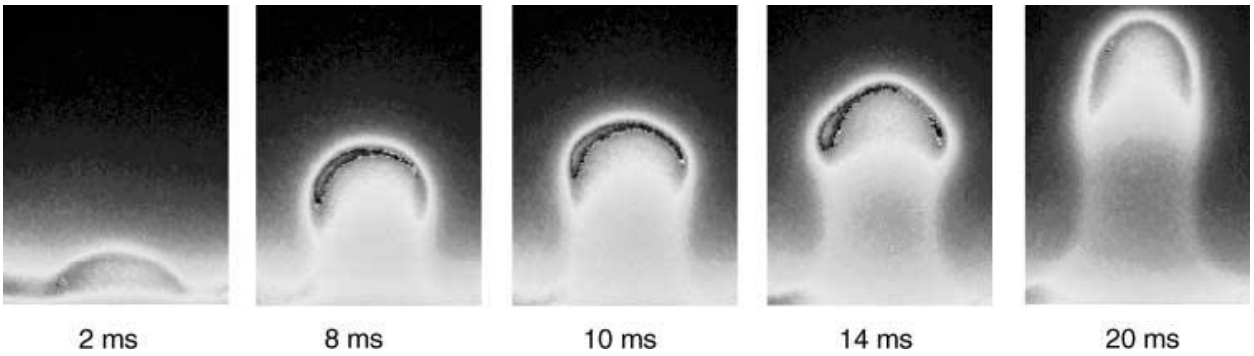

Figure 2.16 Temporal evolution of OH PLIF emission from flame sheet-vortex interaction. (Brockhinke et al. 2001)

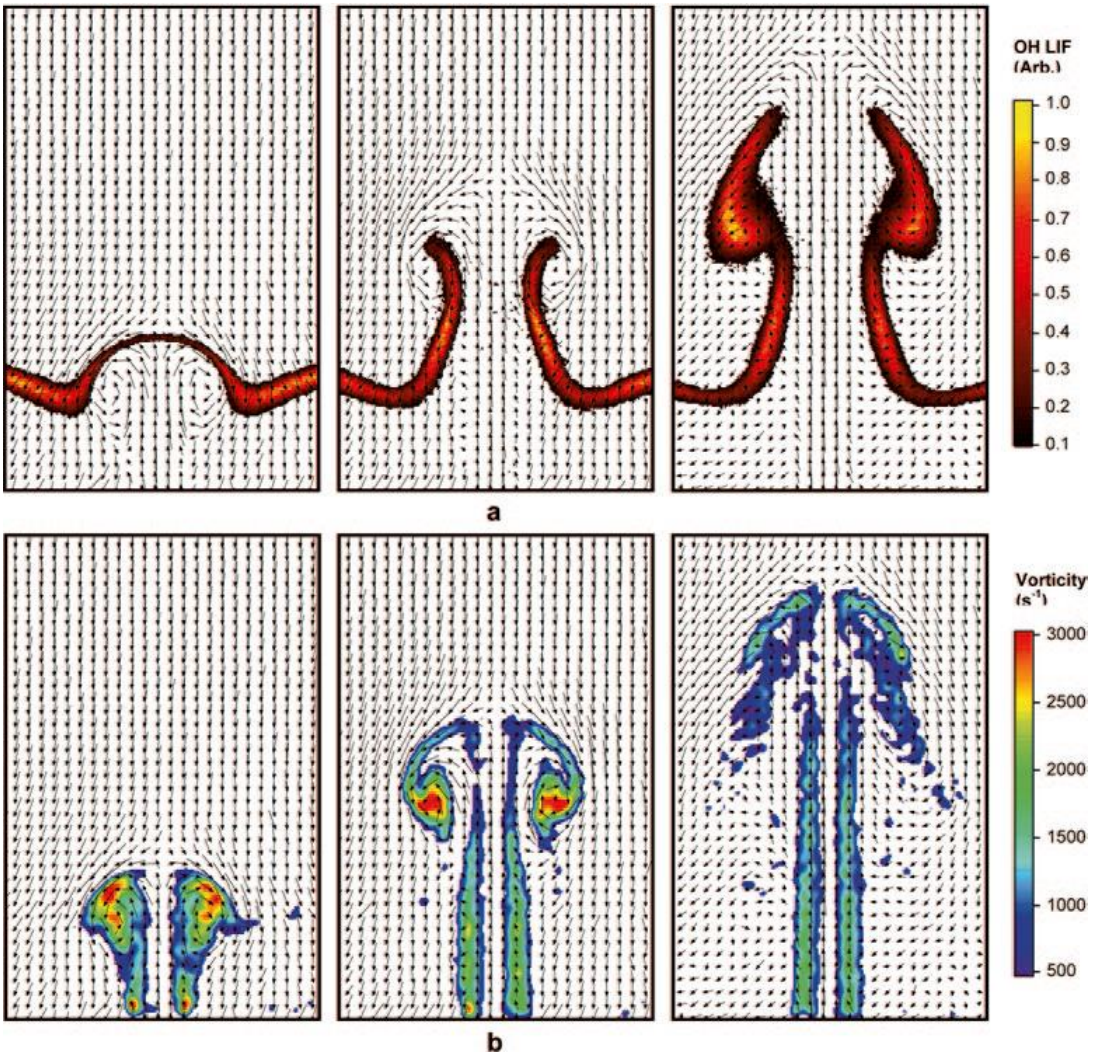

Figure 2.17 Simultaneous OH PLIF and PIV results from (Meyer et al. 2004)*showing the evolution of a vortex-flame sheet interaction*

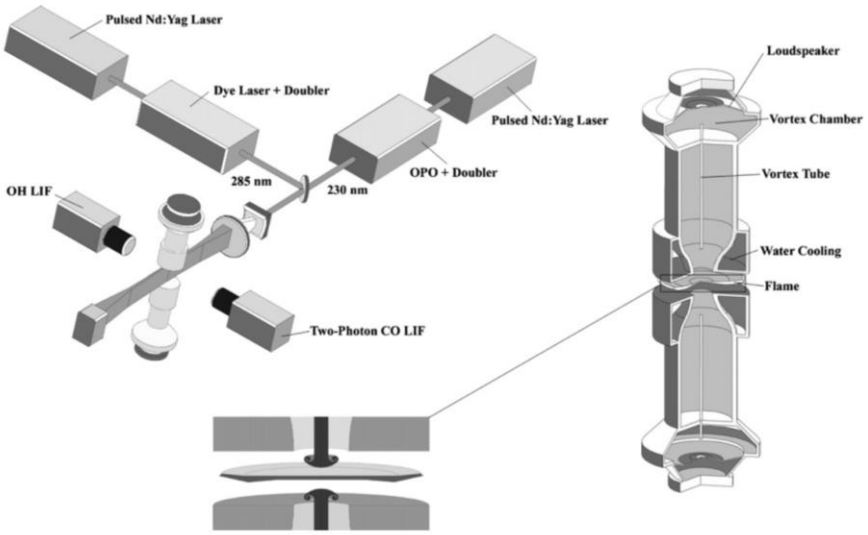

Figure 2.18 Experimental setup of Amantini et al. showing burner geometry and CH/OH PLIF setup. (Amantini et al. 2005)

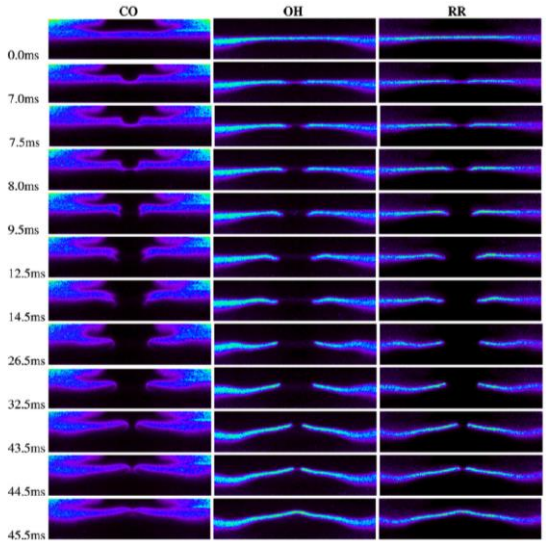

Figure 2.19 Time evolution of a flame hole including formation and healing. CO LIF (left), OH LIF (center), and reaction rate imaging (right) are shown. (Amantini et al. 2005)

Forward Edge Experimental Studies

Forward edge flames have been investigated for over half a century, with some of the first research being performed using a Schlieren optical technique to visualize the propagation of a forward edge flame through the mixing layer between methane and air (Phillips 1965). This type of flame is easily stabilized in the laboratory where the edge is stationary due to a balance between the propagation speed and the incoming velocity. A diverging section with a stoichiometry gradient was used to stabilize a forwardly propagating triple flame front by (Kĩoni et al. 1999)(*Figure 2.21a*). The planar triple flame structure (*Figure 2.20)* was described in detail, and PIV measurements were taken in this geometry (Kĩoni et al. 1999). OH PLIF measurements were performed, and it was determined that the maximum velocity in this flame occurs at the diffusion flame edge. It was also observed that the heat release in the triple flame caused a decrease in incoming gas velocity, thus aiding in the propagation of the flame.

Standing triple flame edges were created in a counterflow burner (Santoro, Liñán, and Gomez 2000)and formaldehyde PLIF was used to determine that a forwardly propagating flame edge that is not highly strained exhibits a triple flame structure, and as the strain was increased (which led to a decrease in Damkohler number), the flame did not exhibit the tribrachial structure. The propagation speeds of the forwardly propagating flames were measured using LDV and correlated to Damkohler number.

A coflow jet geometry has also been studied (Lee et al. 2003)including simultaneous Rayleigh thermometry, CH, and OH PLIF (*Figure 2.22*). This study confirmed that the largest chemical reaction

occurred in the diffusion flame branch along the stoichiometric contour. The blowoff of these flames was studied and a correlation was presented for flame liftoff with respect to jet and coflow velocity.

Concentrations of NO_x and soot were examined in a coannular jet flame (Yamamoto, Isii, and Ohnishi 2011) This flame consisted of a central air jet, a fuel annulus outside that, and another coflow air annulus on the outside of the tube. This study concluded that the partial premixing that takes place upstream of a triple flame reduces emissions of NO_x and soot production.

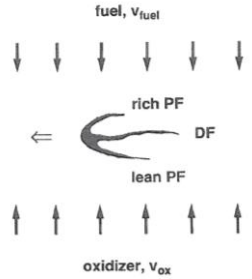

Figure 2.20 Schematic of a triple flame propagating in a mixing layer (Kioni et al. 1993)

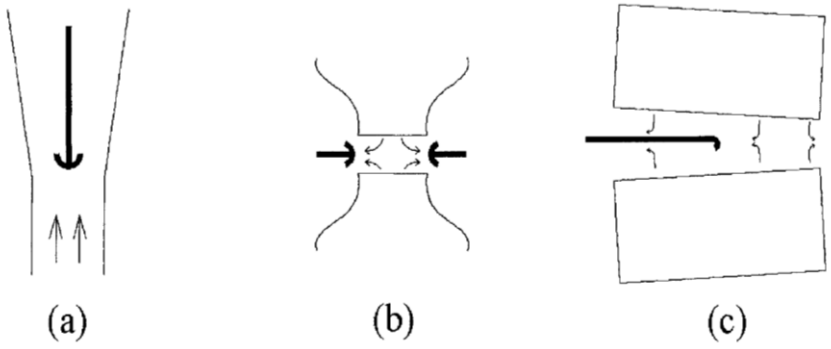

Figure 2.21 Edge flame burner geometries for previous research (a) Forwardly propagating flame (Kioni et al. 1993)*, (b) Forwardly propagating flame edge* (Santoro, Liñán, and Gomez 2000)*;(c) Stationary flame edge* (Shay and Ronney 1998)

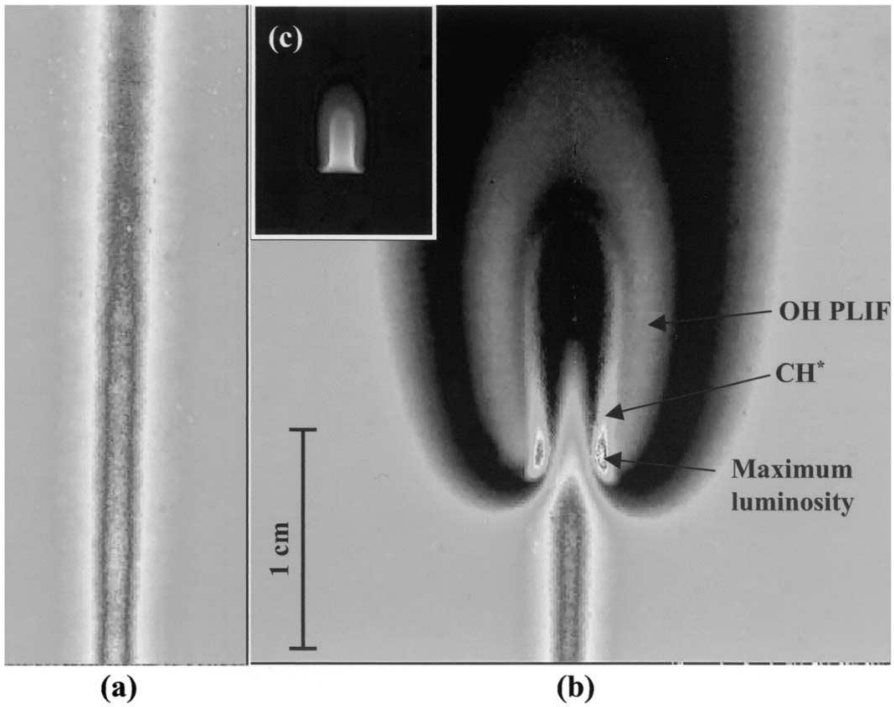

Figure 2.22 Simultaneous Rayleigh intensity, OH PLIF, and chemiluminescence for a lifted jet flame (b). This is compared to the cold flow case (a) and a photograph of the flame (c) (Lee et al. 2003)

Numerical Forward Edge Studies

The forward edge flame has been observed to be the mechanism by which flame holes heal. These types of flame edges have been well studied, with the edge propagation velocity being numerically predicted to scale with scalar dissipation (Ruetsch, Vervisch, and Liñán 1995). A lifted laminar diffusion flame on a round jet was simulated, and the structure and liftoff height of the flame was analyzed in detail (Boulanger et al. 2003). This was also studied in a planar configuration (Im and Chen 1999). The effects of heat loss on the propagation in addition to the flame thickness in these flames were studied as well (Daou, Daou, and Dold 2002). The interaction of these flame fronts was studied using a slot burner with stratified fueling and compared to numerical results (Kostka and Renfro 2007)The effects of gravity were studied by Pearce and Daou (Pearce and Daou 2013), and it was found that gravity can slightly alter the flame speed if it acts in a direction perpendicular to flame propagation. All of these studies

agreed well with experimental data, and the simulation of forwardly propagating edges seems well understood and acceptably accurate.

Stationary Edge Experiments

An intentionally misaligned slot burner (*Figure 2.21c)* was used to create a stationary edge flame (Shay and Ronney 1998). The researchers found that the extinction strain rate at the edge location was different than the global extinction strain rate in a standard counterflow burner. The flow field of this burner was not studied, so there is some uncertainty as to the actual gas velocity at the edge. Due to the geometry of the burner, it is hypothesized that the bulk of the flow is parallel to the flame front similar to case (b) in Fig. 1.2. This study found that the gradient of strain rate did not have an effect on the strain required to create the flame edge.

Negative Edge Experiments

Negative edge flames were observed in a transient counterflow slot jet burner (Cha and Ronney 2006). This experiment used the chemiluminescence of the flame as a marker for the flame edge. The experiment allowed for the imaging of the negative edge flame (*Figure 2.23)*, but lacked detailed measurements of species, temperature, or gas velocity at the edge.

A stationary extinction edge was formed in a counterflow burner with inert jet impingement for methane and propane flames (*Figure 2.24*) (Chen and Bilger 2000). The inert jets did cause a negative flame edge to be observed, however the post-extinction behavior of the flame sheet is not representative of the behavior in a turbulent flame, as the flow through the edge is into nitrogen, not the fuel air mixture; thus, dilution plays an artificial role in the extinction process compared to local extinction in a turbulent diffusion flame sheet. As a result, the extinction strain rates observed in these holes was significantly lower than global extinction rates for centerline extinction in a counterflow

burner. In this work, it was shown that the number of flame holes in a flame sheet does not significantly alter the behavior of any of the individual holes.

Carnell and Renfro stabilized a stationary negative flame edge in a counterflow burner by replacing the standard nitrogen guard flow with a flow that matched the composition of the main flow (Carnell and Renfro 2005). This created an off-axis extinction point. Chemiluminescence imaging and OH PLIF were used to show the existence of this edge (*Figure 2.25*). This group also used Raman spectroscopy to obtain temperature profiles through the edge to quantify the heat flux through the edge (Carnell and Renfro 2007). This study also showed that the maximum temperature gradient occurs downstream of the extinction edge, but relatively close to the end of the reaction zone. OH and formaldehyde PLIF were performed and contours of forward reaction rate for the OH –formaldehyde reaction were developed from the experimental data. This group concluded that the formaldehyde width beyond the region of flame extinction is not proportional to scalar dissipation. However, it was found that the width increases drastically after extinction, and this was a useful marker for a local extinction event.

A stationary negative flame edge was also stabilized by Yang *et. al* for some experimental conditions in a twin jet counterflow slot burner (*Figure 2.26*). A stability map for their experimental geometry and observations on the luminosity of the flame relative to the edge location were provided.

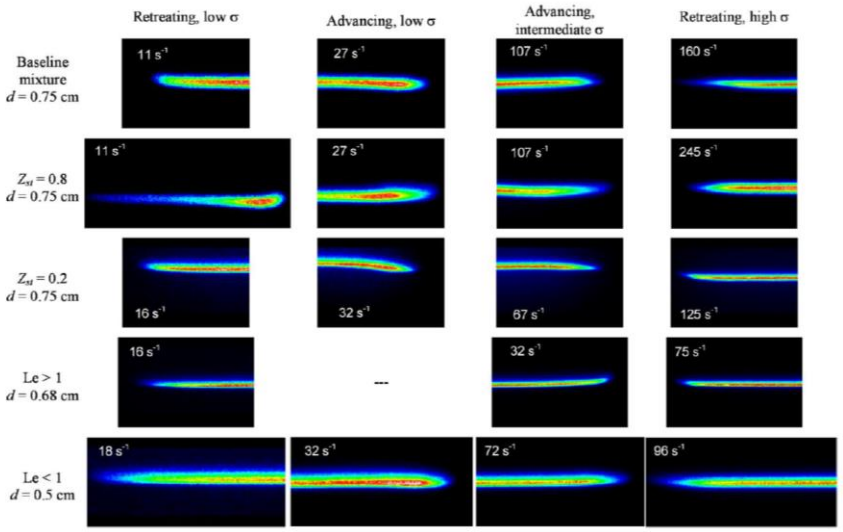

Figure 2.23 False color chemiluminescence images from the work of Cha and Ronney. The left and right columns show retreating edge flames for varying strain rate, Lewis number, and gas mixtures (Cha and Ronney 2006)

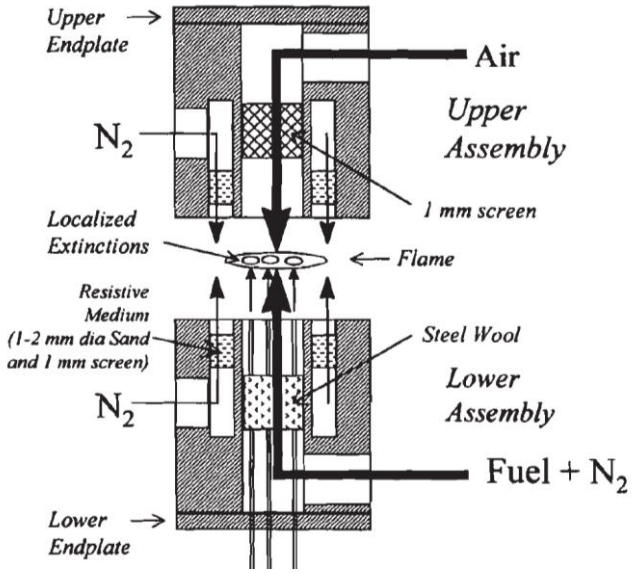

Figure 2.24 Experimental setup of (Chen and Bilger 2000)*showing the localized extinctions in the flame sheet.*

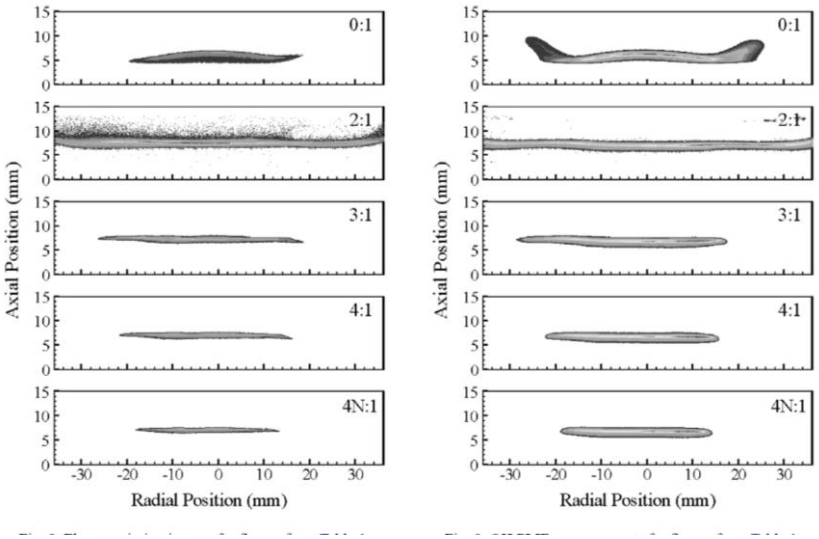

Figure 2.25 Chemiluminescence (left) and OH PLIF (right) measurements in the work of Carnell and Renfro comparing different inner and outer nozzle velocity ratios. The case 4N:1 is extinction with an inert nitrogen outer flow. The difference between this and the 4:1 case above it is clear. (Carnell and Renfro 2005)

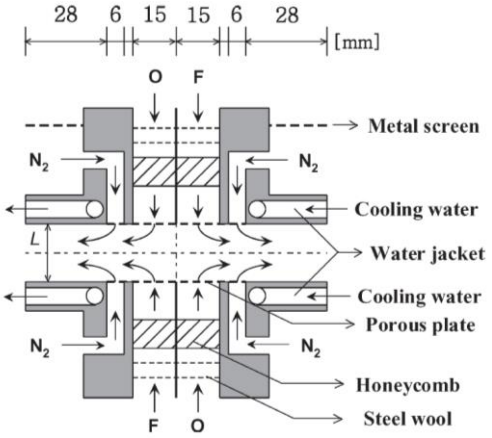

Figure 2.26 Schematic of twin-jet counterflow burner used to stabilize interacting flame edges (Yang et al. 2009)

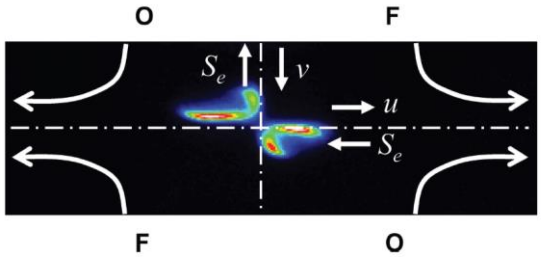

Figure 2.27 Example of interacting flame fronts with negative flame edges (Yang et al. 2009)

Numerical Negative Edge Studies

Negative edge flames have been studied in the transient simulations involving flame holes and turbulent flows. In addition, the simulations of Carnell and Renfro utilizing an off-axis extinction point in a counterflow burner (*Figure 2.2*) have provided significant insight to the mechanics of flame extinction in a steady state simulation. The formation of the negative flame edge off axis in this burner separates the location of local extinction from the location of global stabilization (the burner centerline). Thus separation allowed for the creation of a stationary, yet extinguishing flame edge. This facilitates very detailed study of the mechanism of flame extinction. A similar approach is used in the present work for experimental studies of turbulent flame extinction. Numerical studies were performed in the laminar flames to characterize the temperature profile and flow field of the burner (*Figure 2.28*). (Carnell and Renfro 2005). A numerical study varying the inner nozzle geometry led to the development of a relationship between advective heat flux through the extinction edge and the scalar dissipation rate at which the flame edge forms (Carnell and Renfro 2006). The temperature profile in the burner was compared to both OPPDIF simulations and Raman spectroscopy measurements. This showed the shortcomings of the one step chemistry model used in this study (*Figure 2.*29) (Carnell and Renfro 2007). CH and OH PLIF results were simulated and compared to measurements made in the burner (Carnell et al. 2009).

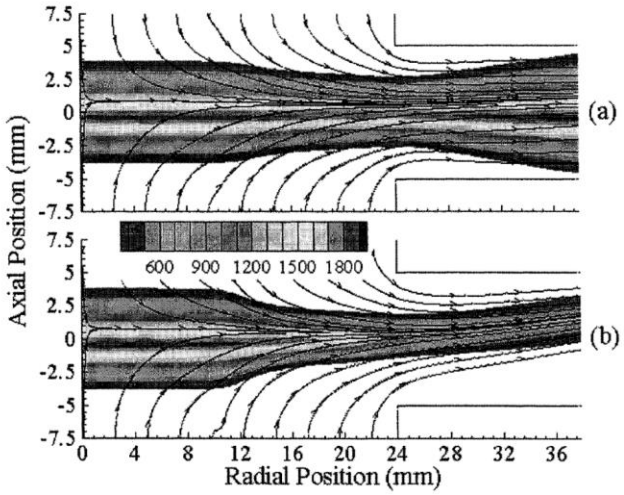

Figure 2.28 Superimposed temperature and velocity field in the burner of Carnell and Renfro. This figure shows the flow field for a (a) standard diffusion flame and (b) the off axis extinction case.

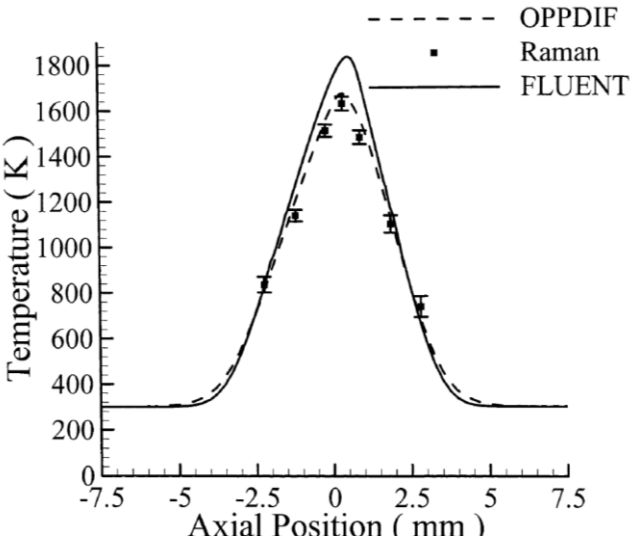

Figure 2.29 Comparison of OPPDIF and Fluent simulated temperature profiles in the work of Carnell and Renfro (Carnell and Renfro 2007)

Summary

The study of positive (ignition) flame edges has been studies extensively in prior work. The study of negative (extinction) edges has been studied in laminar unsteady flows, such as the centerline flame sheet-vortex interaction experiments and simulations that make up the bulk of the literature. Recently, stable, stationary negative flame edges have been studied both experimentally and computationally to more closely analyze the extinction process. The research contained in this thesis addresses a previously unstudied type of extinction edge. This study involves a negative flame edge in a statistically stationary

turbulent flow. This flame edge will not be completely stationary due to the nature of turbulent flow; however it will be located in a well-defined region of the burner to allow for detailed study of the extinguishing edge. The previous study outlined in this literature review does not provide information on the flame edge behavior as a function of scalar dissipation rate. This thesis provides a preliminary analysis of the negative flame edge velocity in turbulent non-premixed flames.

Chapter 3: Burner Design and Development

Based on the results of the literature review presented in Chapter 2, a new two dimensional burner geometry was designed for studies of statistically stationary negative edge flames in turbulent flows. In order to separate the mechanism of flame stabilization from the mechanism of local extinction so that local extinction did not lead to global extinction, it was determined that a diffusion flame would be stabilized in the wake of a splitter plate and extinguished downstream. In the development of this new burner geometry, three different burner designs were tested. One was a straight channel with a linear convergent section (*Figure 3.1a*), another was a linear convergent nozzle (*Figure 3.1b*), and the final design was a straight burner with impinging side jets (*Figure 3.1c*). Scalar dissipation rate (*Equation* 1) using the Bilger mixture fraction (*Equation 2*) (Bilger 1990) has been shown to be a useful parameter for predicting extinction in laminar counterflow flames (Carnell 2006). This parameter was used to evaluate the effectiveness of each burner design at creating an extinction edge. Simulations of mixing in preliminary burner designs were used to simulate scalar dissipation rate. The majority of the simulations were performed without chemical reactions, which are more computationally expensive to compute.

$$\chi = \frac{\lambda}{\rho c_p}\left(\left(\frac{dZ_{BLGR}}{dx}\right)^2 + \left(\frac{dZ_{BLGR}}{dy}\right)^2\right)$$

Equation 1 Calculation of scalar dissipation(Carnell 2006)

$$Z_{BLGR} = \frac{2Y_C / W_C + \tfrac{1}{2}Y_H / W_H + \left(Y_O - Y_O^O\right)/W_O}{2Y_C^F / W_C + \tfrac{1}{2}Y_H^F / W_H + Y_O^O / W_O}$$

Equation 2 Calculation of Bilger mixture fraction (Bilger, Stårner, and Kee 1990)

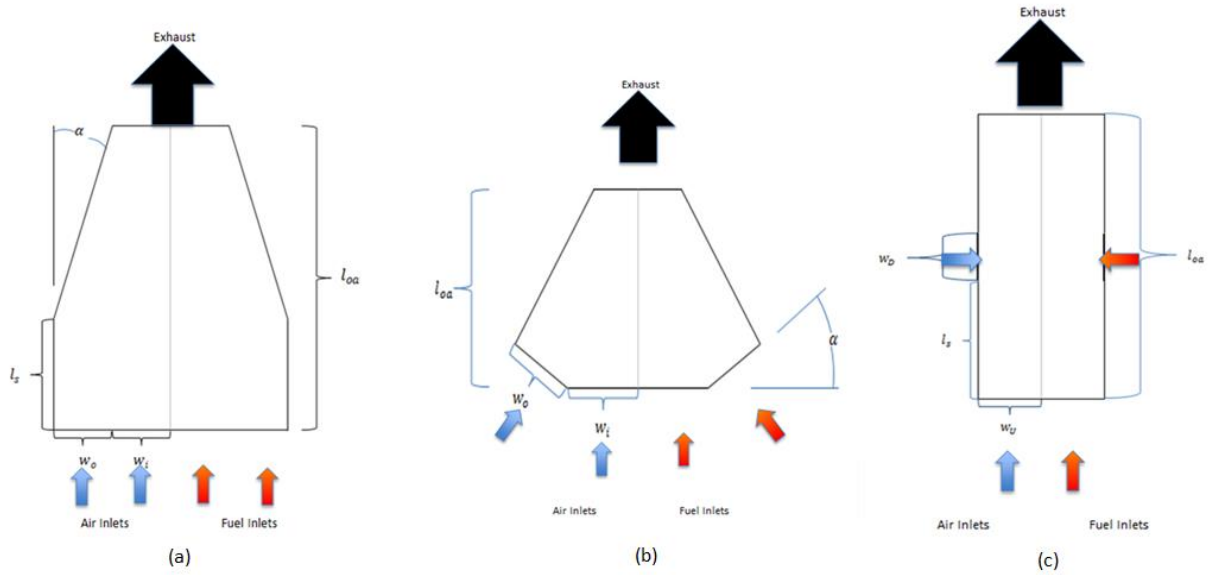

Figure 3.1 Burner geometries simulated

Simulation Methods

In the development of the new burner geometry presented in this chapter, the commercial CFD code FLUENT version 13.0 was used to simulate the fluid flow in the proposed geometries. The majority of the simulations presented were done without modeling combustion in the simulation. This allowed for rapid simulation of many different geometries and flow rates. Scalar dissipation rate, which was calculated along the stoichiometric contour using a first order centered differencing scheme in MATLAB, was used as the variable of interest in predicting the capability of the burner design for flame edge formation.

A structured mesh was used for all cases, with the worst grid resolution being 250 microns for the non-reacting cases. The reacting case mesh had a resolution of 62.5 microns. This grid was sufficiently dense to capture the high gradients in the flame edge, and a mesh independence study was carried out, and it was found that the scalar dissipation rate along the stoichiometric contour changed by less than 0.5% with a double grid (*Figure 3.2*)

For the non-reacting case, a viscous –laminar model was used to simulate the flow field. The flow was assumed to be incompressible. Specific heat and viscosity were modeled using the ideal gas mixing law. Mass diffusivity and thermal conductivity were calculated using kinetic theory. The pressure-velocity coupling scheme used was the Semi-Implicit Method for Pressure Linked Equations (SIMPLE). All gradients were calculated using Green-Gauss cell based differencing. Pressure was calculated using the Pressure Staggering Option (PRESTO!). Momentum, species, and energy equations were all solved using second order upwind differencing.

For the reacting cases presented, the chemical reactions were simulated using one-step methane-air chemistry. The stiff chemistry solver was used to solve for the reaction rate in the flow. This method was shown to be effective in predicting the existence of a flame edge in the work of Carnell and Renfro (2006). This numerical solution was not expected to predict the detailed chemistry and structure of the flame, but was instead used to predict the existence of an edge and to guide the detailed burner design.

In preliminary design calculations the fuel inlets were modeled as 20% methane and 80% nitrogen by volume. The air inlets were modeled as 20.95% oxygen and 79.05% nitrogen. The inlets were assumed to have uniform velocity profiles with all flow normal to the inlet surface. These boundary conditions were selected to match the fuel concentrations in past studies (Carnell 2006). This was done to allow the extinction scalar dissipation rate for the flame to be predicted from their work. In the preliminary design phase, the minimum scalar dissipation rate to create an extinction event was assumed to be 17 s^{-1} as this value was consistent with the local scalar dissipation rate in the off-axis extinction from Carnell.

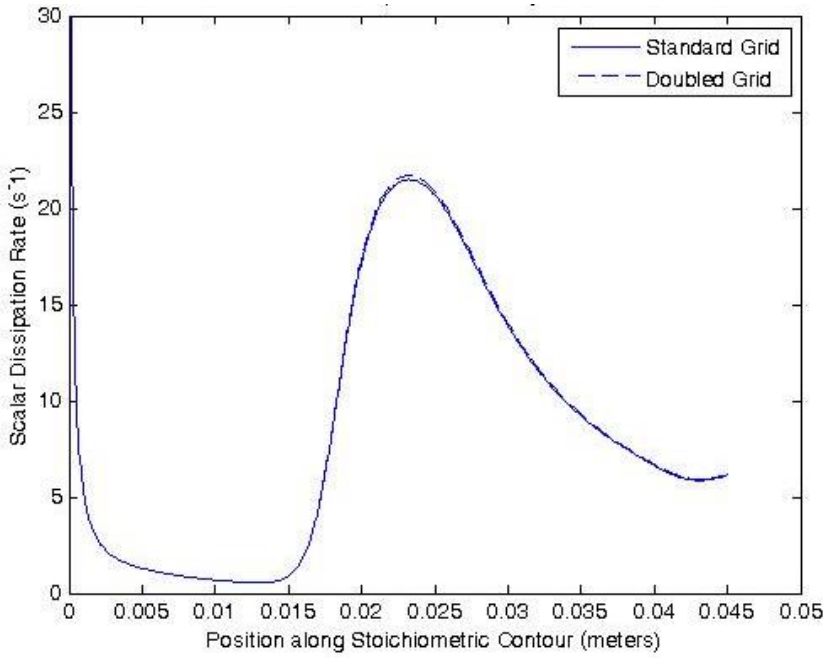

Figure 3.2 Grid independence for reacting simulation case with 62.5 micron grid resolution

Channel with Convergent Nozzle Design Evaluation

Using ANSYS fluent, a convergent two dimensional nozzle geometry with the reaction occurring inside the nozzle was modeled (*Figure 3.1a*). This burner includes provisions for 4 inlets, two for fuel and two for air. There are a set of inner nozzles, and a set of outer nozzles. These nozzles are rectangular. In order to maintain flow without recirculation, the velocities must be the same in both of the inner slots and both of the outer slots. Different velocities and species concentrations can be used in each of these slots. The size of the burner slots(w_o *and* w_i), half angle of the burner(α), length of the burner(l_{oa}), length of the straight section before the convergence starts(l_s), and flow rates were all varied in order to analyze the attainable scalar dissipation rates. In order to minimize computational expense, simulations were run in the non-reacting case.

Scalar dissipation along the stoichiometric contour was calculated (*Figure 3.3*) At the burner entry, which is the end of a splitter plate, the scalar dissipation is near infinite, because the mixture fraction is a step function with a value of 1 on the fuel (right) side and 0 on the air (left) side. As the area of the nozzle decreases as the distance from the origin increases, the scalar dissipation begins to rise. This

nozzle begins to converge at a distance of 2 cm from the inlet. The scalar dissipation rate reaches a maximum at the exit of the burner, as this is the minimum area of the burner. This is the peak downstream scalar dissipation rate for this geometry. This value is used to compare the performance of the different burner geometries and flow rates, as opposed to the value at the burner inlet.

The peak scalar dissipation rate for the different geometries and flow rates were tabulated (*Tables 3.1-4*). Increasing mass flow rate leads to an increase in peak scalar dissipation rate, as expected; however the obtained values were far from the design goal of 17 s^{-1}. After a detailed analysis of this geometry, it was observed that in some cases the scalar dissipation rate along the centerline of the burner did not exhibit a monotonic increase after the start of the convergent section (*Figure 3.5*). This burner geometry was not selected for the final design in light of these observations in the preliminary simulations.

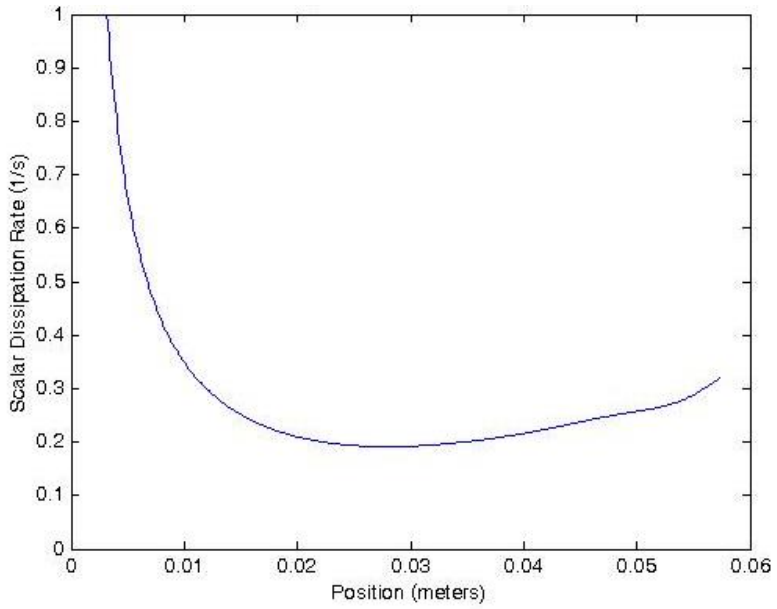

Figure 3.3 Scalar dissipation rate along the stoichiometric contour for the 10 cm/sec flow case in the 15 degree burner.

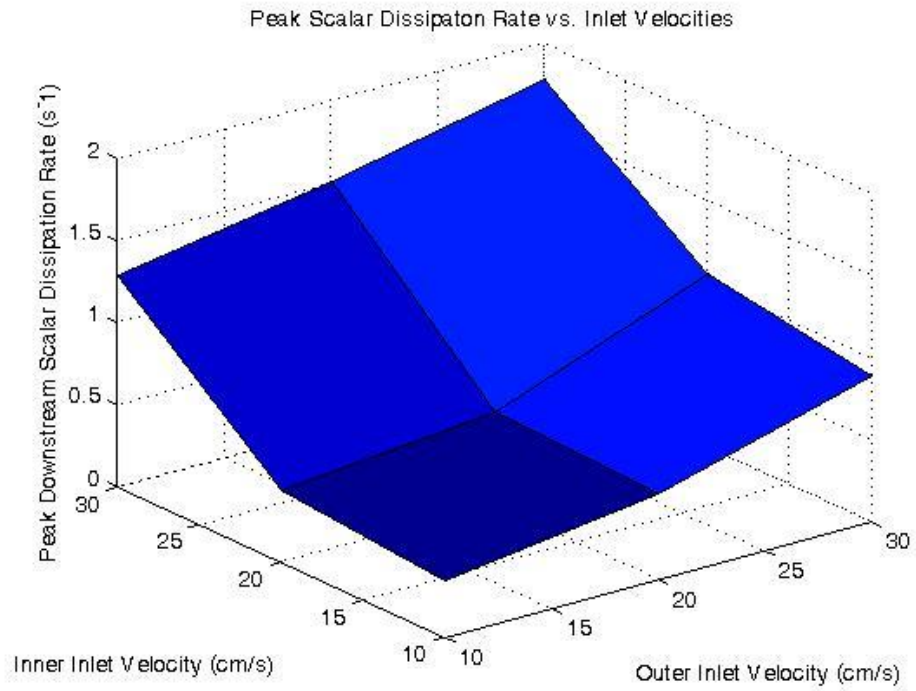

Figure 3.4 Peak downstream scalar dissipation rate for the 15 degree tapered burner with 1cm inner and outer inlets and 2cm settling section

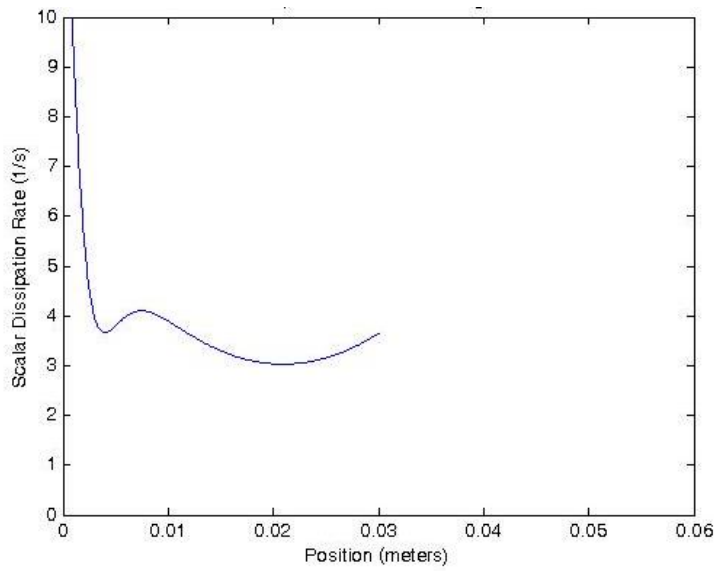

Figure3.5 10:30 Case 30 Degree Burner with no Settling Section

Table 3.1 Peak downstream scalar dissipation rate (s^{-1}) for the 15 degree tapered burner with 1cm inner

and outer inlets and 2cm settling section

Inner Flow Velocity (cm/s)	Outer Flow Velocity (cm/s)		
	10	20	40
10	0.343	0.525	0.886
20	0.434	0.558	1.059
40	1.288	1.511	1.781

Table 3.2 Peak downstream scalar dissipation rate (s^{-1}) for the 30 degree tapered burner with 1cm inner and outer inlets and 2cm settling section

Inner Flow Velocity (cm/s)	Outer Flow Velocity (cm/s)		
	10	20	40
10	0.455	0.761	1.401
20	0.607	0.868	1.435
40	1.491	1.692	1.955

Table 3.3 Peak downstream scalar dissipation rate (s^{-1}) for the 15 degree tapered burner with 1cm inner and outer inlets and no settling section

Inner Flow Velocity (cm/s)	Outer Flow Velocity (cm/s)		
	10	20	40
10	0.556	0.892	1.500
20	0.741	1.048	1.569
40	1.190	1.500	1.973

Table 3.4 Peak downstream scalar dissipation rate (s^{-1}) for the 30 degree burner with 1cm inner and outer inlets and no settling section

Inner Flow Velocity (cm/s)	Outer Flow Velocity (cm/s)		
	10	20	40
10	1.062	1.7	3.252
20	1.605	2.315	3.33
40	3.314	3.653	4.202

Convergent Nozzle with Angled Inlet Design Evaluation

A linear converging section with angled inlets that were positioned perpendicular to the wall was simulated (*Figure 3.1b*). This design proved to be similar to the geometry in the previous section. Varying burner angles and flow rates were tested (*Tables 3.5-6*). The peak scalar dissipation rates obtained in this geometry were higher than those obtained in the previous simulations (*Figure 3.6*),

however the burner did not meet the design goals. The desired scalar dissipation rate could not be obtained in laminar flow in this geometry with the required physical size. The peak scalar dissipation rates for these geometries all occurred at the burner exit. A peak scalar dissipation rate in the interior of the burner would allow for the formation of a flame edge in a region less sensitive to external effects.

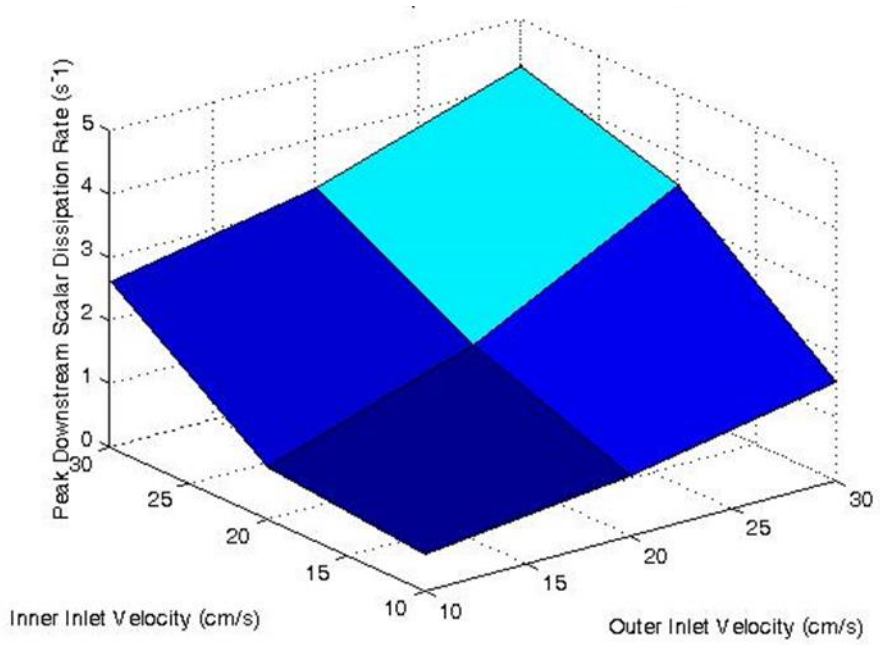

Figure 3.6 Peak downstream scalar dissipation rate for the15 degree tapered burner with 1cm inner and outer inlets and 2cm settling section and angled outer inlets

Table 3.5 Peak downstream scalar dissipation rates for the 15 degree burner with 1cm inner and outer inlets

Inner Flow Velocity (cm/s)	Outer Flow Velocity (cm/s)		
	10	20	40
10	0.598	0.948	1.556
20	0.829	1.868	3.546
40	2.624	3.210	4.282

Table 3.6 Peak downstream scalar dissipation rates for the 30 degree burner with 1cm inner and outer inlets

Inner Flow Velocity (cm/s)	Outer Flow Velocity (cm/s)		
	10	20	40
10	0.832	1.360	2.341
20	1.436	1.947	2.910
40	2.801	3.385	4.415

Straight Burner Design Evaluation

A straight slot burner with a fuel inlet and an air inlet at the end of the burner channel, a straight section for the flame to form in, side inlets for both fuel and air to increase the magnitude of the species gradient downstream, and a straight section to the exit of the burner was next modeled. The width of the inlets (w_U), side inlets (w_D), velocity of fuel and air, and location of the side inlets (l_s) were all varied to alter the peak scalar dissipation rate. The peak downstream scalar dissipation rate in this design occurred slightly downstream of the side jets (*Figure 3.7*). A parametric analysis of flow rates and burner geometries was performed (*Table 3.7*) (*Figures 3.8-11*). It was determined that the optimum geometry was 5 mm upstream inlets with 10 mm downstream inlets with a 15 mm settling length. This upstream width was chosen because decreasing the burner width led to an increase in peak downstream scalar dissipation rate. The 10 mm downstream inlets were chosen because the fittings that were to be used for the burner were about 8 mm in diameter. In this design, the settling section length was adjustable by replacing the splitter plate. The preliminary design also allowed for the adjustment of upstream inlet width (*Figure 3.12*).

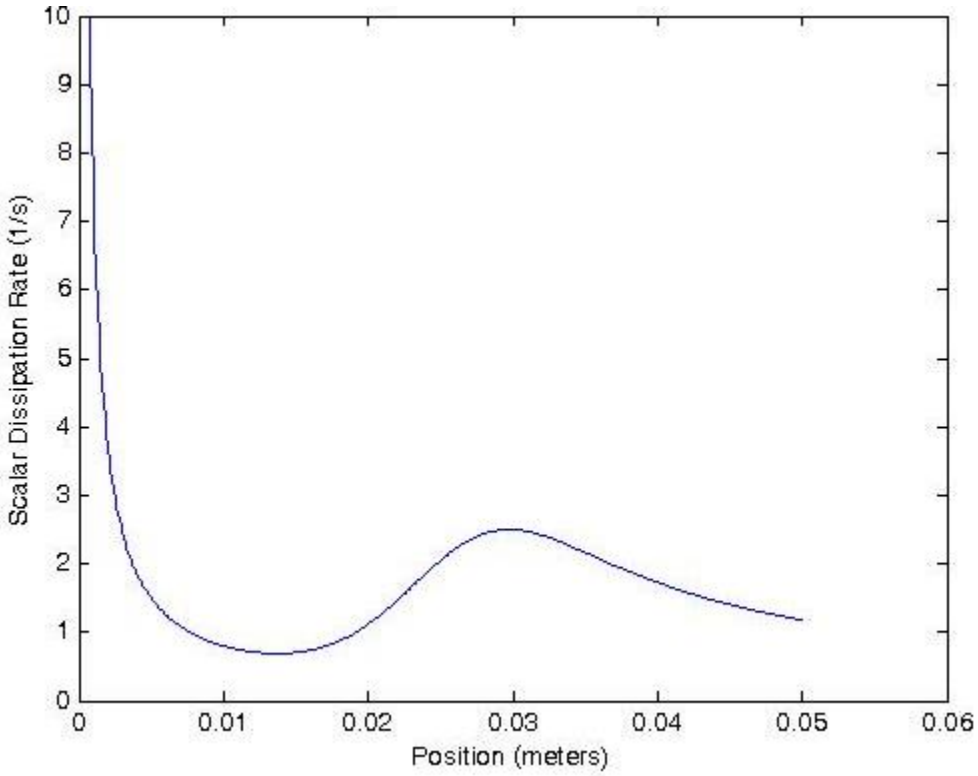

Figure 3.7 Scalar dissipation rate along the stoichiometric contour of the straight burner showing the peak 0.5 cm downstream of the inlet jet. The jet began at 1.5 cm downstream and ended at 2.5 cm.

Figure 3.8 Peak scalar dissipation rate as a function of inlet velocities for the straight burner with 1 cm upstream and downstream jets with a 1.5cm settling section

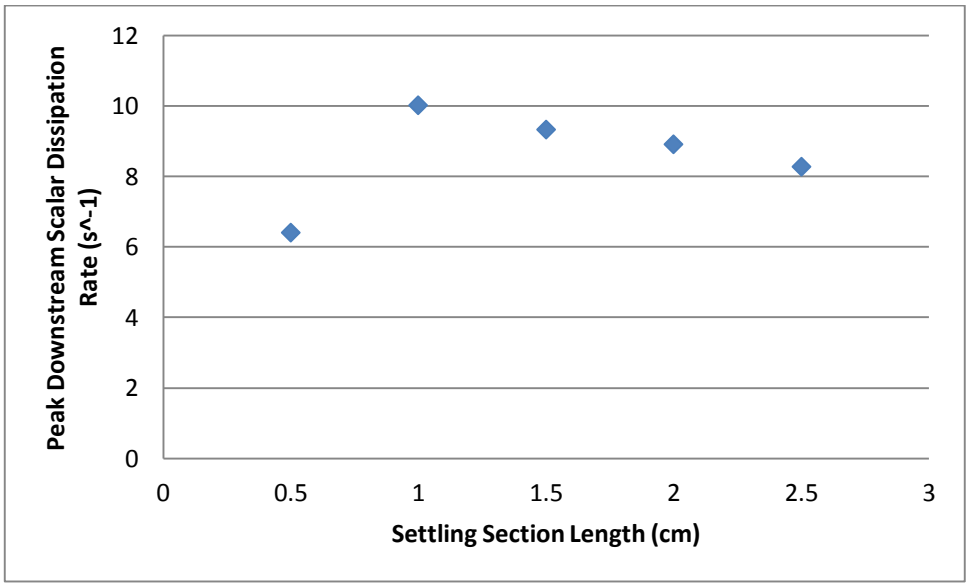

Figure 3.9 Peak downstream scalar dissipation rate versus settling section length with constant 1 cm downstream and upstream inlet widths and 10 cm/sec inlet velocities

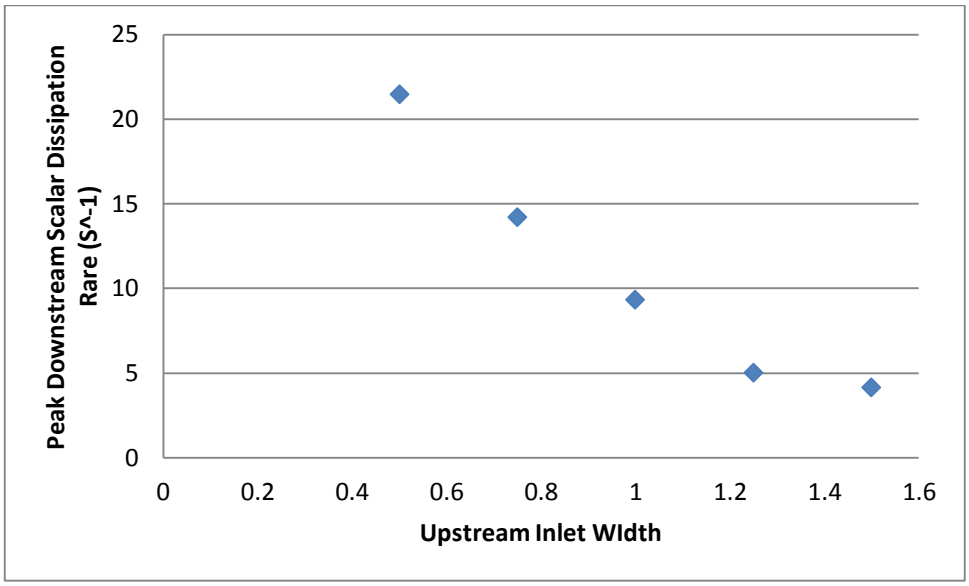

Figure 3.10 Peak downstream scalar dissipation rate for varying upstream inlet widths with constant downstream inlet width of 1 cm, 1.5 cm settling section, 10 cm/sec upstream velocity and 80 cm/sec downstream velocity

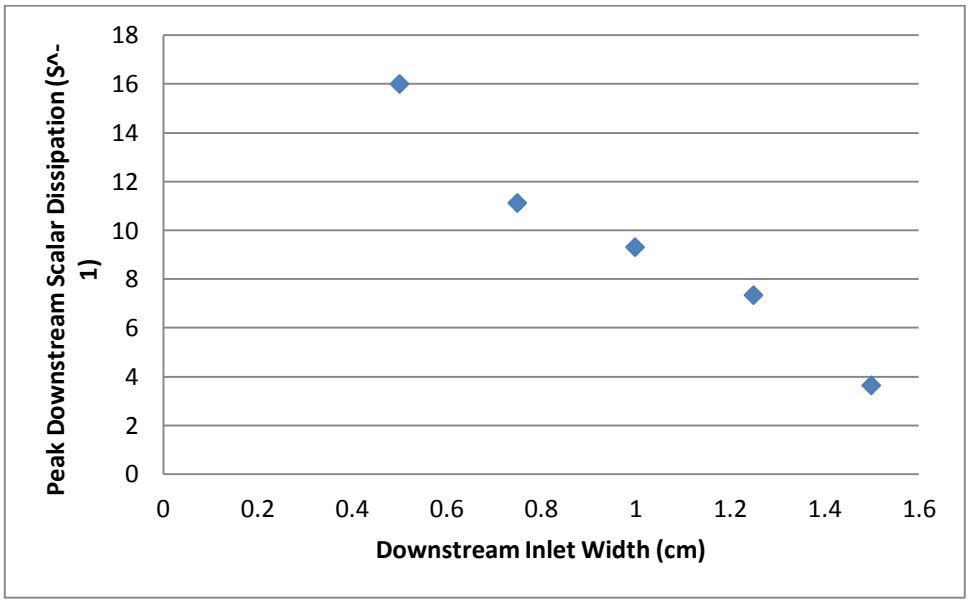

Figure 3.11 Peak downstream scalar dissipation rate for varying downstream inlet width. Downstream inlet Reynolds number was held constant in this study. Upstream inlet if 1cm, 1.5cm settling section, 10 cm/sec upstream inlet velocity and downstream inlet Reynolds number 510.

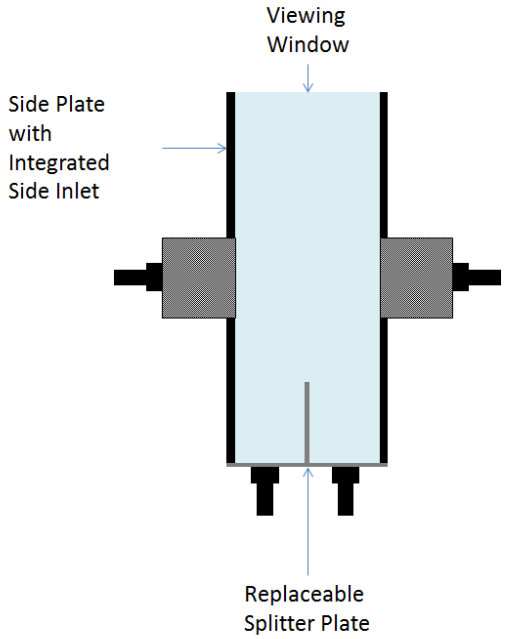

Figure 3.12 2-Dimensional preliminary burner design sketch depicting variable geometry features

	Downstream Inlet Velocity			
Upstream	10	20	40	80
10	0.588	1.0434	2.1831	9.3185
20	0.8682	1.1265	2.1674	7.9096
40	1.6	1.7761	2.4455	4.6978
80	3.0578	3.2407	3.6277	5.113

Table 3.7 Peak downstream scalar dissipation rate (s^{-1}) with 1 cm upstream and downstream inlets and 1.5cm settling section

Reacting Simulations

Reacting simulations were next performed in the burner geometry selected in the previous section. This simulation used 20% diluted methane to match the fueling in the burner previously built by Carnell and Renfro (Carnell 2006). The walls were modeled as constant temperature at 300K. A finite width splitter plate was modeled to provide a wake for the flame to stabilize in. The preliminary splitter plate temperature was chosen at 1250 K, and the width was selected as 3.175 mm to match the design. Simulations with and without the splitter plate were examined (*Figures 3.13-14*), and it was determined that the attached flame that was observed with the splitter plate was preferable to the lifted flame that would be observed if an infinitesimally thin splitter were used. These simulations were both performed

using 10 cm/sec upstream inlets and 80 cm/sec downstream inlets. Plots of temperature and scalar dissipation rate were generated for the finite width splitter case in order to compare them with the literature (*Figure 3.15-16*).

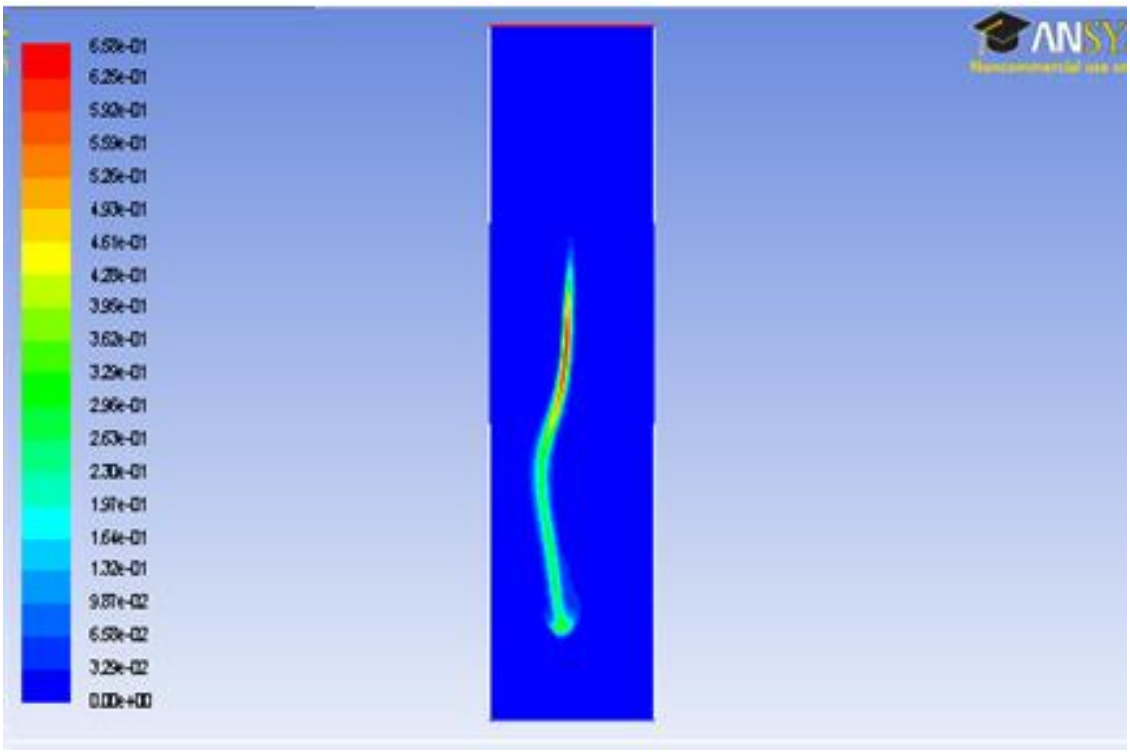

Figure 3.13 Simulated reaction rate for slot burner with infinitesimally narrow splitter plate. This flame has both a forwardly propagating tribrachial edge at the stabilization point and a negative edge at the impinging side jets

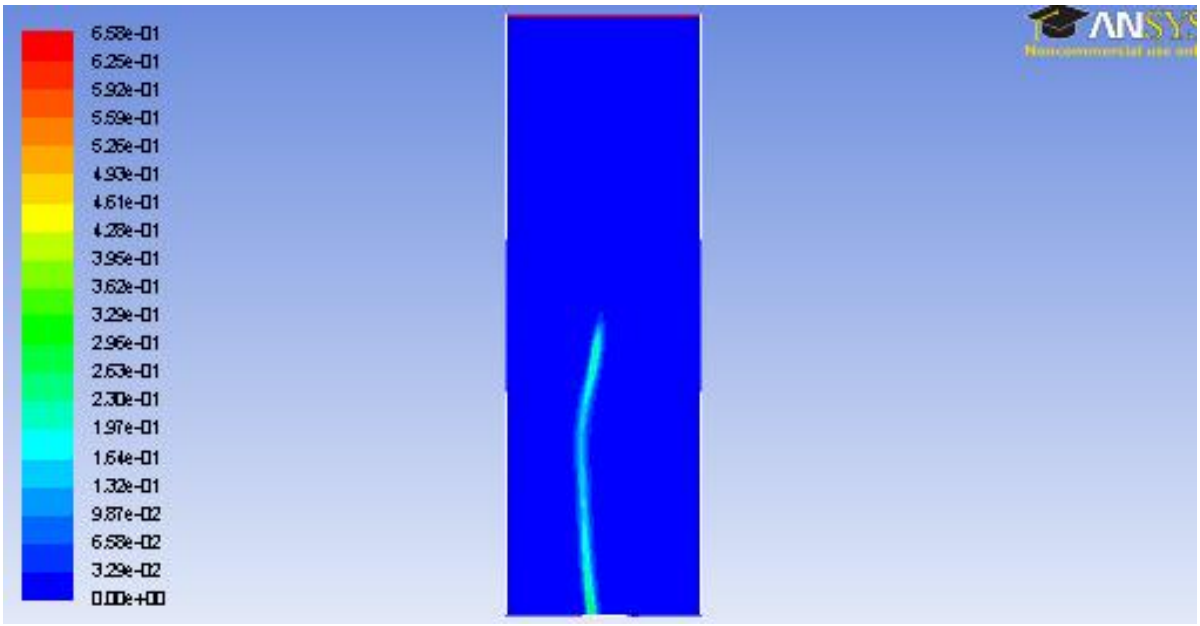

Figure 3.14 Simulated reaction rate for the slot burner with finite width splitter plate showing attached diffusion flame and negative edge.

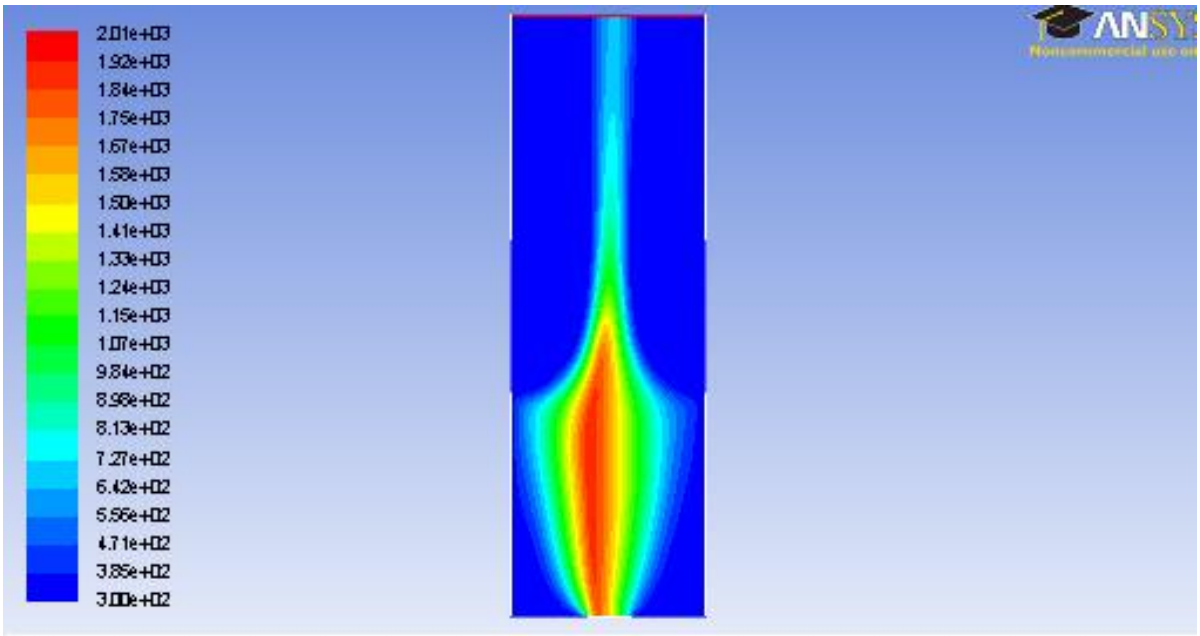

Figure 3.15 Temperature contour for the reacting simulation with finite width splitter plate

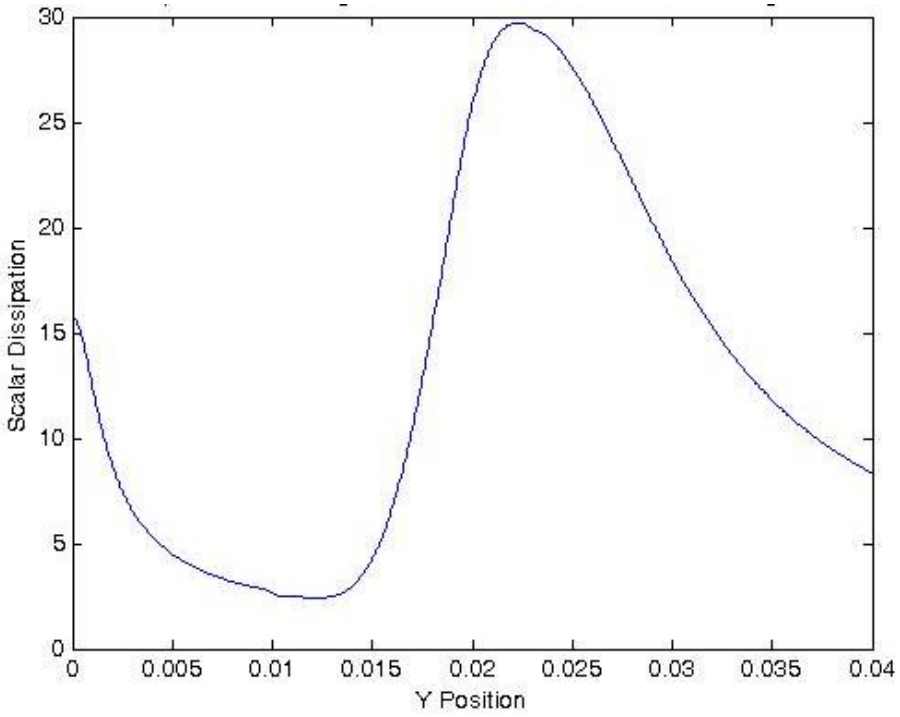

Figure 3.16 Scalar dissipation rate along the stoichiometric contour for the reacting simulation presented above. This curve exhibits a scalar dissipation rate of 17s^{-1} in the vicinity of the predicted flame edge.

Burner Construction and Revised Design

In an attempt to create the proposed burner geometry, it was found that it was difficult to create the adjustability desired while maintaining the geometric tolerances for straightness of the side plates. This was due to difficulties in welding the inlets in the side plates. It was determined that the burner should be made from standard 304 stainless steel rectangular stock. This led to an updated burner width of 15 mm upstream and downstream inlets. This burner more readily accommodated the use of Swagelok® brand tube fittings that allow for easy hook-up to the existing flow system. The entire burner was made from 304 stainless steel and fused silica was used for the viewing windows to allow for the transmission of UV light useful in many optical diagnostic techniques.

After constructing the burner, a laminar extinction edge was observed operating at 15% fuel with 4 cm/sec upstream inlet velocity and 80 cm/sec downstream inlet velocity (*Figure 3.17)*, but it was found that the burner was extremely sensitive to thermal effects in this case. The diffusion flame was not

stable unless the splitter plate was heated extensively, and this was not desirable for the research performed in this thesis. The sensitivity of the flame to the splitter plate temperature was alleviated by using an increased fuel concentration in the fuel streams. A fuel concentration of 35% proved to be the minimum for repeatable attachment of the flame to the splitter plate. In order to create an extinction edge at this fueling, it was necessary to operate the burner at flow velocities where the flow in the region of the flame edge became turbulent. The characterization of the flow field in this burner for four different cases in which a negative edge flame is presented in the remainder of this thesis.

Figure 3.17 High speed camera image (left) and point and shoot camera image (right) of stabilized laminar flame edge in final burner geometry

Chapter 4: Experimental Setup

Burner Geometry

The burner used in this study was constructed from 304 stainless steel tube stock. The outer dimensions of the stock were ¾"x1.5" with 0.065 wall thickness. The burner is 6 inches long. The side inlets are constructed of ¾" by ¾" stock with 0.065 inch wall thickness and are 3 inches long. A bolt-on splitter plate was constructed from 1/8th inch 304 stainless steel sheet. ¼ inch thick quartz glass viewing windows form the front and back of the burner. ¼ inch Swagelok tube fittings were used to introduce gases into the burner. Fine aluminum honeycomb ½ inch thick with hex cell size of 1/16th of an inch was located near the inlet exits to help ensure a uniform velocity profile (*Figure 4.1*). This burner geometry yielded 15.8 mm square inlets both upstream and downstream, which was the closest practical size to the computational geometry.

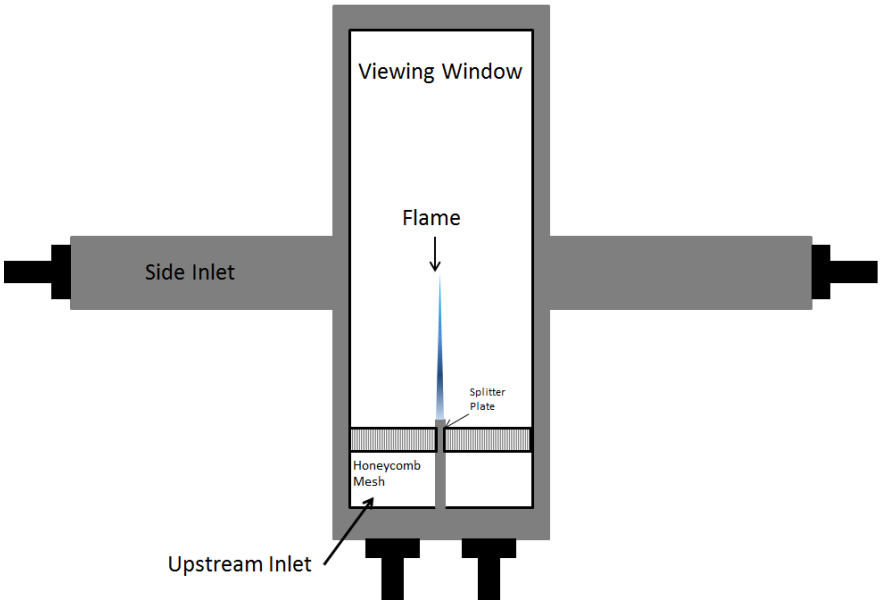

Figure 4.1 Cartoon of burner geometry

Gas Supply and Flow Control

Gaseous oxygen (Airgas OX ED300), gaseous methane (Airgas ME CP300), and the gas from a liquid nitrogen tank (Airgas NI 240LT230) were regulated from tank pressure using two stage regulators to 120

psi. These gases were piped into the inlet fittings of a custom digital flow bench (*Figure 4.3*) using ½ inch plastic tubing. This digital flow bench (*Figure 4.3*) consists of ten ControlAir 500-EH digital pressure regulators controlled by a LabView instrument through a MCC USB-3105 DAQ board. Each regulator received a 0-5 V analog signal from the DAQ system which is used to set the output pressure of the gas. The pressure regulators use a bleed line to vent excess pressure when necessary. For channels that handled flammable gasses, the ControlAir 500 regulators regulated the pressure of nitrogen, which was used to control an AeroCon Model 1026 dome loaded regulator to prevent bleeding of fuel into the lab. The dome loaded regulator is a passive device that transfers the pressure from one stream (nitrogen) to another (fuel) and does not use a bleed vent. The flow bench also includes a feedback loop ensuring accurate pressures. This consists of a Cole Parmer 68075-48 pressure transducer read by a PCI 6035 DAQ card. The output from each of the regulators is split and piped simultaneously to choked orifice that converts the controlled pressure into a controlled flow rate. The second output from the pressure regulator is sent to a bank of 10 Clippard EV-2M solenoids (one for each flow channel) that lead to a common manifold in which the pressure transducer is mounted. These solenoids are driven by a SainSmart 16 channel relay board, which is driven by a LabView VI through a Measurement Computing USB-1208 DAQ board. The desired flow rates for each gas are entered into a master Labview program which converts each flow rate to a desired control pressure (via input calibrations). The program sequentially sets the analog output on each gas channel to the control value for that pressure and opens the solenoid valve for that channels so that the actual pressure can be read. Changes to the voltage output are made to control to the desired pressure and each channel is altered in a continuous sequence using a PID control in a LabView VI. The total time for updating all 10 flow channels is approximately 100 seconds. Once the gases have flowed through the choked orifices, they are piped into the burner inlets.

The output from the pressure transducer for each channel was calibrated to a volumetric flow rate using either an American Meter company DTM-200A dry flow test meter or a Bubble-O-Meter 10-100-1000 ml meter. The back pressure was measured using an SSI MediaGauge Digital pressure gauge accurate to 0.1 psi for the dry flow test meter. These calibrations were input to the master Labview program.

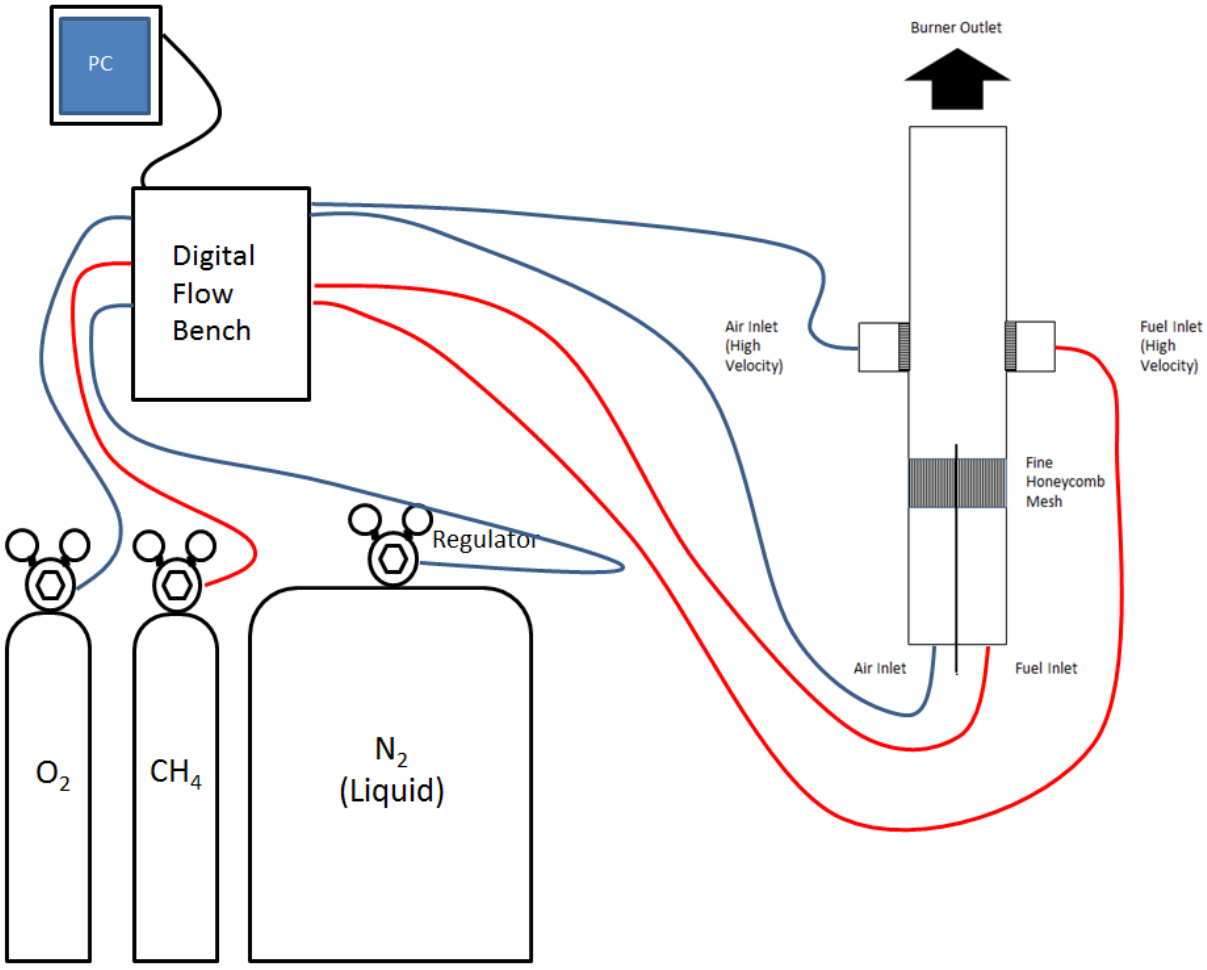

Figure 4.2 Main experimental setup diagram

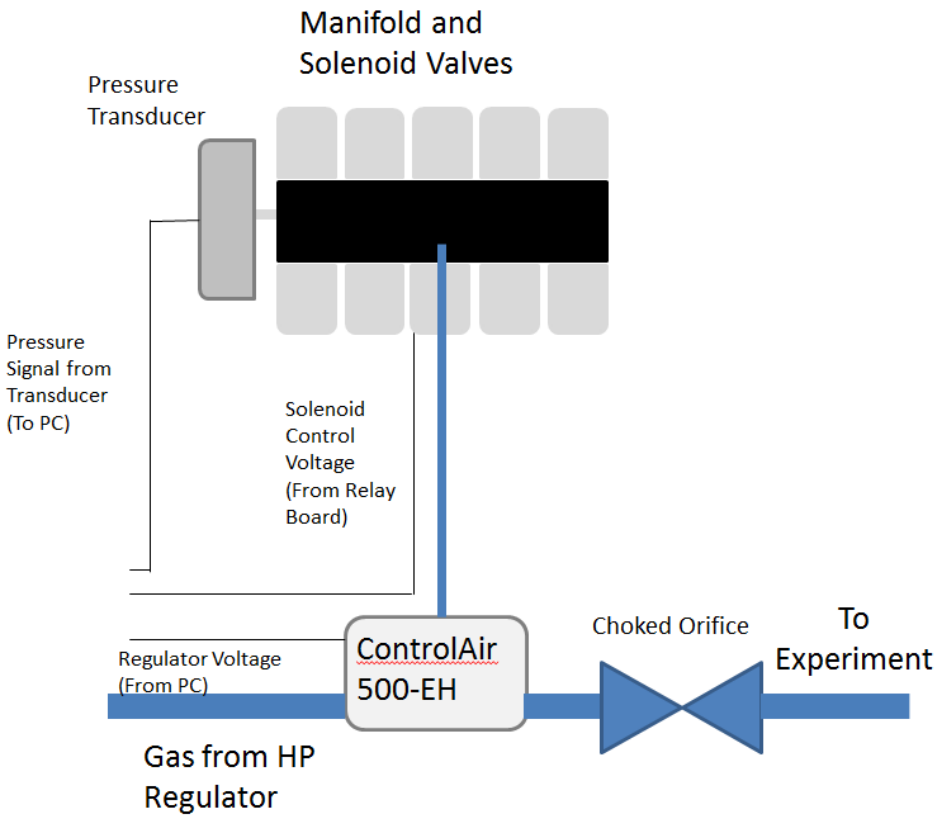

Figure 4.3 Diagram of one nonflammable gas channel of the 10 channel digital flow bench

PIV Background and Required Equipment

Particle imaging velocimetry (PIV) is a non-intrusive optical diagnostic technique that utilizes a pair of Mie scattering images (*Figure 4.4*) to obtain a velocity field (*Figure 4.5*). In this thesis two dimensional PIV is used, so the velocity field acquired is located on a plane. The images used to perform the PIV analysis are formed by Mie scattering from seed particles. These seed particles are small liquid or solid phase particles injected into the flow field that follow it with sufficient accuracy to be representative of the gas velocity. A laser pulse is formed into a sheet and shone through the test section. This laser light is scattered by the seed particles, and the scattered light is collected by a lens and imaged with a camera. A short time later (on the order of microseconds) another laser pulse is fired, and the image is collected and stored on the camera. In order to perform these actions within the required time, usually a dual head laser is required. The camera used in this type of measurement is usually a CCD camera with

frame straddling capabilities. This allows the camera to take two images before the CCD array needs to be read out.

After the two images are processed, the images are divided up into interrogation windows. Then a cross-correlation algorithm is applied between the first and second frames in each interrogation window. This algorithm provides the most likely displacement of the seed particles (in pixels). The velocity of the flow is calculated by dividing the displacement of the particles by the inter-frame delay time. From this, an instantaneous vector field of velocities is formed. In this study this vector field is used to compute the average velocity field and turbulence statistics of interest including turbulent kinetic energy and integral length scales. This analysis will be presented later in this thesis.

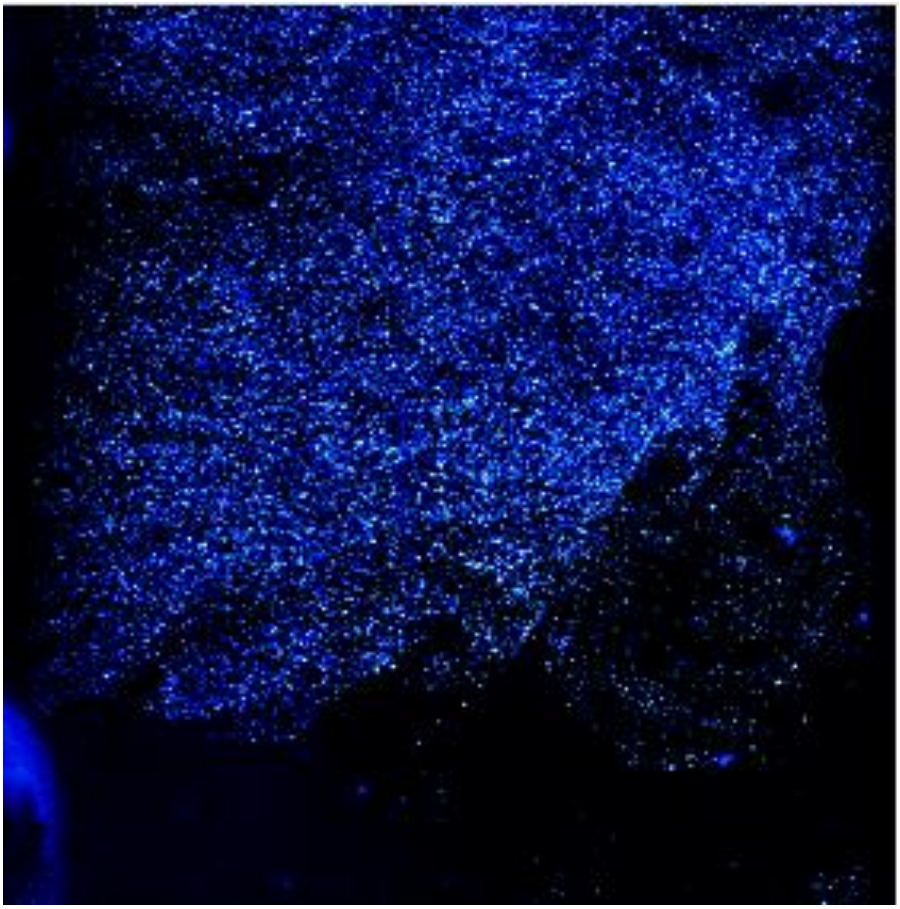

Figure 4.4 Sample Mie scattering image

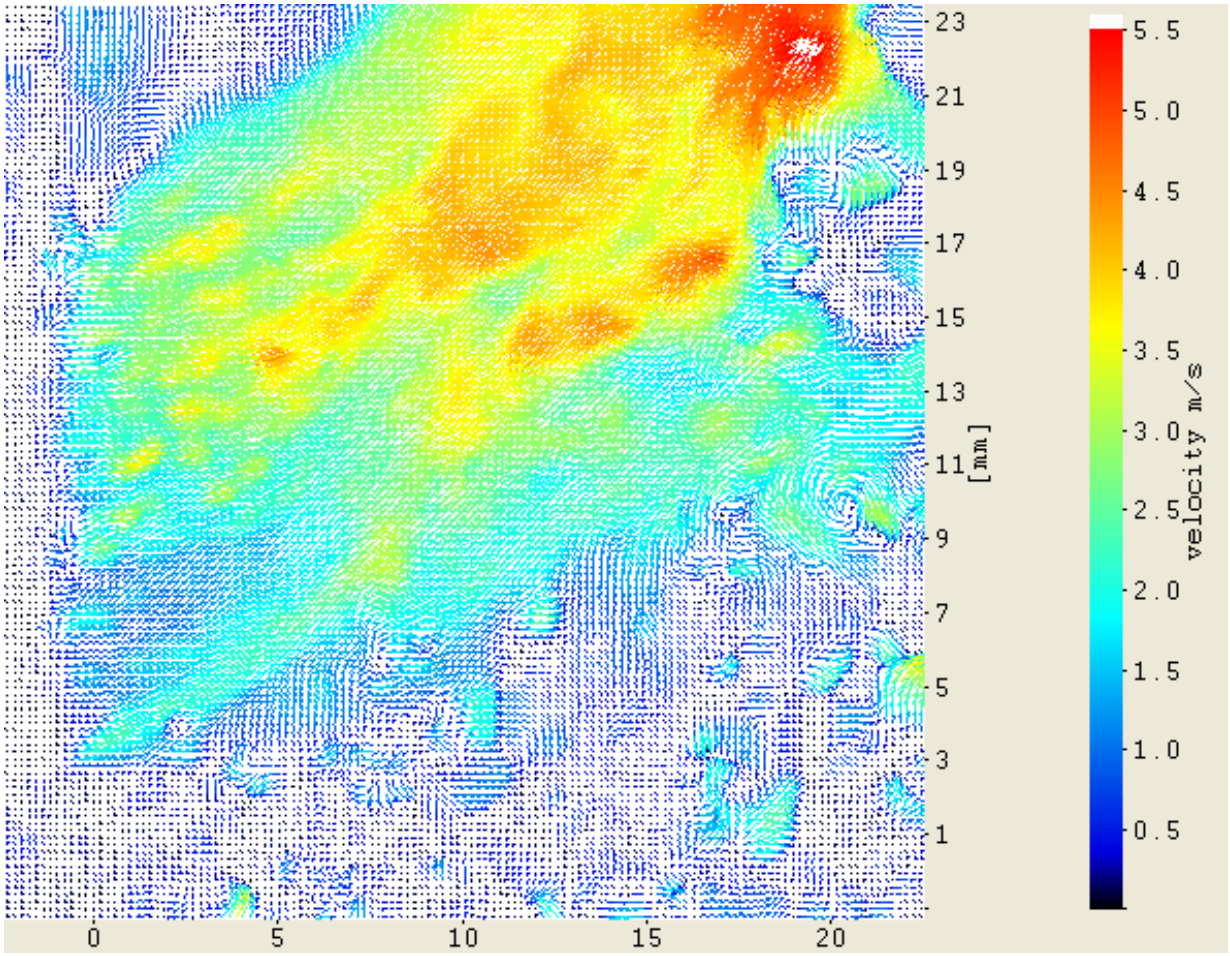

Figure 4.5 Sample instantaneous velocity field

PIV Experimental Setup

During the acquisition of Mie scattering images used for PIV, it is necessary to seed the flow field. In this experiment, it was important for the seed particles to withstand the high temperatures found in the flame region. For this reason, aluminum oxide powder was selected for the seed material. The seed was #1 micro alumina with a nominal particle size of 1 micron, purchased from the KC Abrasive Company. The seed was introduced into the flow between the choked orifice bank in the digital flow bench and the burner inlets. This was performed using seeders made from PVC pipe (*Figure 4.6*). The inlet fitting for the seeder was installed so the flow of the incoming gasses was nearly tangential to the wall of the

tubing to generate a swirling effect. Fine mesh screens were installed below the top cap to prevent large clumps of seed from exiting the seeder. Each burner inlet had its own seeder. These seeders were agitated using mechanical vibrators powered by shop air at 85 psi which provided 45 pounds of force at 350 Hz. This was to prevent seed particles from clumping. To further prevent clumping, the seed was baked at 400 K for 12 hours and allowed to cool prior to use.

Two different commercial PIV systems were used in collecting the flow field information presented in this thesis. The data presented in Chapter 5 was collected using a LaVision FlowMaster 3S CCD camera with a 532 nm band pass filter with a full-width half-max of 0.5 nm mounted on a UV-Nikkor 105mm f/2.8 lens. This removed ambient light and chemiluminescence from the raw Mie scattering images. In this system, a New Wave Solo III dual cavity laser was used to create the light sheet (*Figure 4.5*). This laser provided 50 mJ per pulse at 10 Hz. The camera and laser were controlled by a LaVision programmable timing unit controlled by Davis 7.0 software. The PIV measurements were taken at 1 Hz with an inter-frame delay time of 75 microseconds. The images were processed in LaVision Davis 7.2 software using interrogation windows of 16x16 pixels with 50% overlap. A multi-pass deforming window technique was used. This provided a spatial resolution of 141 microns between 16x16 pixel interrogation windows. The individual pixel size is 17.6 microns.

Due to a required repair of the New Wave laser, a second PIV system was used to acquire the data presented in Chapters 6 and 7. The New Wave Solo-III was replaced with a Dantec Dynamics DualPower 200-15 PIV dual cavity laser. This laser provided 200 mJ per pulse at up to 15 Hz. A Dantec Dynamics FlowSense 4M MkII camera was used to acquire the Mie scattering images through a 105mm Nikon f/4 lens. A 532 nm band pass filter with a full-width half-maximum of 0.5 nm was used for the data in Chapter 6, while the filter was removed to capture the chemiluminescence from the flame in Chapter 7. These measurements were taken at 6 Hz with an inter-frame delay of 100 microseconds. The raw Mie

scattering images were exported to bitmap format images, and imported into DaVis 7.2 software, where the processing was performed. 64x64 pixel interrogation windows were used with 50% overlap. A multi-pass deforming window technique with decreasing window size was used. The spatial resolution for this measurement is 509 microns between each 64x64 interrogation window. Each individual pixel is 15.9 microns

In both cases, the laser pulse was reflected by two 2-inch and three 1-inch laser line mirrors. This brought the laser beam into the test section. The laser beam was focused using a 1.5-inch diameter 500 mm focal length plano-convex lens. The beam was expanded in one dimension using a -50 mm focal length, 1-inch diameter plano-concave cylindrical lens. The resulting laser sheet was equivalent in width to the test section at 35 mm. The laser sheet thickness was approximately 1.2 mm (*Figure 4.7*). With this laser sheet thickness and the longest inter-frame delay of 100 microseconds, out of plane velocities of up to 12 m/s can be tolerated without losing seed particles. The Mie scattering images were collected using an f-mount Nikon lens with 105mm focal length. A 2-inch diameter laser line filter was mounted on the front of this lens. (*Figure 4.8*)

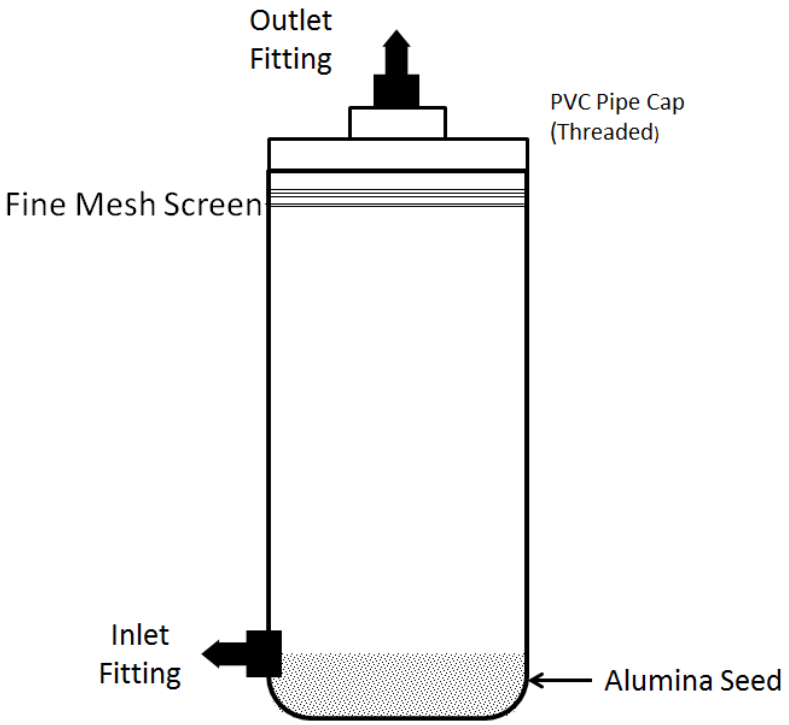

Figure 4.6 Seeder Schematic

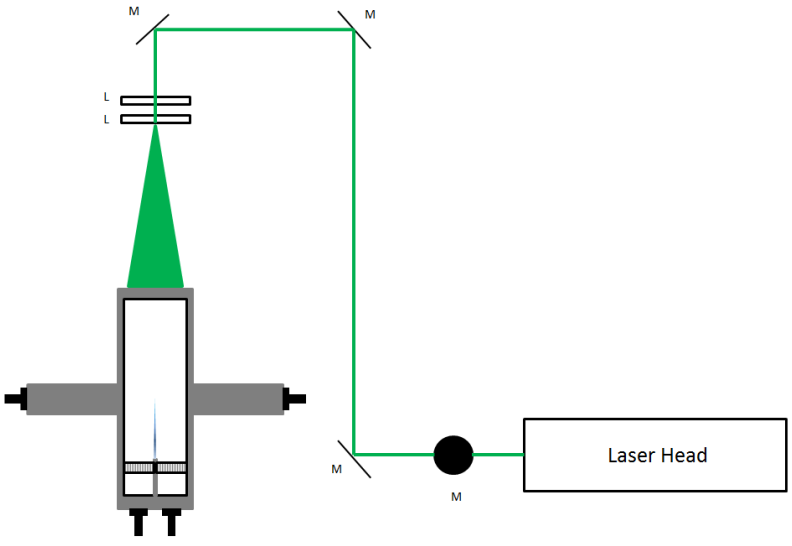

Figure 4.7 Diagram of optics to form laser sheet in the burner

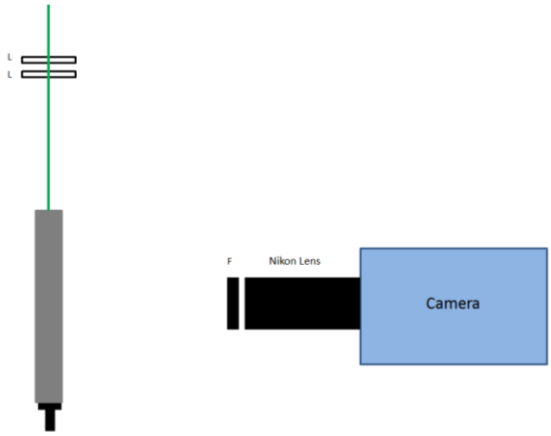

Figure 4.8

Chapter 5: Side Jet Characterization

In preliminary attempts to perform PIV measurements on the entire flow field inside the burner, it was determined that adequate spatial resolution to resolve the turbulent structures in the side jet entrance region was not present in measurements made across the whole test section. This resolution is important for future computational work, as the boundary conditions for the jet inlet could have a significant effect on the numerical solution. In addition, considerable difficulty was encountered with seed adhering to the viewing windows when all four inlets were seeded. Because of these difficulties, a PIV study of the side jet only was performed to characterize the flow field in and around the entry region of the jet. This was performed with an extinction edge flame inside the burner, and the flow conditions are identical to those in later study. These flow conditions are denoted (Upstream Velocity (cm/sec): Side Jet Velocity (cm/sec)). For this set of PIV images, the jet entry in the burner is approximately located at x=-1 mm and y=3 mm -18 mm. In this study, turbulence statistics were calculated from the individual PIV images, including turbulent kinetic energy. A total of 2400 instantaneous velocity fields were acquired for each experimental condition. This was adequate to provide statistical convergence of the turbulent kinetic energy field (*Figure 5.1*), which shows changes in the average turbulent kinetic energy of each additional instantaneous image. The percent change in the turbulent kinetic energy field was calculated by taking the change observed in the average for each new image element by element for each additional image and dividing that difference from the average of each individual element. The maximum value in the whole field was used as the percent change in the turbulent kinetic energy field. No element was found to change by greater than 0.5% with 1600 vector fields input into the processing code.

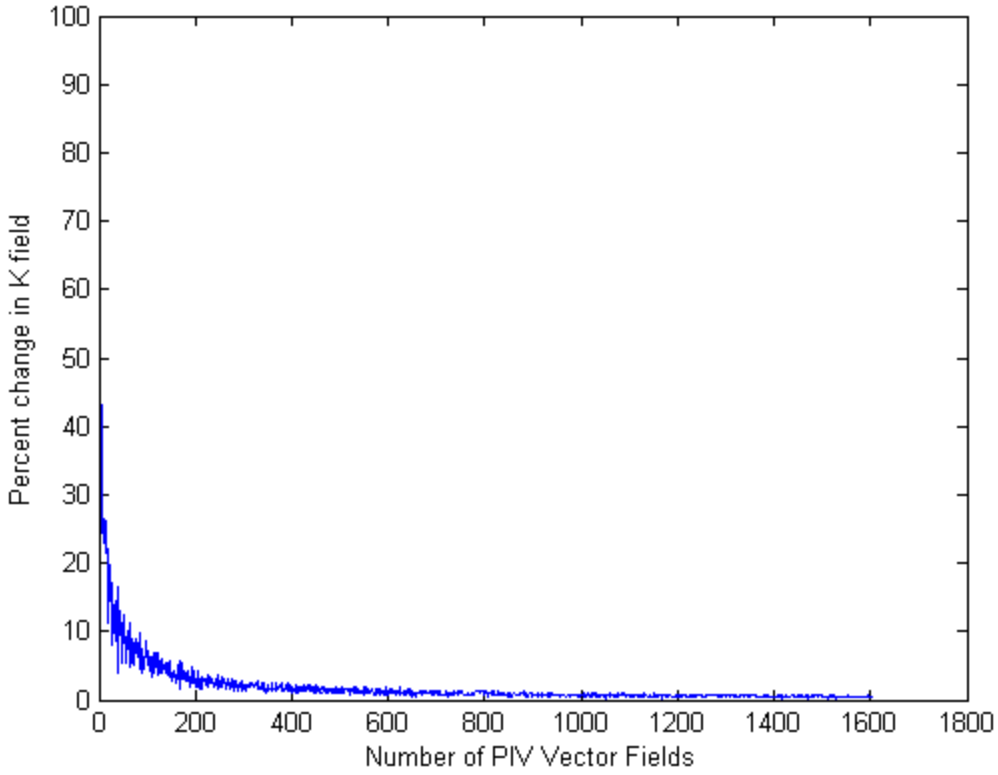

Figure 5.1 Convergence history for the turbulent kinetic energy field showing adequate statistical convergence with 1600 input velocity fields. 2400 fields were used in the final calculations for this thesis.

Mean Velocity Fields

From an ensemble of 2400 instantaneous velocity fields for each of the experimental conditions tested, a time averaged velocity field was calculated (*Figures 5.2-5.5*). The jet inlet velocity conditions were extracted along the line x=0, and polynomial fits are provided for detailed boundary conditions for future CFD simulations. (*Table 5.*1)(*Equation 5.1*). The honeycomb mesh that was used as a flow straightener in the jet exit into the test section was observed to cause a periodicity in the inlet velocity profile (*Figures 5.6-5.9*). The periodicity of the velocity profile is approximately equal to the spacing of the honeycomb grid. The fluctuation of the profile is a maximum of 8% from the fit velocity profile.

The jet deflection as a function of varying jet velocity with constant main inlet velocity is shown using streamlines originating from the center of the jet (*Figure 5.10*). The higher the jet velocity, the less the

jet is deflected. This is due to the higher ratio of jet momentum to main channel momentum. A lower velocity jet is deflected downstream more readily.

The flame edge is located between y=10 and y=20 mm within 5 mm of the jet center plane, which is at x=17 mm. It is clear that this region has high positive velocity in the y direction, which suggests the existence of a negative edge flame. Since only the left jet was seeded, the velocity information to the right of the burner center plane may not be complete. This may account for the positive x velocity in the average field, even though the velocity is expected to be zero in the x direction somewhere near the center plane of the burner. The detailed flow conditions in this region are studied in greater detail in Chapter 6.

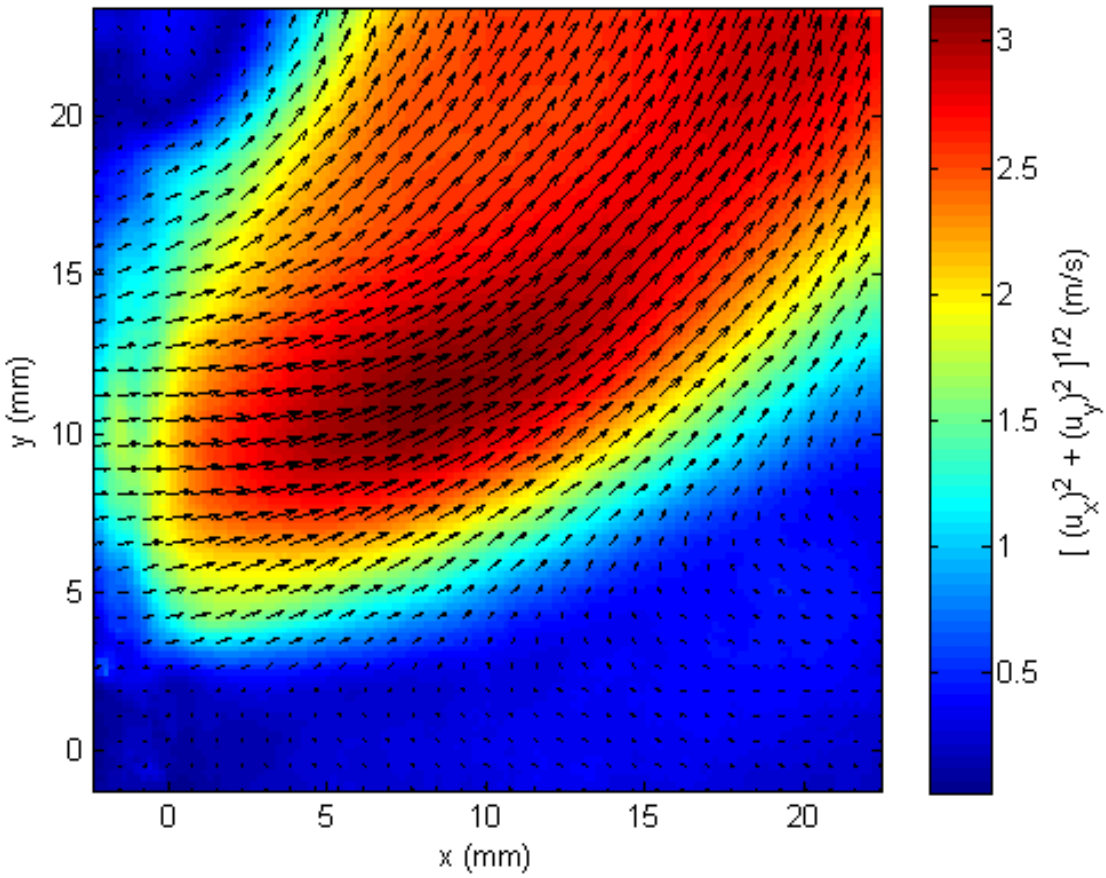

Figure 5.2 Average velocity field for the 40:180 case

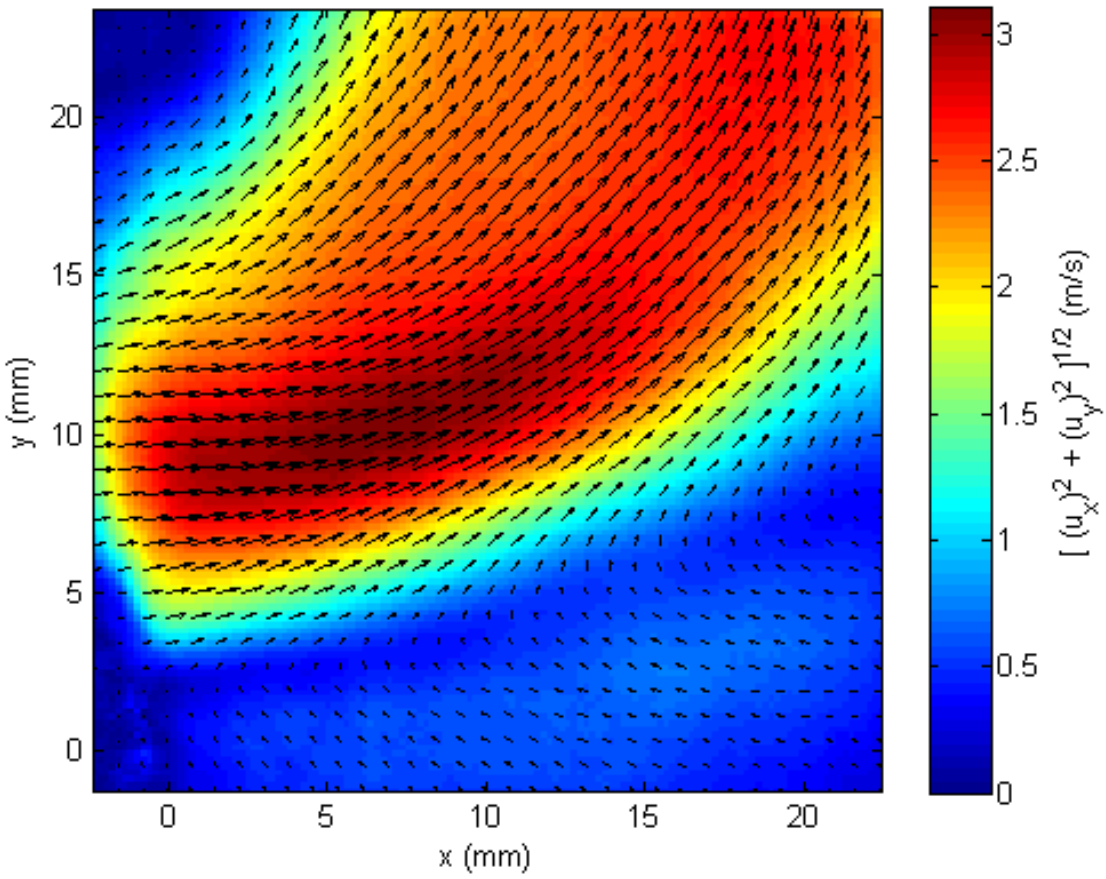

Figure 5.3 Average velocity field for the case 20:400

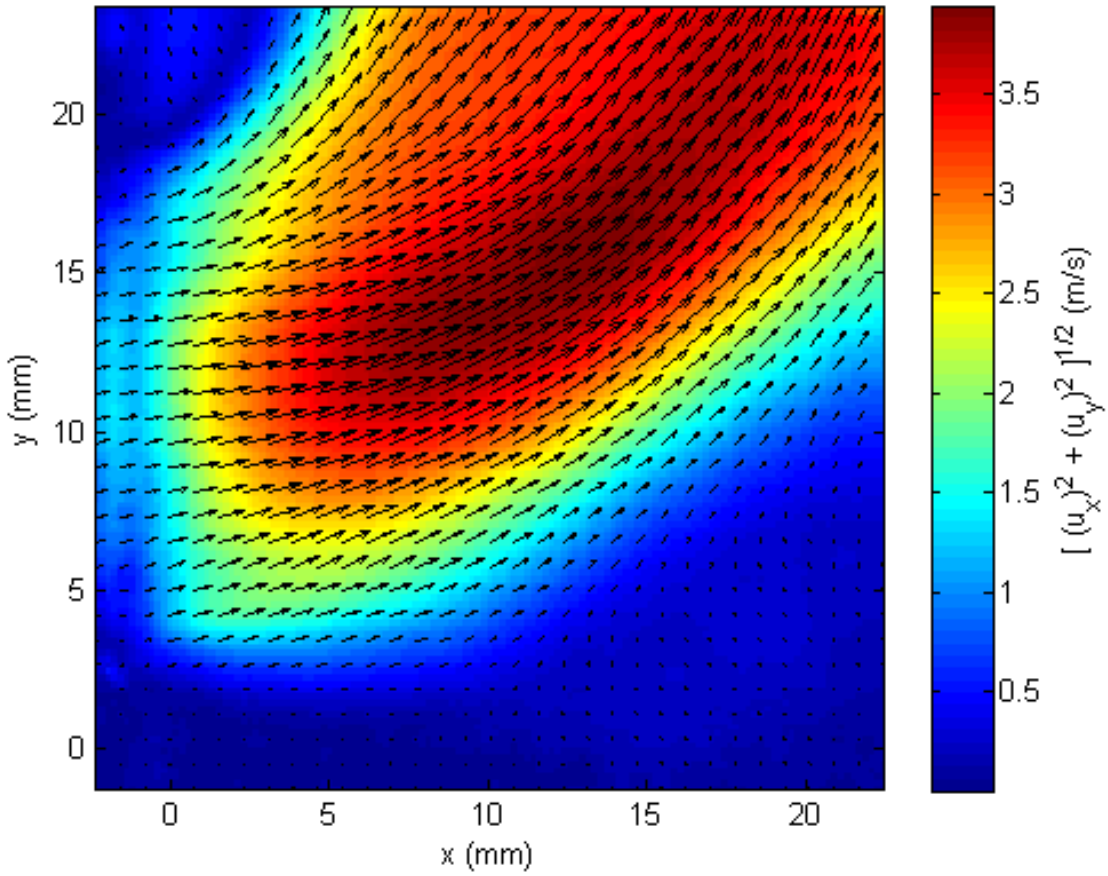

Figure 5.4 Average velocity field for the case 40:220

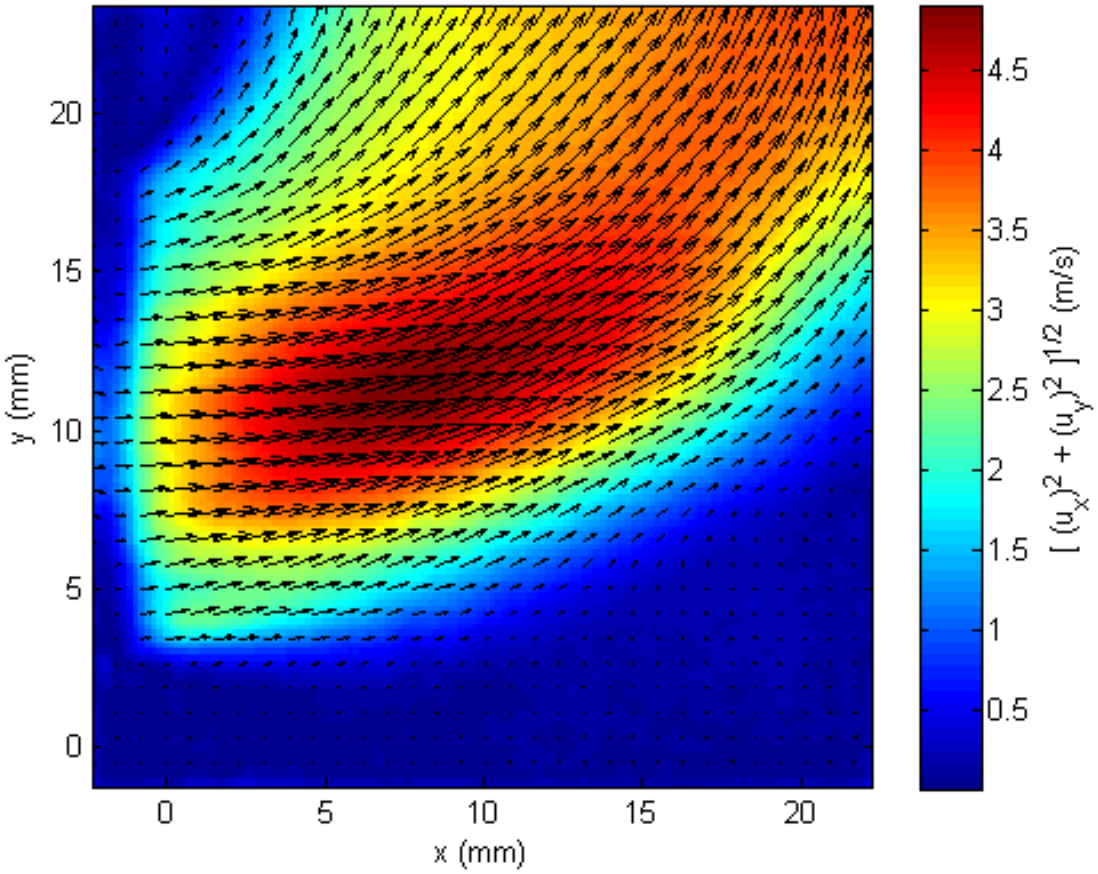

Figure 5.5 Average velocity field for the case 40:240

Table 5.1 Constants for polynomial inlet velocity fits

Case	K1	K2	K3	K4	K5
40:180	6.93E-06	1.50E-03	-5.92E-02	5.21E-01	9.79E-01
40:200	2.63E-06	3.00E-03	-9.94E-02	8.22E-01	8.03E-01
40:220	1.96E-04	-6.40E-03	4.36E-02	2.02E+02	1.41E+00
40:240	2.56E-04	-6.60E-03	1.83E-02	3.22E-01	1.75E+00

$$V = K1 * y^4 + K2 * y^3 + K3 * y^2 + K4 * y + K5$$

Equation 5.1 Functional form for inlet velocity profile fits

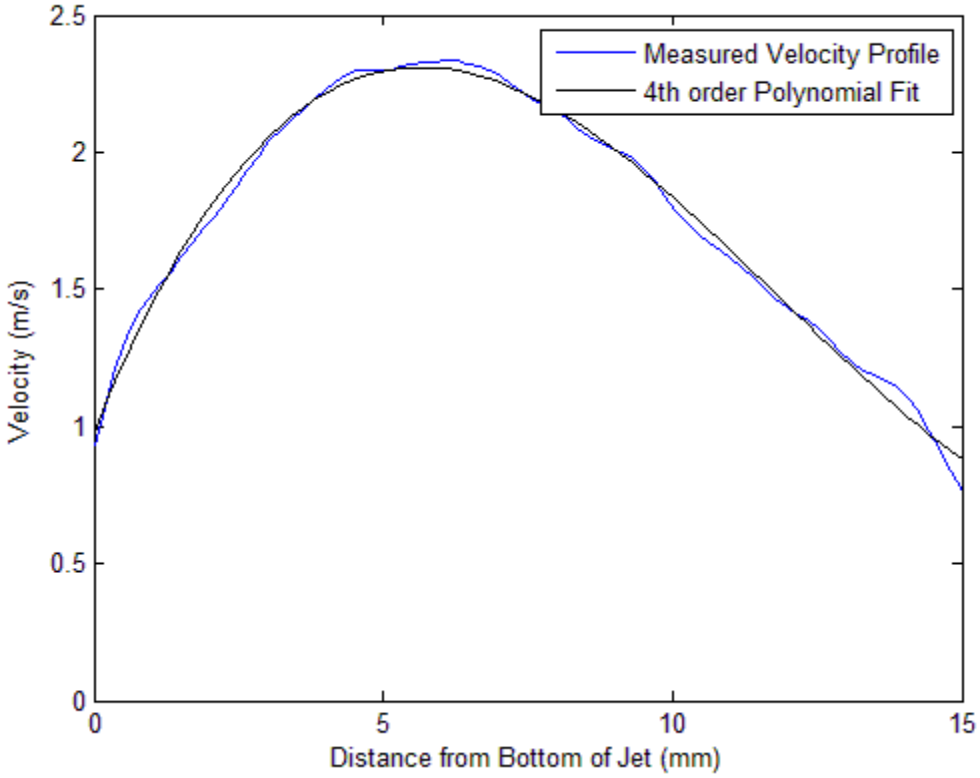

Figure 5.6 Measured and fit inlet velocity profiles for the case 40:180

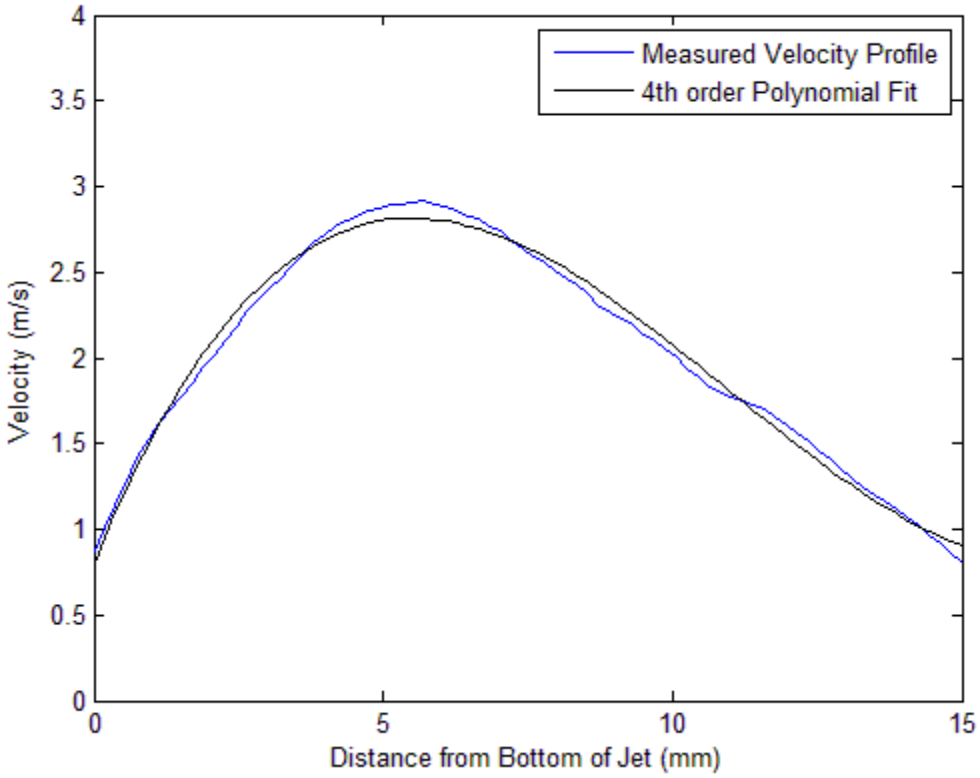

Figure 5.7 Measured and fit inlet velocity profiles for the case 40:200

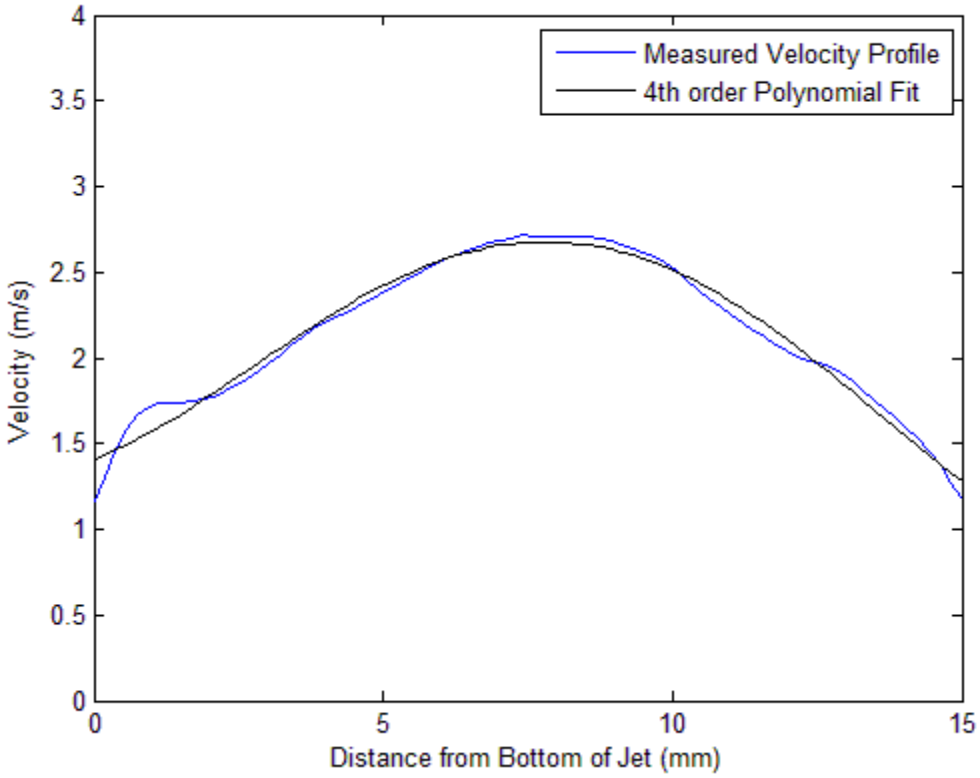

Figure 5.8 Measured and fit velocity profile for the case 40:220

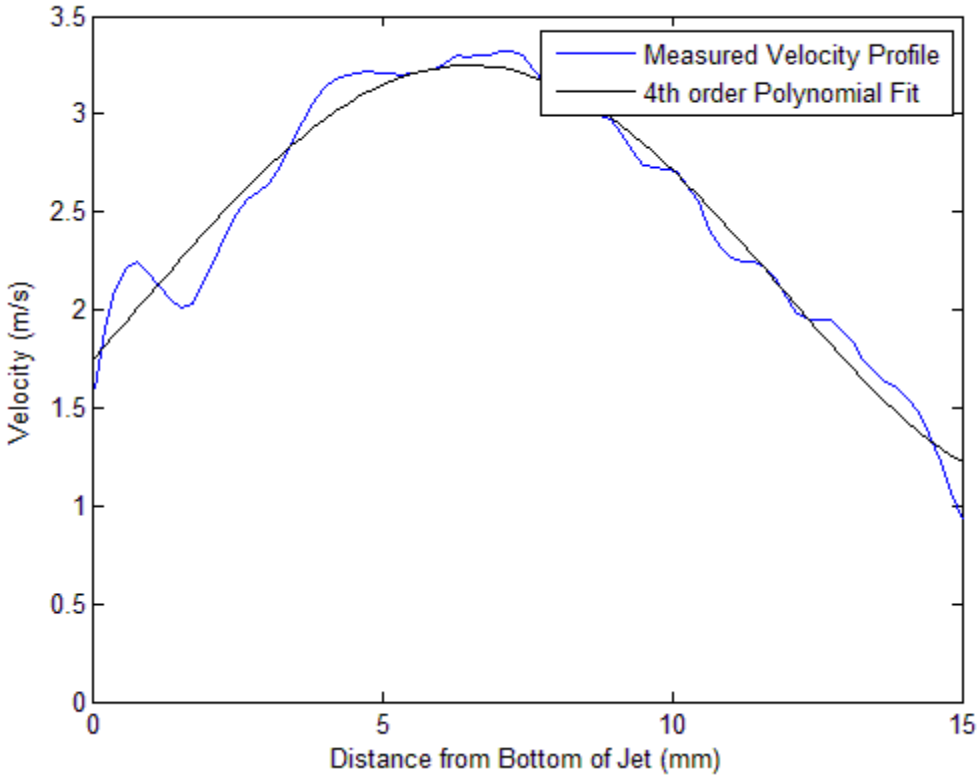

Figure 5.9 Measured and fit inlet velocity profiles for the case 40:240

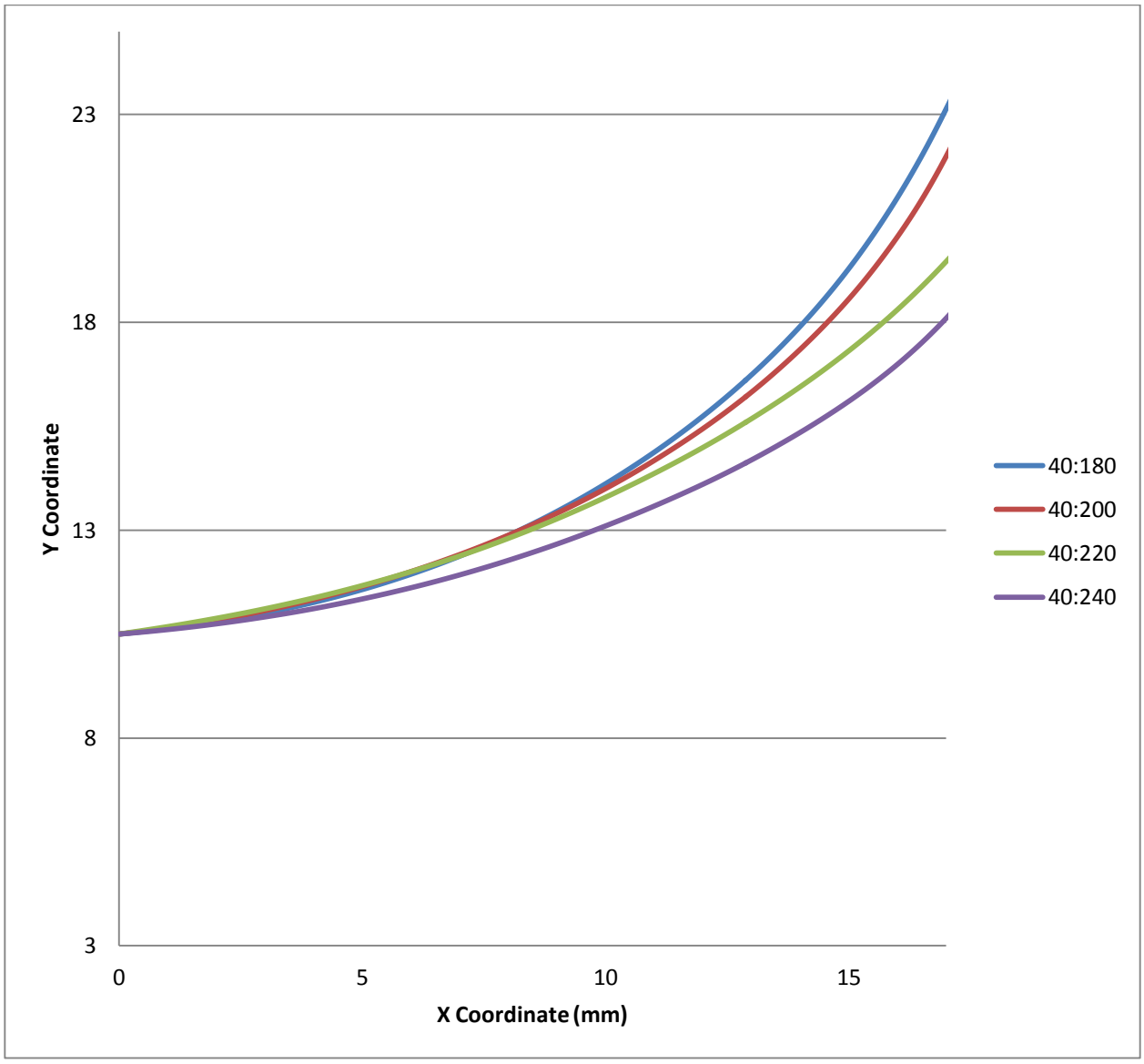

Figure 5.10 Comparison of center jet streamlines to the midplane of the burner.

Turbulent Kinetic Energy Fields

The turbulent fluctuations in each instantaneous velocity field were calculated (*Equation 5.2*) for each interrogation window. These were used to compute the turbulent kinetic energy (*Equation 5.3*) field for each of the cases. The average of the k fields over 2400 images are shown in (*Figures 5.11-14*).

In the review of experimental logs, it was found that the sealant holding the honeycomb flow straightener in the side jet was burned off in the case 40:200. This allowed the honeycomb to float in

the inlet, and made it less effective at providing a uniform flow. This accounts for the increased turbulent kinetic energy observed at the jet exit. In order to perform simulations at this flow velocity, the turbulent kinetic energy was interpolated from the surrounding data points, using the average of the cases 40:180 and 40:220. The suggested boundary conditions are tabulated (*Table 5.2*). In the highest velocity case, streaking in the wake of the mesh is observed. This streaking is due to the turbulent production inside the mesh that takes place at this high velocity condition. This case is unique in that other cases run at lower velocities do not exhibit this behavior. In order for this turbulence to mix out and become isotropic, it is expected that the flow must travel approximately 4 mm downstream.

Another point of interest is the value of turbulent kinetic energy in the flame edge region. It is clear that as the inlet velocity is increased, the turbulent kinetic energy in the region of the flame front increases from a value of approximately 1.5 in the 40:180 case to a value near 5 in the 40:240 case. This is of interest in the statistical analysis of the flame edge. Since this region of the flow is not particularly well seeded, further study to validate these results is needed. More detailed analysis of this trend is performed later in this thesis.

$$u_i' = u_i - \bar{u}$$

Equation 5.2 Calculation of turbulent fluctuations.

$$k = \frac{1}{2}\left(\overline{(u')^2} + \overline{(v')^2}\right)$$

Equation 5.3 Calculation of turbulent kinetic energy

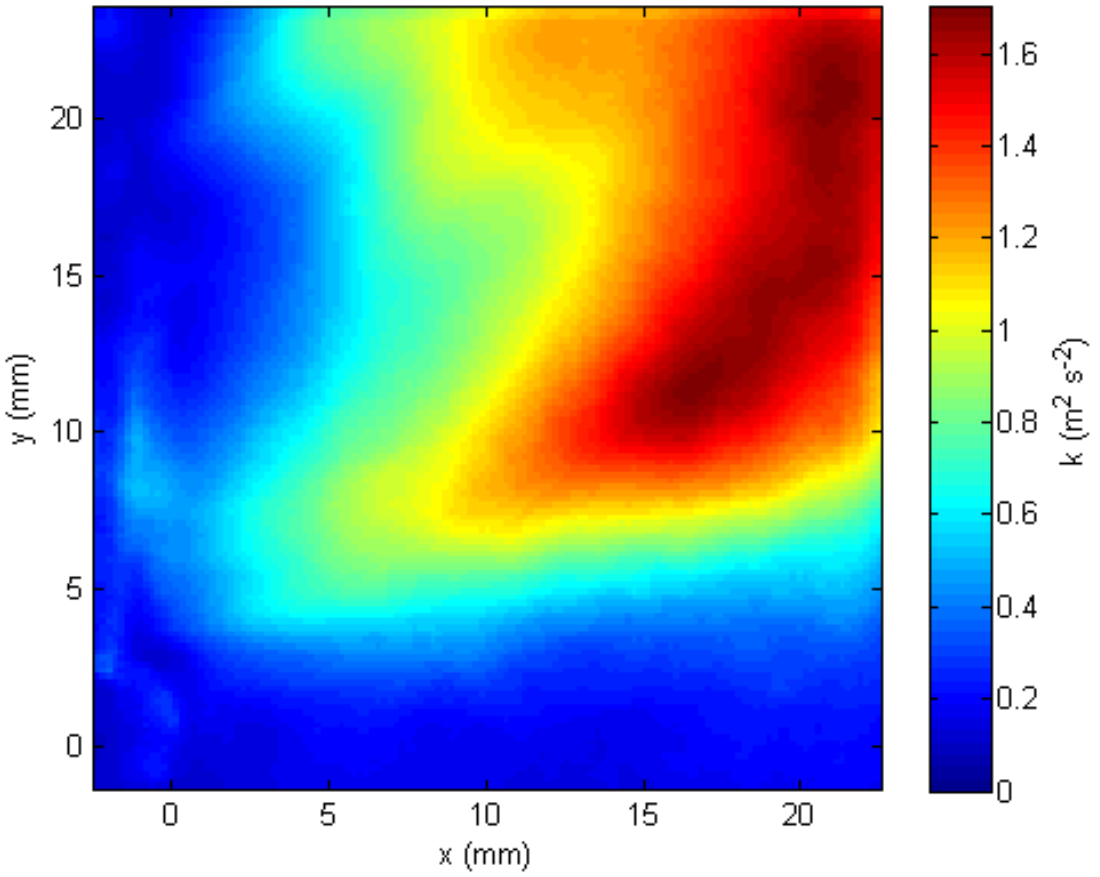

Figure 5.11 Turbulent Kinetic energy field for the case 40:180

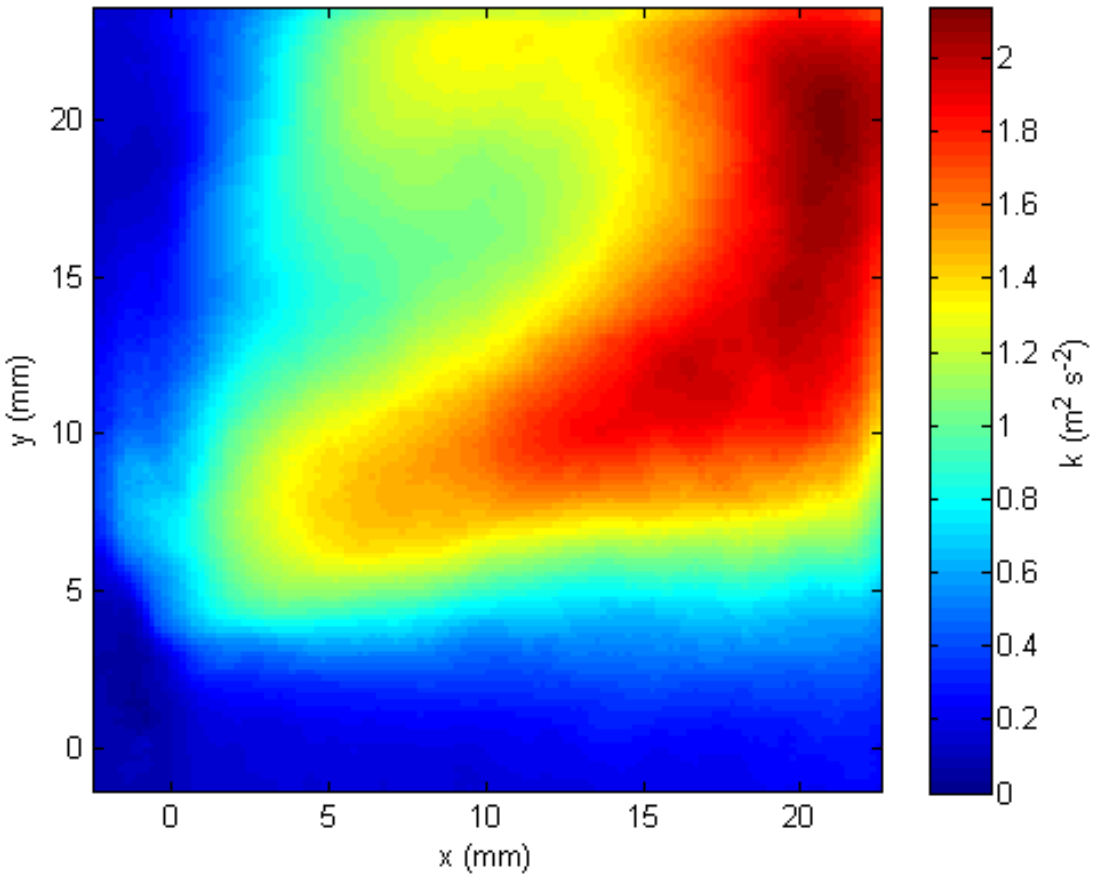

Figure 5.12 Turbulent kinetic energy field for the case 40:200

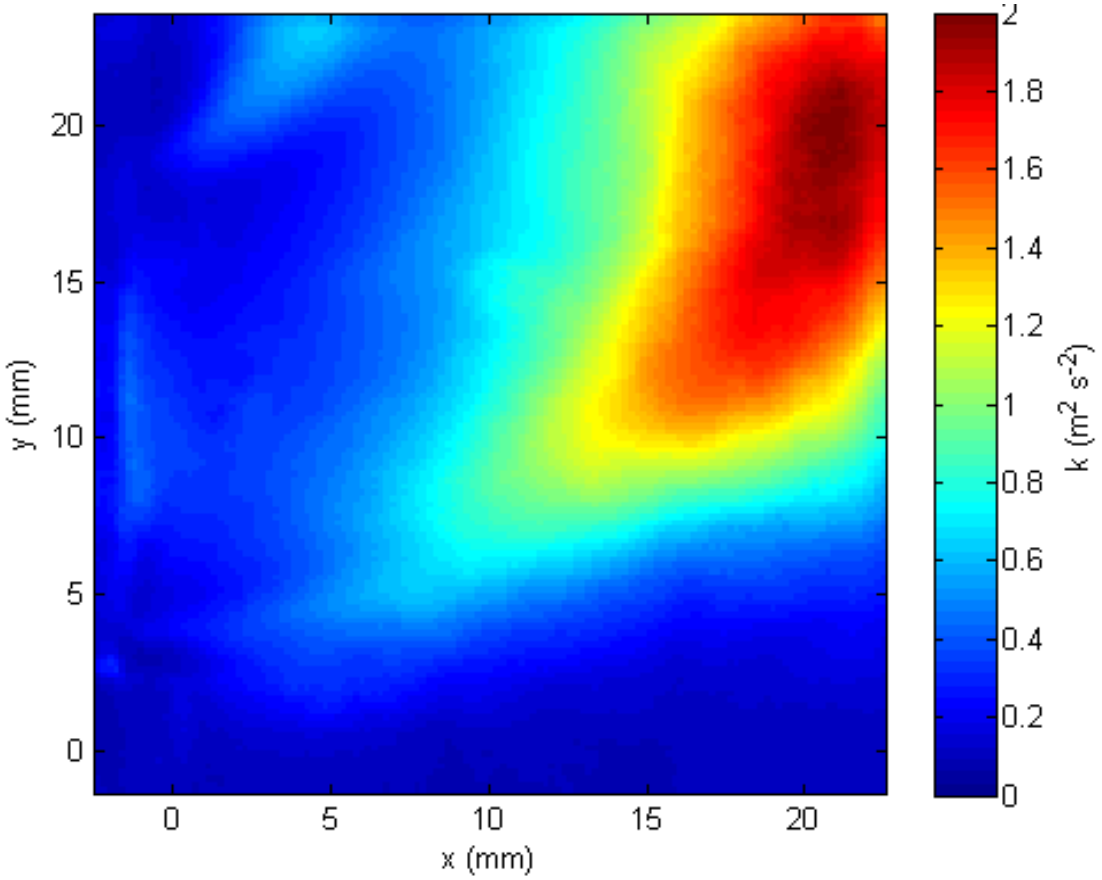

Figure 5.13 Turbulent kinetic field for the case 40:220

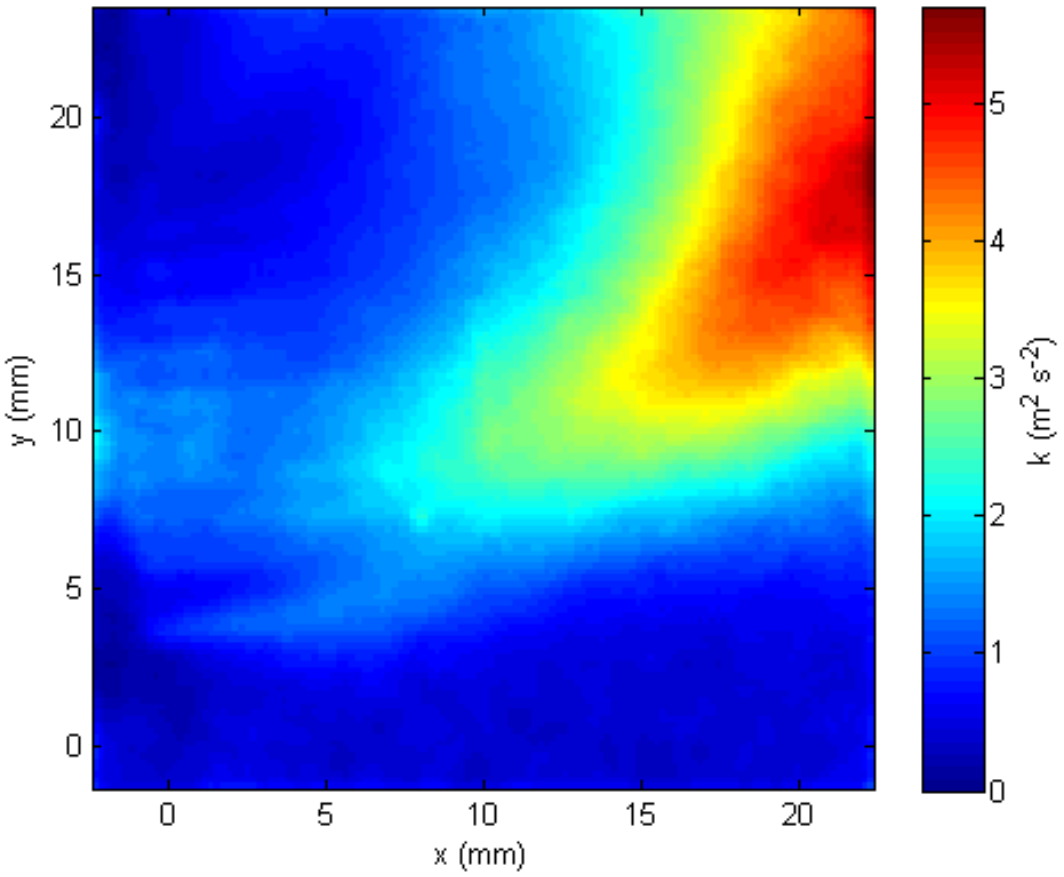

Figure 5.14 Turbulent kinetic energy for the case 40:240

Table 5.2 Turbulent kinetic boundary condition measurements and suggested boundary conditions

Case	Average Turbulent Kinetic Energy (m^2/s^2)	Suggested K Boundary Condition
40:180	0.30	0.30
40:200	0.59	0.30
40:220	0.30	0.30
40:240	0.94	0.94

Integral Length Scales

The integral length scale at the inlet boundary of the side jets is an important measurement for the accurate simulation of this experiment. Moreover, the length scale is of interest directly for understanding how changes in the length scale of the turbulence field affects local extinction at the flame edge. The integral length scale of interest in this experiment is the longitudinal integral length scale (*Equation 5.4*). This length scale is representative of the largest scale in the energy spectrum.

These are measured in the direction of bulk flow velocity. In this experiment, the integral length scale is calculated using a discretized form of a two point velocity correlation function. The two-point correlation function was calculated starting at each of the PIV interrogation windows at the jet exit (52 per image, 2400 images). These 124,800 two point velocity correlation functions were averaged (*Figure 5.15*) and numerically integrated to the first zero crossing, as used in the study by O'Neill *et al*. (Nicolaides, Honnery, and Soria 2004). These values were compared to the analytic integration from a least squares regression fit of an exponential function to the data points (*Table 5.3*). The grid positioned just before the side jet exits had a hexagonal cell size of approximately 2 mm. Since there is no monotonic trend in integral length scale in terms of velocity, it would be appropriate to use an integral length scale that is the arithmetic mean of the cases in which the mesh was firmly attached. The lack of a trend in the length scale in conjunction with the fact that the hexagonal grid is positioned less than 1 mm away from the jet inlet lead to the conclusion that the turbulent length scale is governed by the mesh in the side jet channel. It is suggested to use an integral length scale of 5.2 mm for all cases in the simulations.

$$L_{11} = \int_0^\infty R(r)dr \ \ and \ R(r) = \frac{u'(x)u'(x+r)}{(u'(x))^2}$$

Equation 5.4 Integral length scale calculation

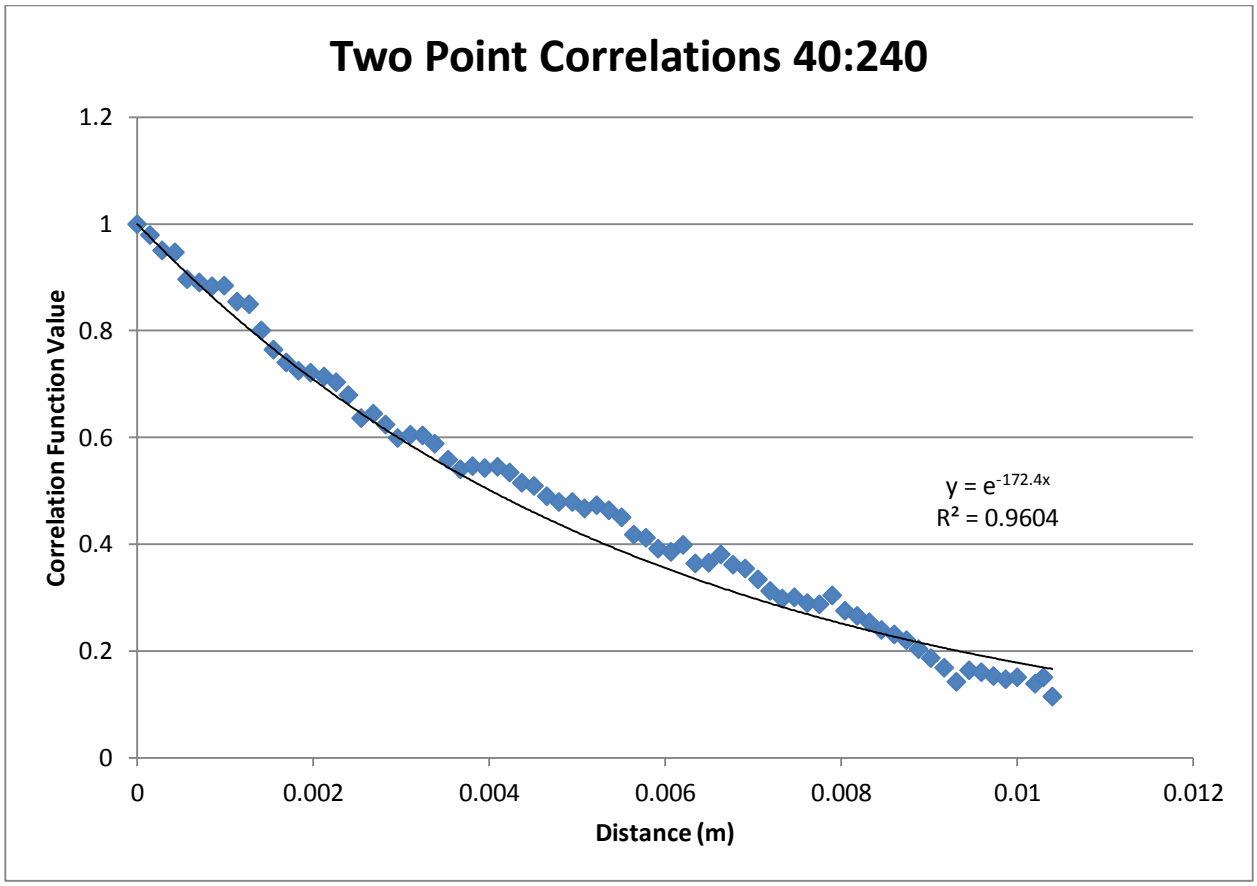

Figure 5.15 Averaged two point velocity correlation functions for the case 40:240 with exponential fit shown

Table 5.3 Calculated integral length scales

Case	Integral Length Scale (Numerical Integration)	Integral Length Scale (Exponential Fit)
40:180	5.0 mm	5.5 mm
40:200	5.4 mm	6.4 mm
40:220	4.3 mm	4.1 mm
40:240	5.0 mm	5.8 mm

Other Scalar Fields of Interest

In the study of fluid flows, instantaneous (*Figure 5.11*) and average (*Figures 5.12 -5.15*) vorticity fields are of interest. Vorticity is defined as the curl of the velocity field, and was calculated for each individual vector field. The average vorticity field was calculated as the average of all of the instantaneous velocity fields. (*Equation 5.4*) Vorticity is important to evaluate mixing. Instantaneous vorticity plots can also be

used to gather information on the length scales present in the flow. In the average plots, the vorticity of the jet at the leading edge is negative. The vorticity at the jet core is near zero, and the vorticity of the trailing edge of the jet is positive. This is because the fluid elements at the leading edge of the jet are expected to experience a rotational movement in the clockwise direction due to the strong shear layer present in this location. The same explanation holds for the trailing side, but the rotation is expected to be counter clockwise.

For increasing side jet velocity, it was found that the vorticity in the shear layer of the jet increased. This was observed in all cases except the 40:200 case, in which the honeycomb mesh was loose in the inlet channel. This case exhibited less vorticity in the shear layer, but higher vorticity penetrating into the jet core. Of particular interest is the high vorticity seen at the mesh inlet on the highest velocity case. These structures are the same size as the flow straightening grid. This points to turbulent production in this region, which was discussed earlier in this chapter.

$$\omega = \nabla \times \vec{v} = \frac{\partial v_y}{\partial x} - \frac{\partial v_x}{\partial y}$$

Equation 5.4 Calculation of vorticity for a two dimensional flow with no out of plane motion

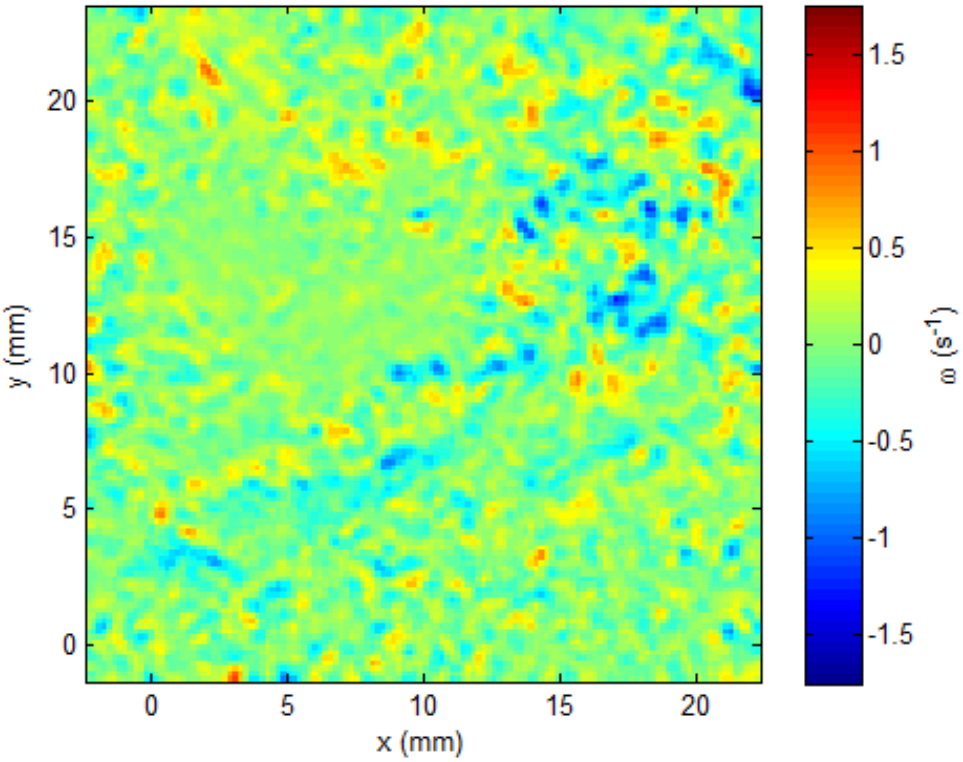

Figure 5.11 Sample instantaneous vorticity field taken from 40:240 data

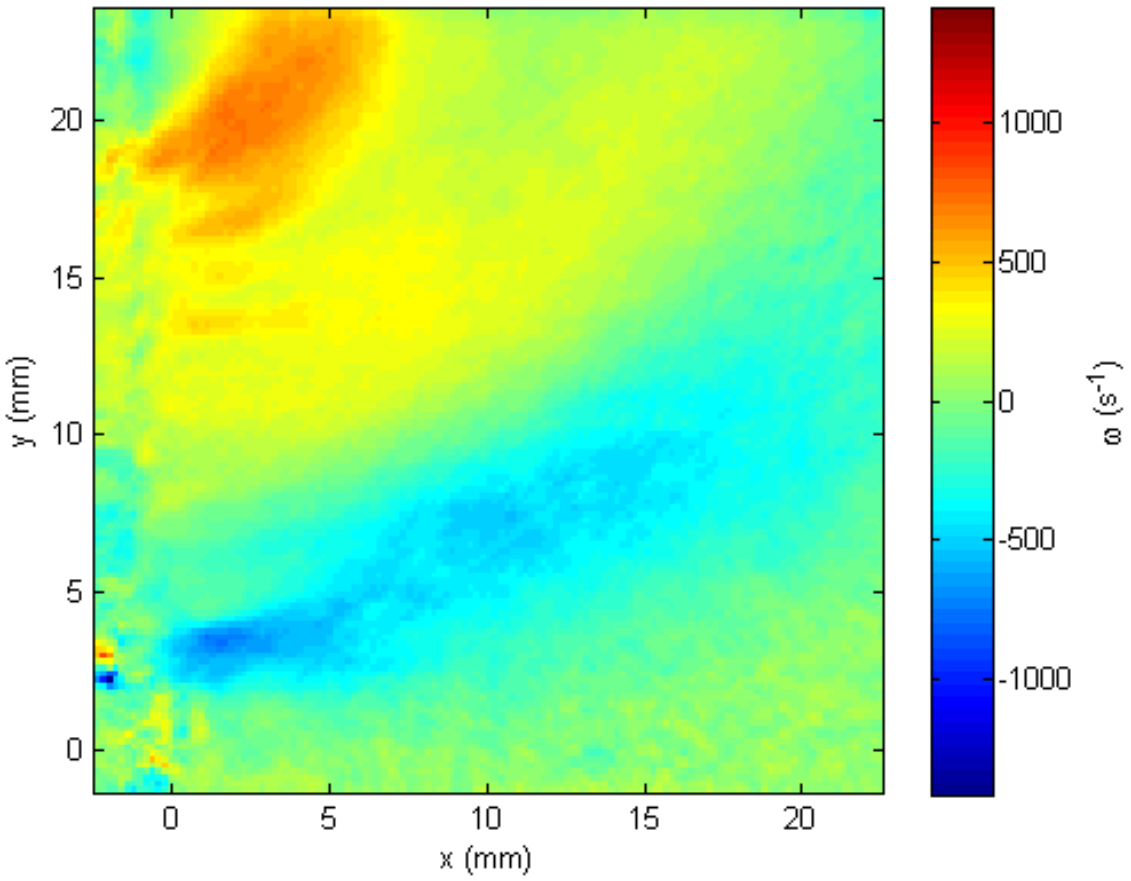

Figure 5.12 Average vorticity field from the case 40:180

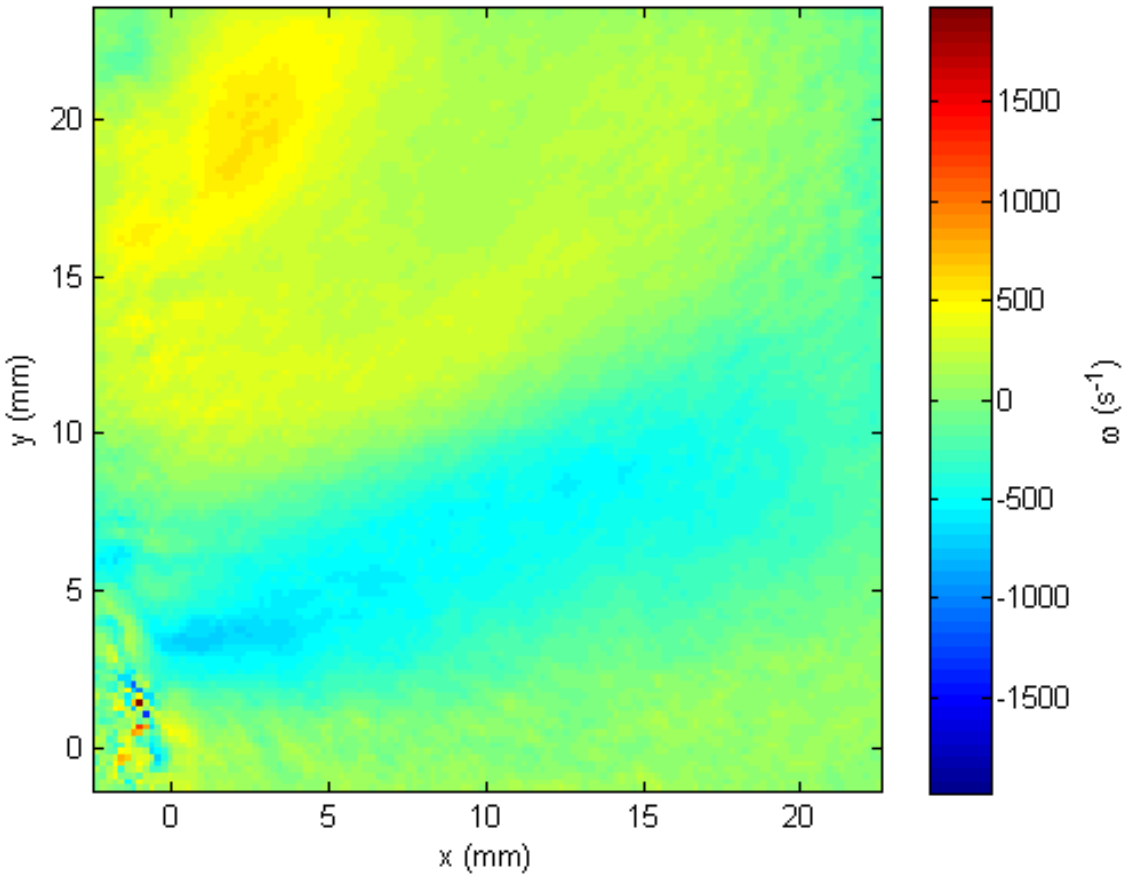

Figure 5.13 Average vorticity field for the case 40:200

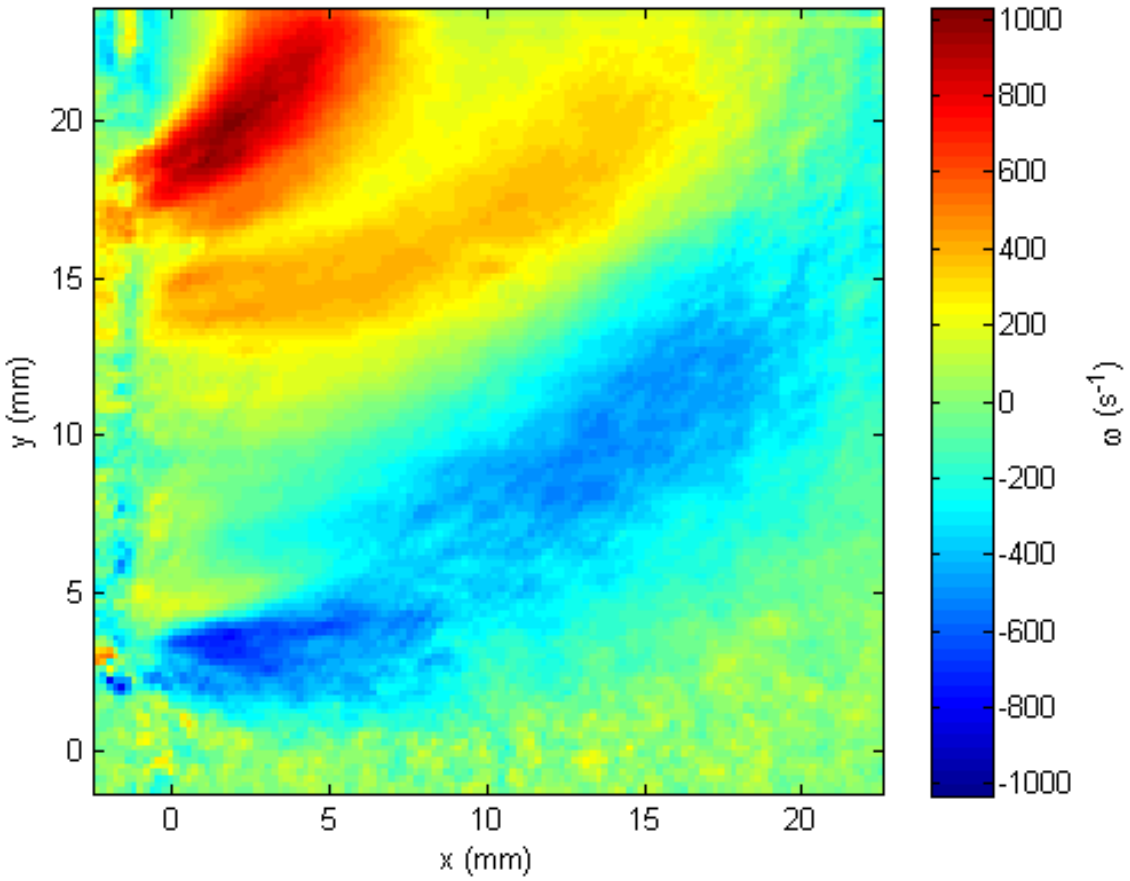

Figure 5.14 Average vorticity field for the case 40:220

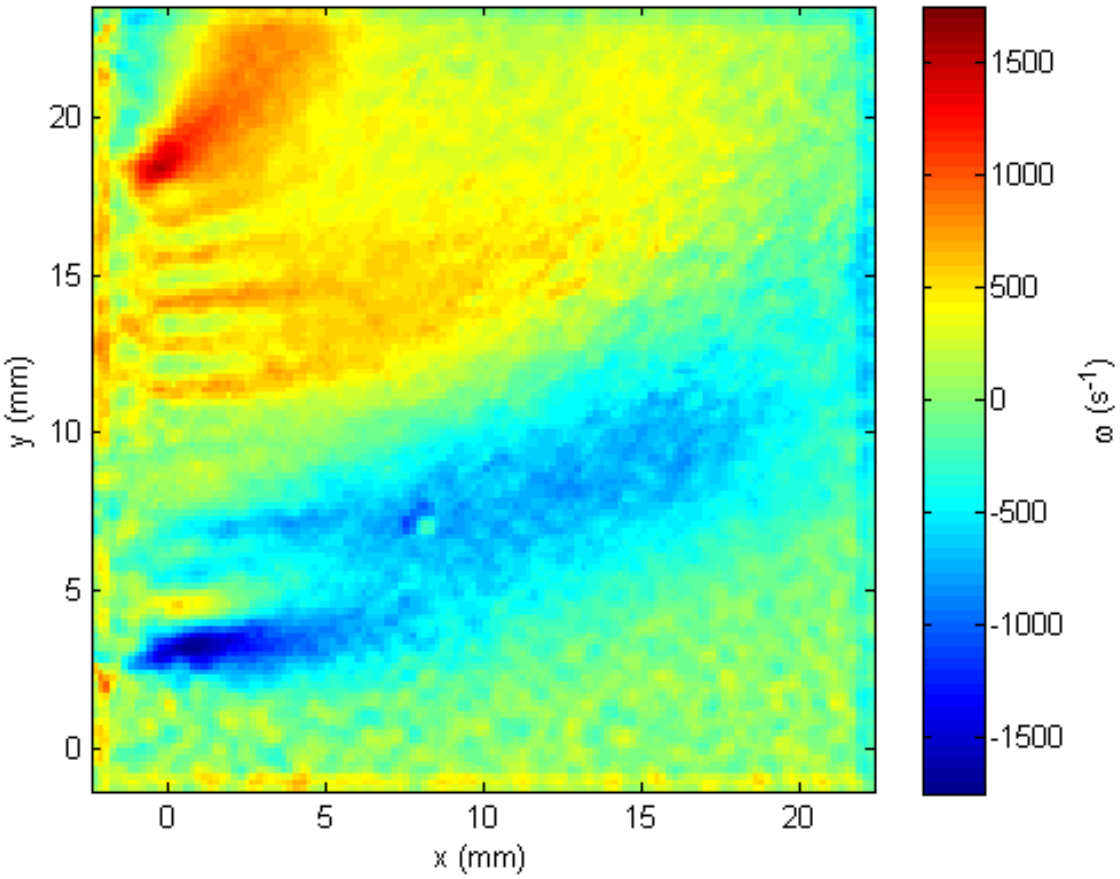

Figure 5.15 Average vorticity for the case 40:240

Summary

From this section appropriate boundary conditions for CFD simulations of the burner presented in this thesis are presented. The appropriate velocity inlet profiles can be found in (*Table 5.1*). The turbulent kinetic energy for each case can be found in (*Table 5.2*). The integral length scales can be found in (*Table 5.3*). It is suggested to use an integral length scale of 5mm for all of the computational cases to be run.

Chapter 6: Full Flow Field Results

The flow field in the entirety of the burner, especially in the region of the flame is of utmost importance in the characterization of the flame edge. PIV measurements that spanned the entire flame region were performed and the results from these measurements are presented in this chapter. The burner center plane is located as x=0 mm. The side jet exits are positioned between y=15 and y=30 for all experimental cases. This corresponds to the end of the splitter plate being y=0. All of the experimental cases were composed from 2000 instantaneous velocity fields.

Average Flow Field

In this study, the upstream flow in the burner was seeded to quantitatively capture the upstream inlet conditions and velocity in the vicinity of the flame edge. The side jets were lightly seeded to avoid fogging of the window in the flame edge location. This study is not expected to accurately capture the side jet inlet velocity profile. This is detailed earlier in chapter 5. The flame edge is expected to exist within 5 mm of the burner center plane between y coordinates y=15 to y=30 mm. In all of the average velocity fields a region of higher velocity than the upstream inlet is observed in the location of the laminar diffusion flame. (*Figures 5.1*-4).This is due to the decrease in density due to the temperature increase in the flame. The surrounding flow is of uniform velocity within 10% of the nominal inlet velocity. (*Figure 6.5*) As observed in the previous chapter, higher jet velocities lead to less jet deflection, moving the high velocity region of the flow closer to the splitter plate (*Figure 6.6*). The centerline maximum velocity in the vicinity of the edge and downstream of it does not change appreciably across the range of experimental conditions tested, but the region of high velocity extends farther in the span wise direction for higher inlet velocity cases (*Figure 6.7*). Since the location of the flame edge is not exactly known in each frame, a quantitative edge speed cannot be calculated from this average data. This edge speed is calculated in the next chapter of this thesis.

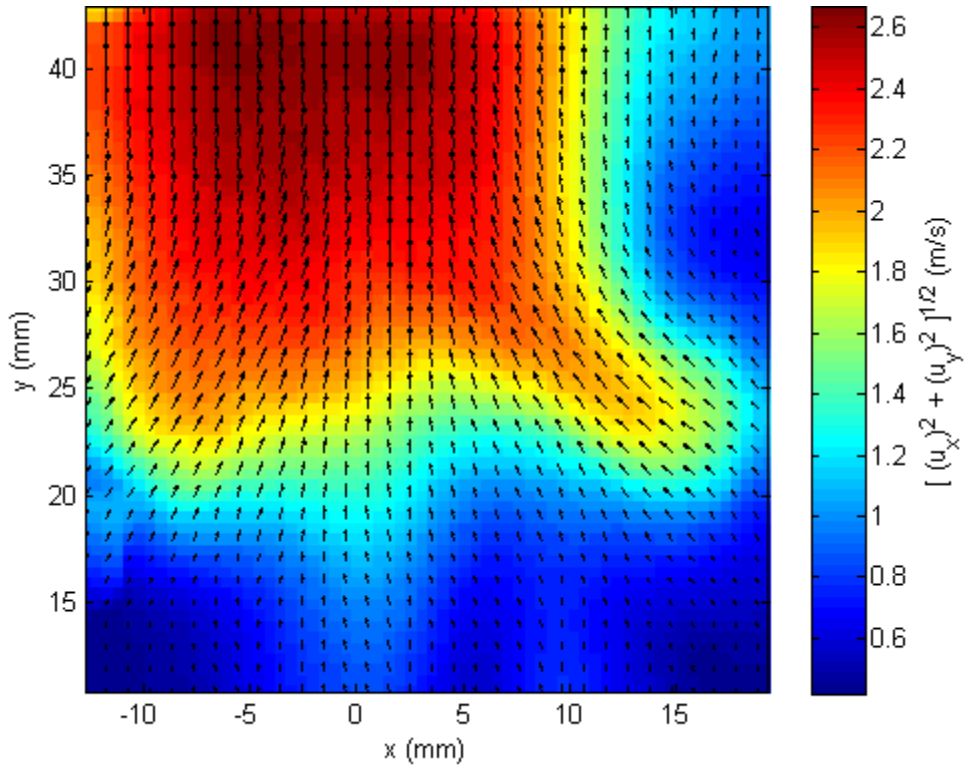

Figure 6.1 Average velocity field for the reacting case with upstream velocity of 40 cm/s and downstream jet velocity of 180 cm/s The average flame edge position from chemiluminescence measurements is x=1mm, y=22.7mm

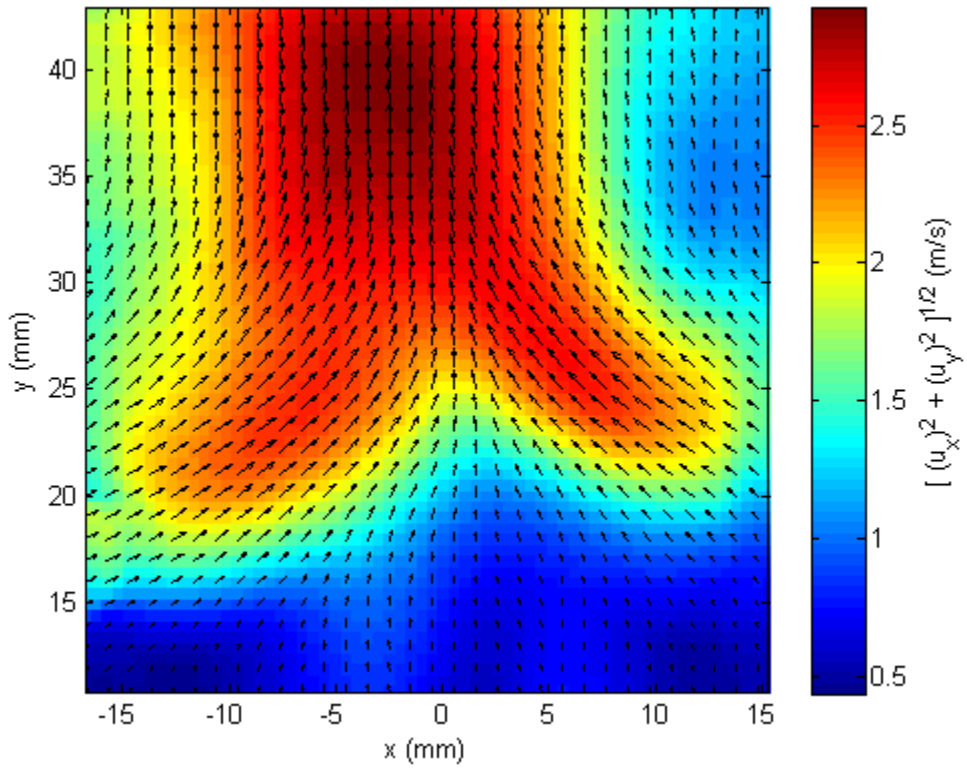

Figure 6.2 Average velocity field for the reacting case with upstream velocity of 40 cm/sec and downstream jet velocity of 200 cm/s. The average flame edge location is x=0.2mm, y=22.6mm from chemiluminescence measurements

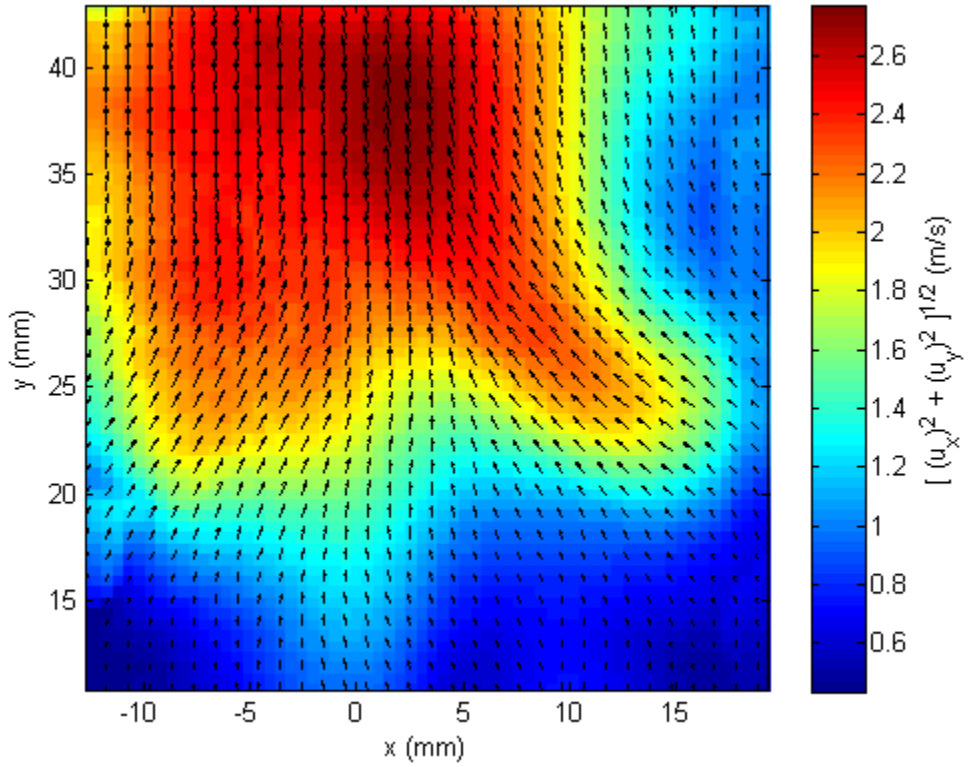

Figure 6.3 Average velocity field for the reacting case with upstream velocity of 40 cm/sec and downstream jet velocity 220 cm/s. The average flame edge position is x=-2mm, y=21.3mm from chemiluminescence measurements

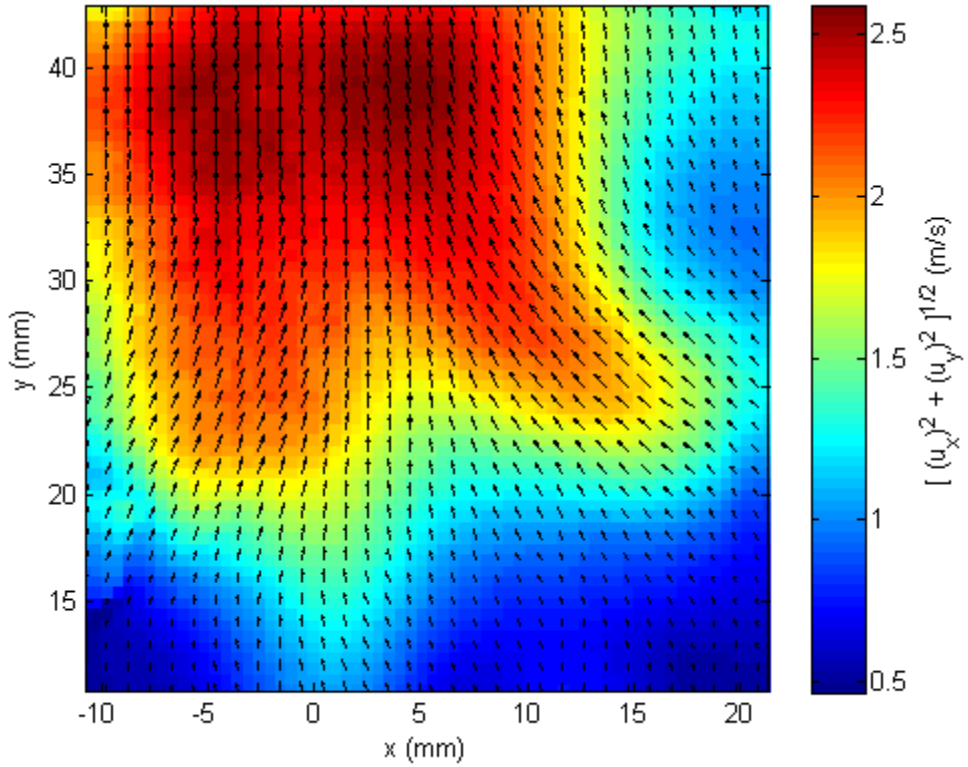

Figure 6.4 Average velocity field for the reacting case with upstream velocity 40 cm/s and downstream jet velocity of 240 cm/s. The average flame edge location is x=0.6mm, y= 19.6mm from chemiluminescence measurements

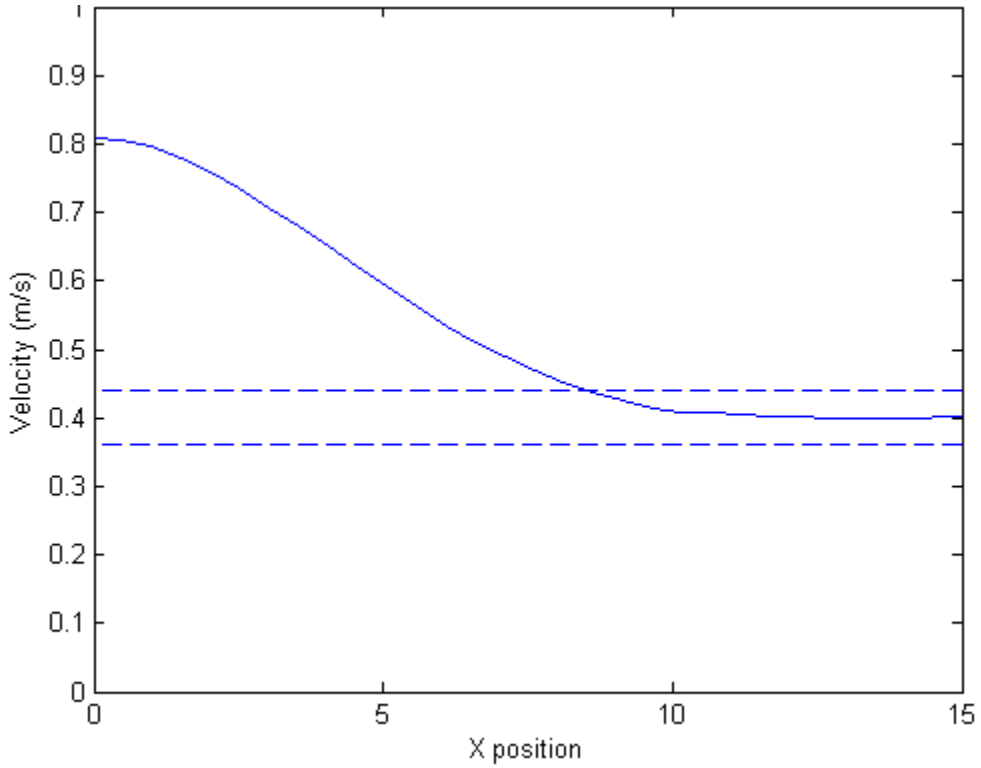

Figure 6.5. Y velocity profile showing uniform flow surrounding accelerated flow due to heating from the chemical reaction. This plot is taken at a y position of 12mm downstream of the splitter plate. The dashed lines represent +- 10% of the nominal value.

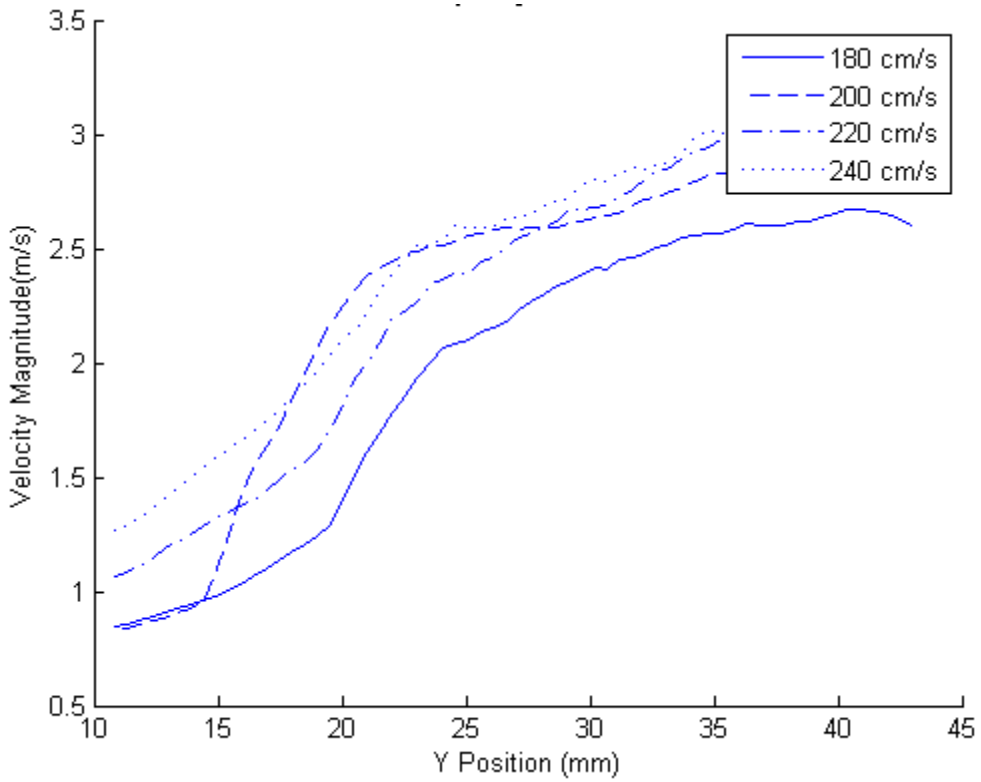

Figure 6.6 Velocity magnitude profile along the center plane of the burner

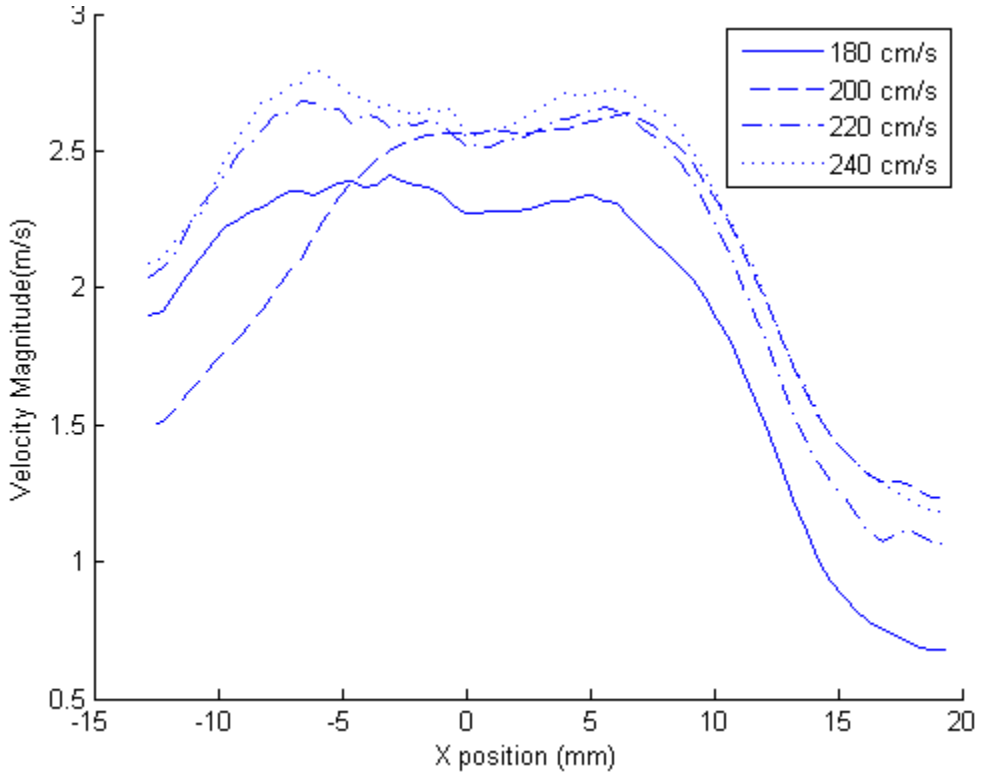

Figure 6.7 Velocity magnitude profiles at y=30mm

Turbulent Kinetic Energy

As with the average velocity field, the inlet turbulent kinetic energy at the jet location is not expected to be quantitatively captured due to low seed density in this region. The side jet velocity statistics were characterized separately in Chapter 5. The turbulent kinetic energy in the upstream flow and the flame edge region is of interest in this study, and is adequately resolved. From the turbulent kinetic energy fields, it is clear that the assumption of nearly zero turbulent kinetic energy upstream of the jets is valid (*Figures 6.8-12*).For increasing inlet velocity the turbulent kinetic energy in the flame region increased. In all cases except for the 40:200 case, the turbulent kinetic energy was dispersed in the flame region in a wide range of x values with a near 20 mm full width half max at y=0. In the 40:200 case, the turbulent kinetic energy is observed in a very narrow band with a full width half max of less than 5mm at y=0 (*Figure 6.13*). This is probably due to the seeding in those experimental cases being lighter in the side jets than any of the other cases. This could cause the velocity in this region to not be calculated for any of the image pairs. It is of note that the maximum turbulent kinetic energy in this case is higher than the 40:220 case.

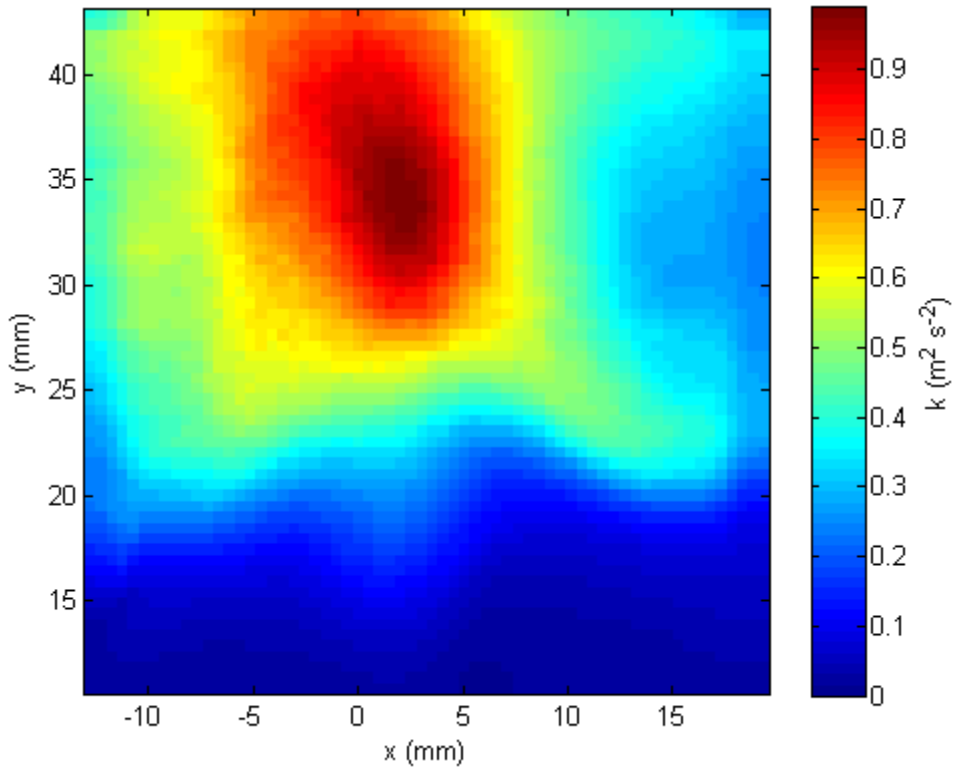

Figure 6.8 Turbulent kinetic energy field for reacting case with upstream velocity of 40 cm/sec and downstream jet veloicty of 180cm/s. The average flame edge position from chemiluminescence measurements is x=1mm, y=22.7mm

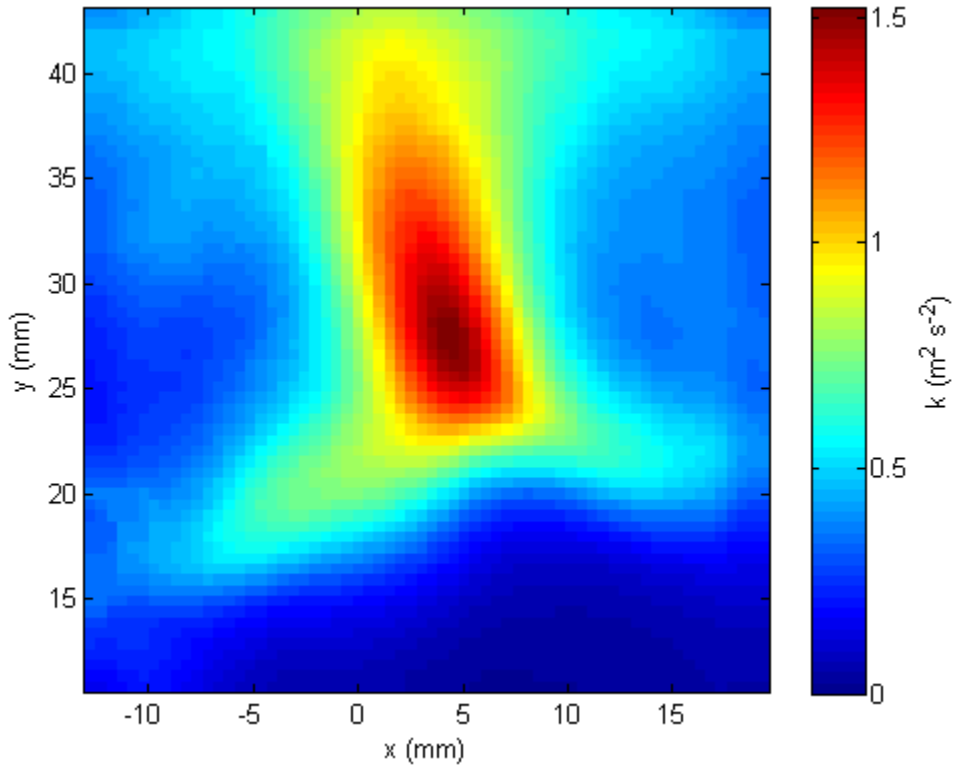

Figure 6.9Turbulent kinetic energy field for the reacting case with upstream velocity of 40 cm/s and downstream jet velocity of 200 cm/s. The average flame edge location is x=0.2mm, y=22.6mm from chemiluminescence measurements

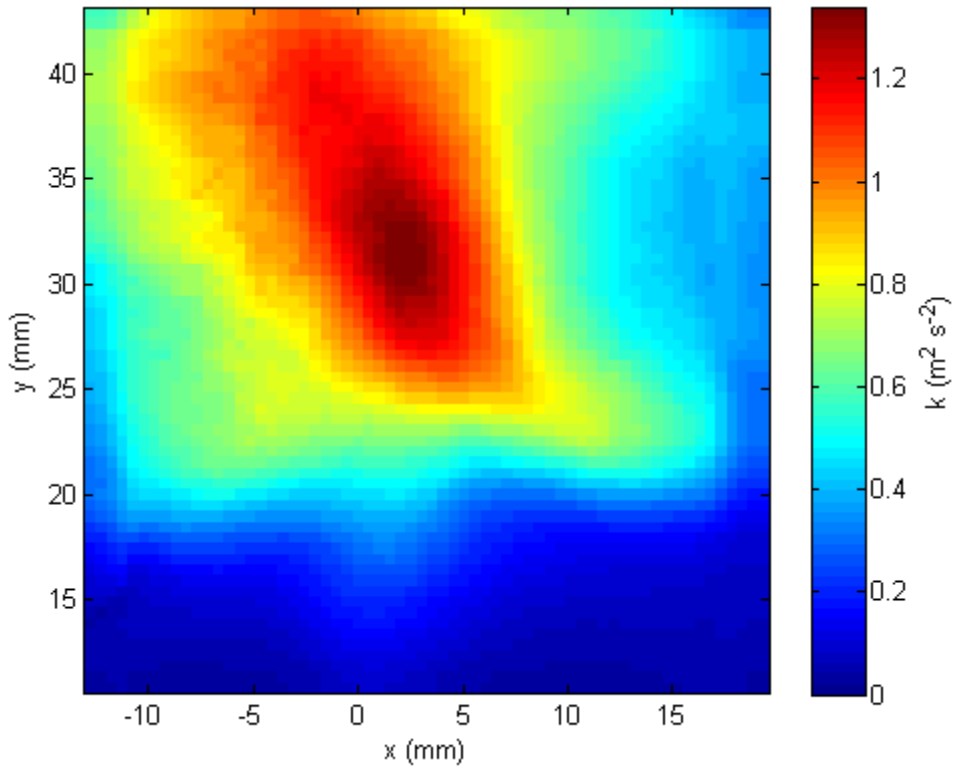

Figure 6.10 Turbulent kinetic energy field for the reacting case with upstream velocity of 40 cm/sec and downstream jet velocity of 220 cm/s. The average flame edge position is x=-2mm, y=21.3mm from chemiluminescence measurements

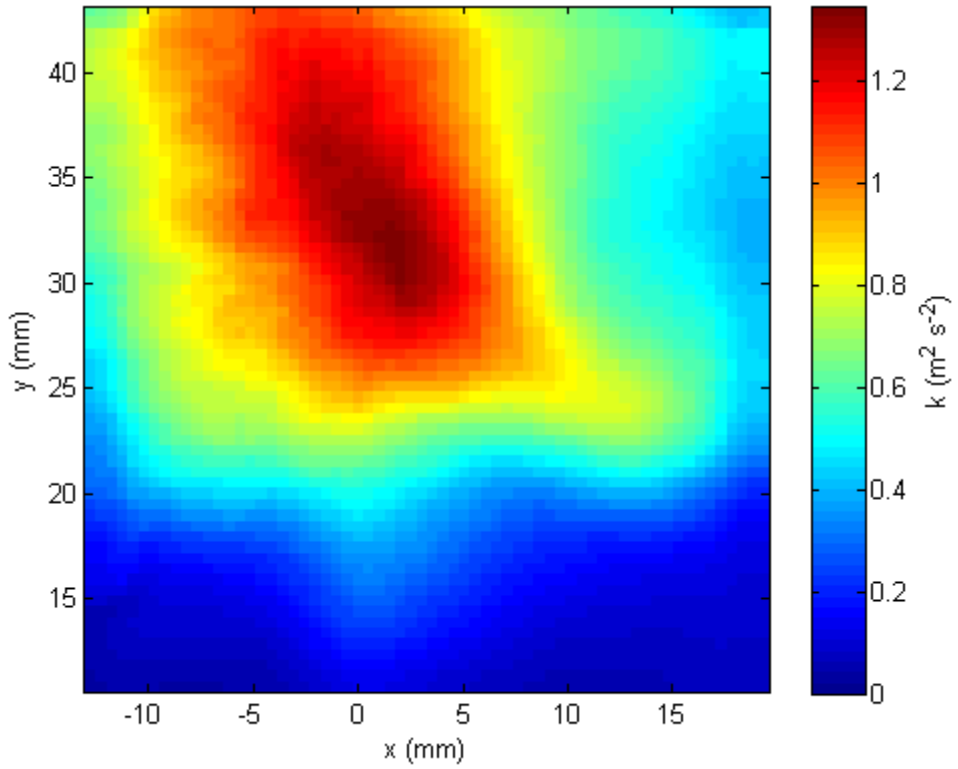

Figure 6.11 Turbulent kinetic energy field for the reacting case with upstream velocity of 40 cm/s and downstream jet velocity of 240 cm/s. The average flame edge location is x=0.6mm, y= 19.6mm from chemiluminescence measurements

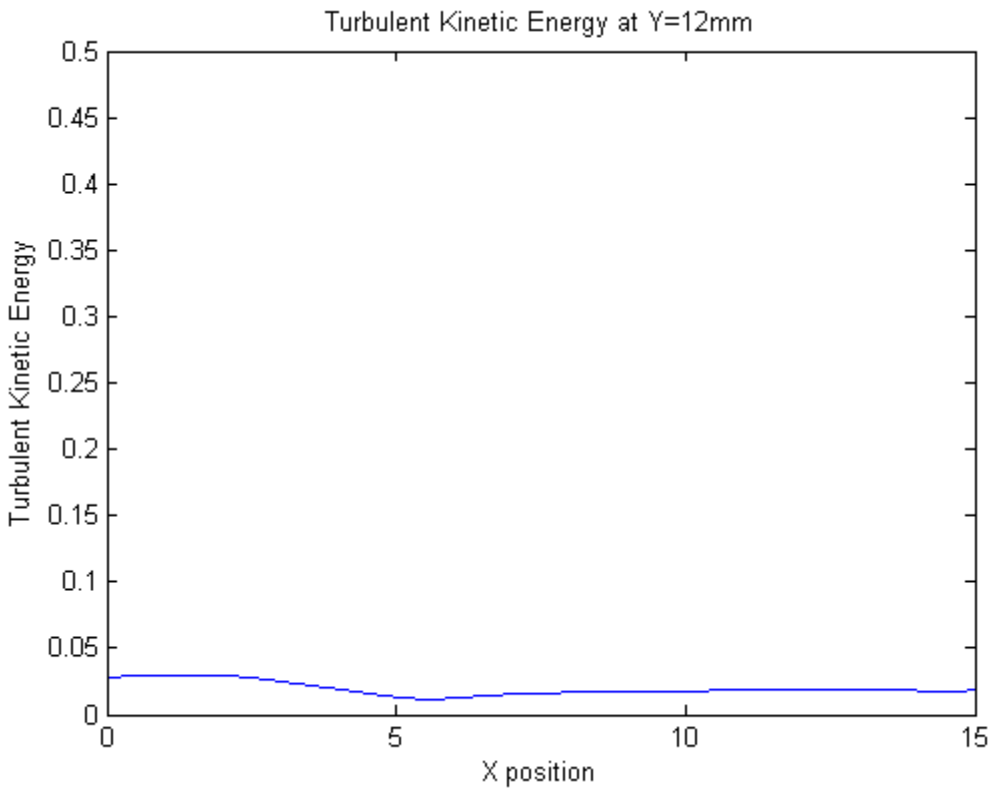

Figure 6.12 Profile plot of turbulent kinetic energy 12mm downstream from the upstream inlet

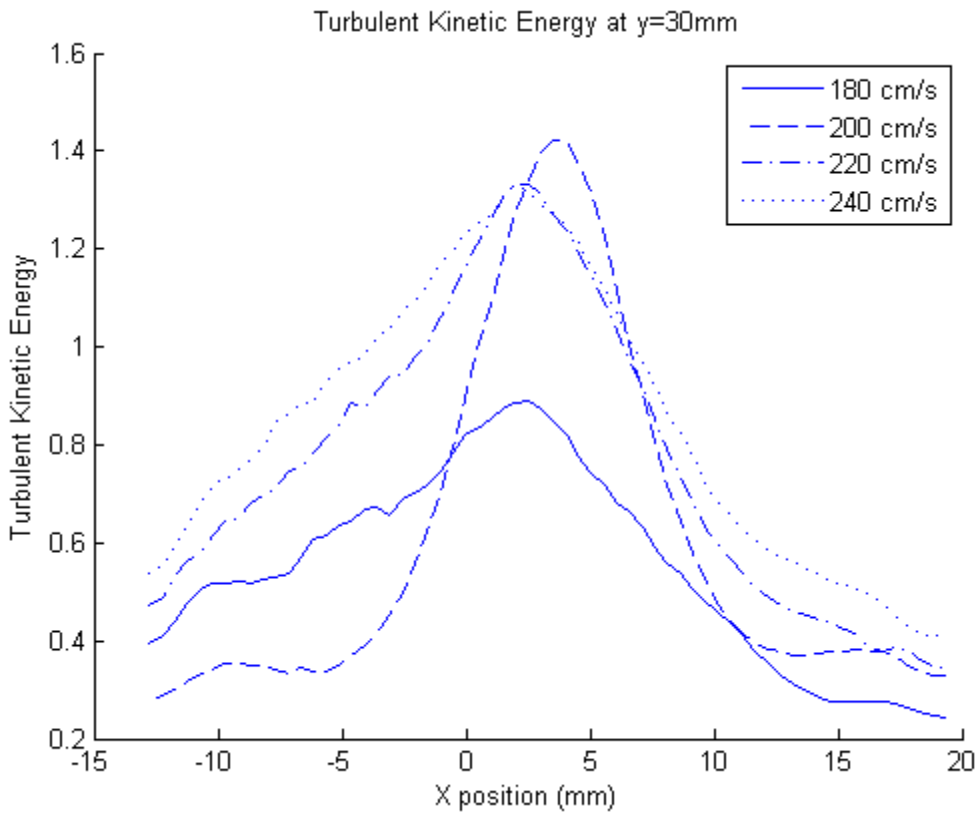

Figure 6.13 Turbulent kinetic energy profile plots at y=30mm

Average Vorticity

Because the side jets were not seeded adequately to resolve the velocity field in them for all of the cases in this study, it is not expected to observe quantitative agreement between this data and the data presented in the previous chapter in the region of the jet inlet. What is apparent from the average vorticity plots (*Figures6.14-17*) is that the flame initially exists in a low vorticity region before the effects of the side jets are observed farther downstream. It is interesting to note that the left side jet is deflected less than the right side jet in all of the cases. This is due to the momentum difference between the fuel and air streams. There does not appear to be a significant difference in average vorticity in the region of the flame edge across the experimental cases studied.

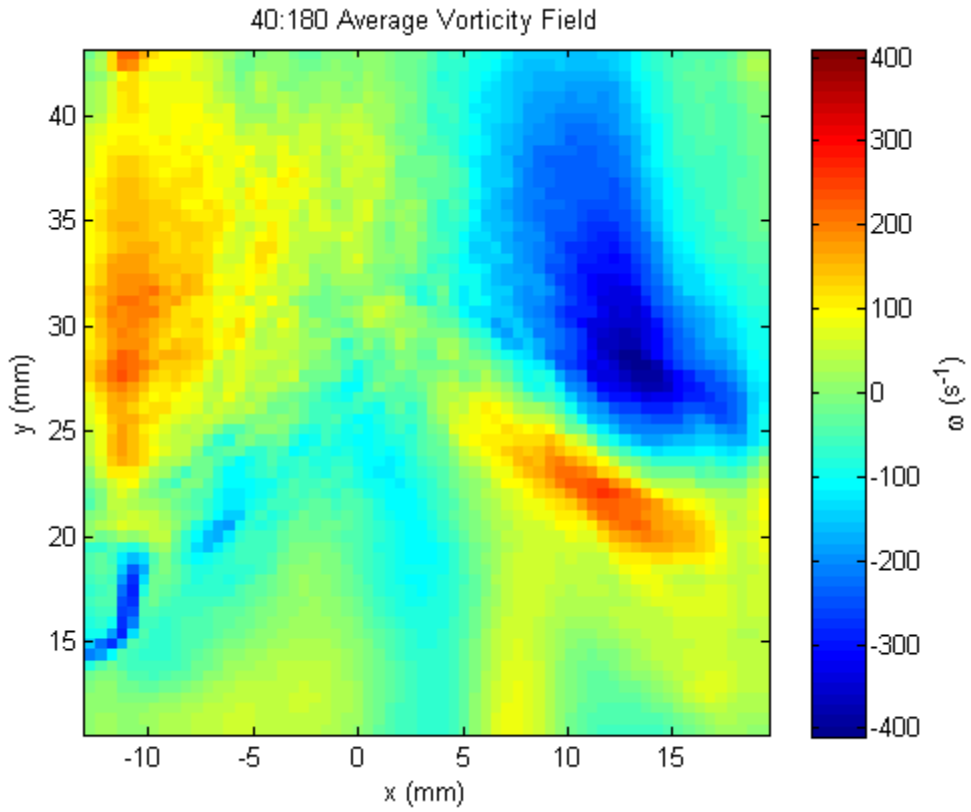

Figure 6.14 Average vorticity field for the reacting case with upstream velocity of 40 cm/s and downstream jet velocity of 180 cm/s. The average flame edge position from chemiluminescence measurements is x=1mm, y=22.7mm

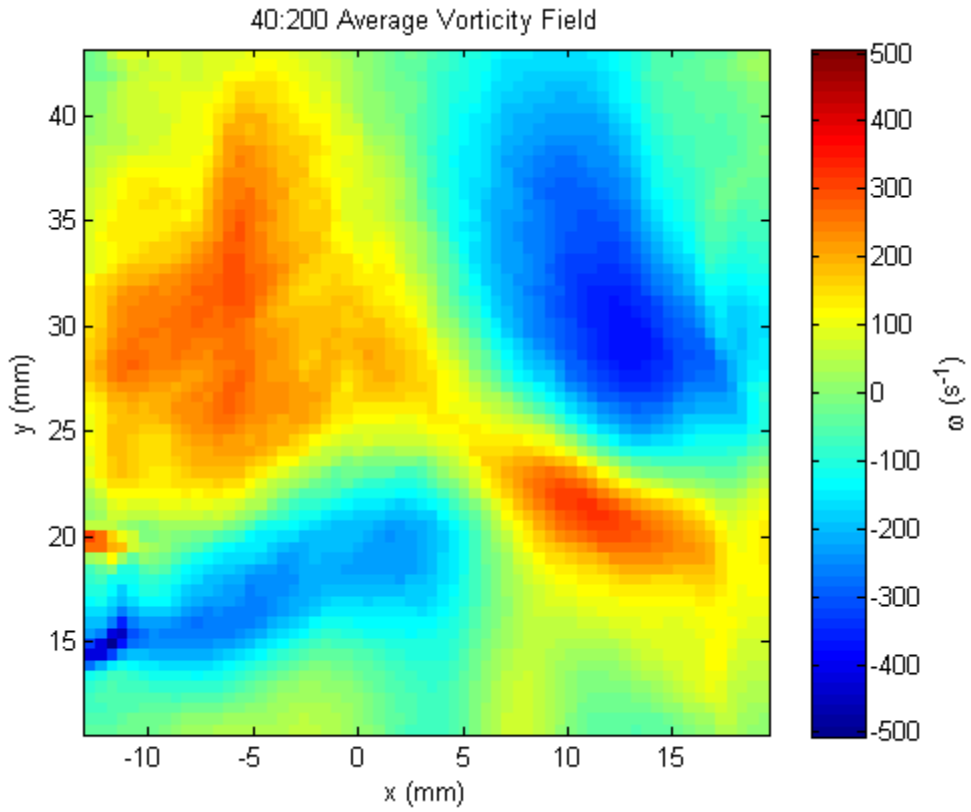

Figure 6.15 Average vorticity field for the reacting case with upstream velocity 40 cm/s and downstream jet velocity of 200 cm/s. The average flame edge location is x=0.2mm, y=22.6mm from chemiluminescence measurements

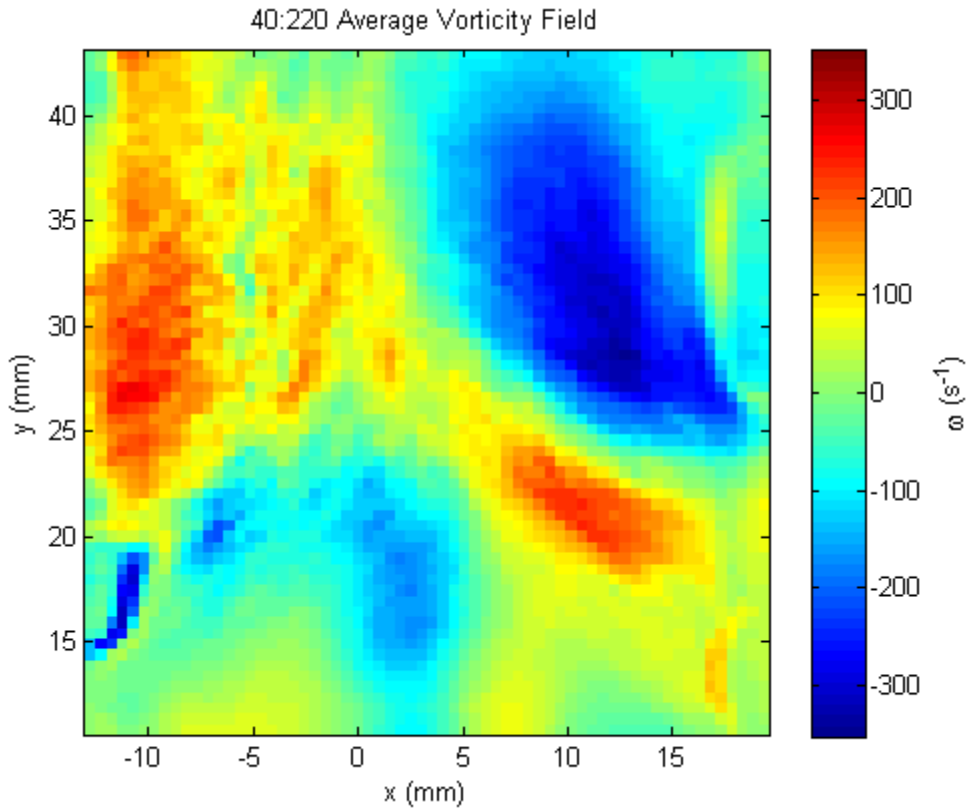

Figure 6.16 Average vorticity field for the reacting case with upstream velocity 40 cm/s and downstream jet velocity 220 cm/s. The average flame edge position is x=-2mm, y=21.3mm from chemiluminescence measurements

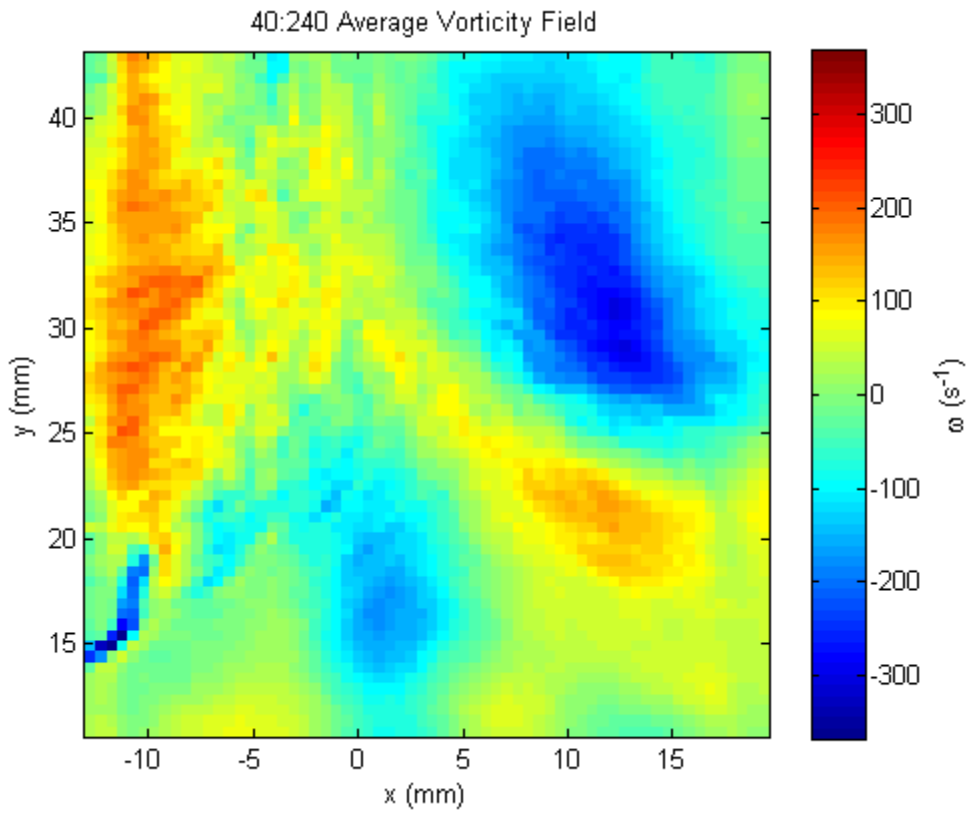

Figure 6.17 Average vorticity field for the reacting case with upstream velocity of 40 cm/s and downstream jet velocity of 240 cm/s. The average flame edge location is x=0.6mm, y= 19.6mm from chemiluminescence measurements

Summary

In this chapter the velocity field in the region of the flame upstream of the extinction event and the region of the flame edge is studied. The upstream inlet conditions of uniform flow at the nominal flow velocity with no turbulent kinetic energy are observed to be valid. The average velocity and turbulent kinetic energy in the region of the flame edge is presented, and average vorticity fields are examined. These statistics will be investigated in more detail in the next chapter. Since there was no technique used to determine the exact edge location, a negative edge cannot be reported. Attempts to calculate the negative edge speed are detailed in the next chapter of this thesis. The previous chapter details the boundary conditions for the jets and the flow field in that region.

Chapter 7: Flame Edge Extraction and Edge Velocity Statistics

PIV measurements of the same burner conditions as studied in the previous chapter were also performed without a laser line filter in front of the CCD camera. This allowed the chemiluminescence from the flame to be captured by the camera during the second PIV frame. A novel filtering technique is presented to provide an estimate of the flame edge location from the second image in the PIV Mie scattering image pair. The coordinate system is the same as the previous analysis, with the center plane of the burner being x=0 mm and the end of the splitter plate being y=0. The data sets consist of 1000 image pairs for each of the experimental conditions.

Extraction of Flame Edge Location in PIV Image Pairs

In these measurements, the upstream flows were seeded to capture the velocity in the flame region. The side jet flows were also seeded to provide velocity vectors in the side jets, but the density was considerably lower than the upstream flow, as any seed build up on the windows of the burner renders the line of sight chemiluminescence integration used in this technique ineffective.

The second Mie scattering image of a PIV image pair has a considerably longer exposure time than the first image. The exposure time in the first image is limited by the inter-frame delay at 75 microseconds. The second frame exposure time is 200 microseconds. If chemiluminescence is present in the region of interest and no optical means are used to filter it out, this is recorded on the CCD chip. The intensity of this signal relative to the seed particle signal can vary greatly and is affected by factors such as laser power, seed density, chemiluminescence intensity, and detector sensitivity to different wavelengths of light. In this study, the intensity of the flame is significantly lower than the seed particles and relatively close to the background (*Figure 7.1*). Traditional edge finding routines or thresholding proved to be ineffective to extract the flame edge due to the dominant signal levels from Mie scattering.

If a histogram of the pixel intensities in the image is computed, a roughly Gaussian distribution of nearly background level values is observed. There is also a small peak of values very near the maximum

pixel values found in the image (*Figure 7.2*). In these sets of images, this small peak with large intensity represents the Mie scattering from the seed particles. The Gaussian distribution of smaller pixel intensities represents both chemiluminescence and background noise. It is desirable to reduce the value of the pixels representing Mie scattering in the region that is not the flame to below the value of the chemiluminescence so that the flame shape can be extracted using a threshold. In this thesis, these pixels from Mie scattering were first forced to 0. The threshold for zeroing out the pixels was obtained by finding the peak location in the 25 bin histogram of normalized pixel intensities (~450 counts in Fig. 7.2), then finding the first bin less than this intensity in which the value is less than 0.5% of the peak value. All pixels with a larger intensity than this threshold were set to 0. This removed the strongest signal from the Mie scattering of the laser, but did not remove the signal from the chemiluminescence (*Figure 7.3*). Note in Fig. 3, that the Mie scattering field is now represented by black pixels.

The resulting image was still too noisy to extract the flame edge from with routine edge finding algorithms. The Mie scattering from PIV particles extend to neighboring pixels (to enable sub-pixel spatial resolution) thus zeroing only the brightest pixels leaves some medium level signals that are still larger than chemiluminescence. A non-linear diffusion filter was next used to remove the remaining signal from the seed and proved enough contrast between the background and the flame to extract a flame profile. The non-linear diffusion filter is described in Appendix 1. After the filter was applied (*Figure 7.4, left*), a thresholding method was used to extract the approximate flame profile (*Figure 7.4, right*). In this study, values one standard deviation higher than the mean after applying the non-linear diffusion filter were considered to be the flame and set to 1 in the binarized image of Fig. 7.4. Everything else was considered not to be from the flame and was set to zero. The flame edge position was defined to be the center of the flame pixels (unity value) in the row farthest downstream from the splitter plate.

The flame edge locations found using this method correspond to positions between 18.2 mm and 24.5 downstream of the splitter plate. From chemiluminescence images acquired with a separate camera without PIV at a 45 degree angle to the burner center plane, the flame in the case 40:200 was found to extinguish between 20 and 23 mm downstream from the splitter plate. The variation in the flame edge location through the depth of the burner was found to be approximately 3 mm. The flame profile extracted from the PIV image pairs is path integrated, so the uncertainty as to the flame edge location in the PIV interrogation plane is affected by this uncertainty.

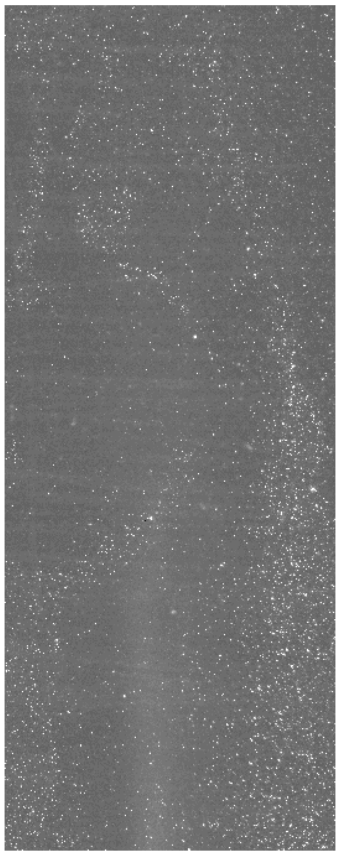

Figure 7.1 Sample image containing both seed particles and chemiluminescence. This image has been cropped to speed processing

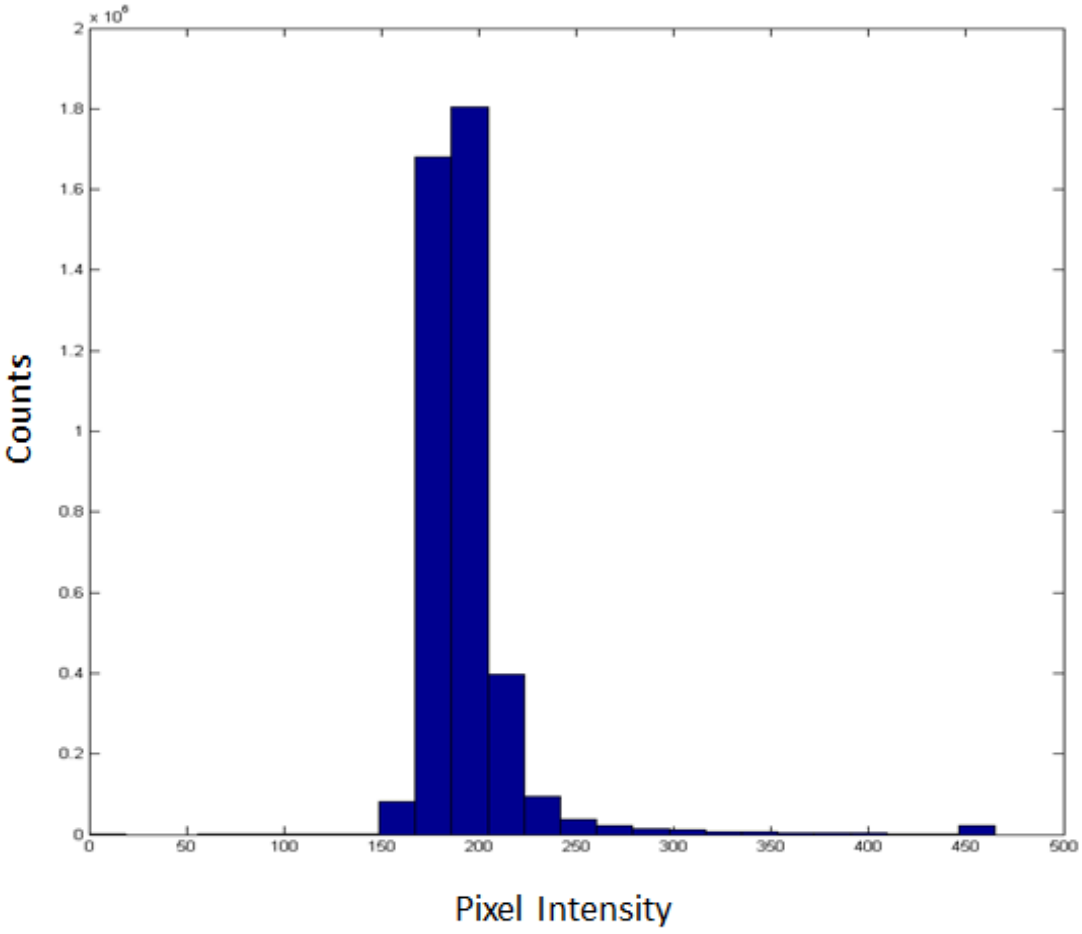

Figure 7.2 Histogram of pixel intensity for a sample image

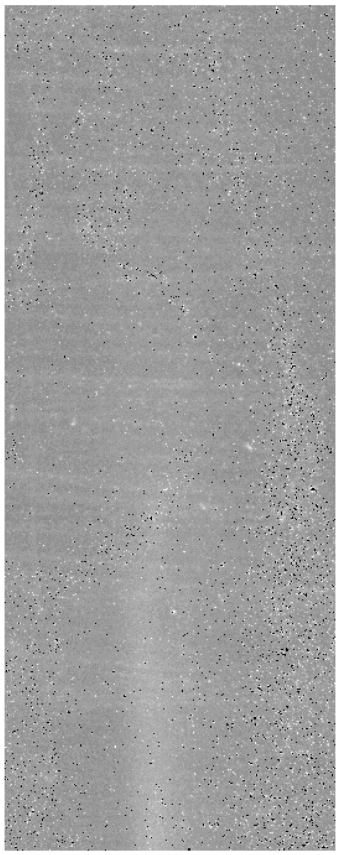

Figure 7.3 Sample image after seed particle signal removed

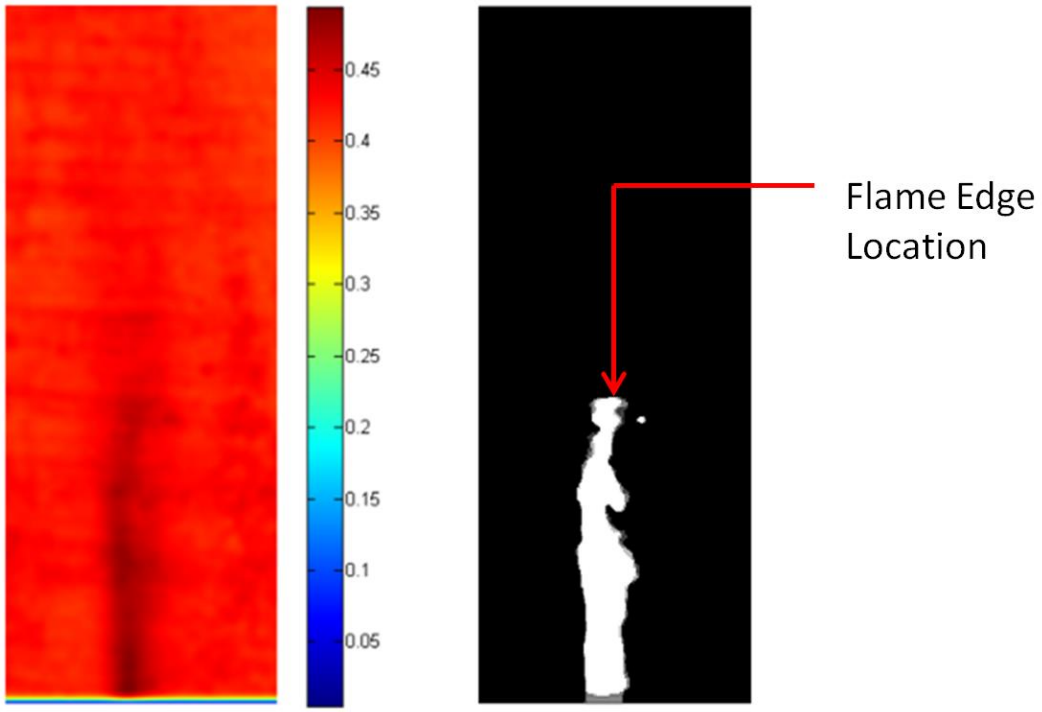

Figure 7.4 Sample filtered image (left) and extracted flame profile (right)

Flame Edge Locations

For each of the experimental conditions, the algorithm was applied to 1000 PIV image pairs. A validation check was used to ensure that the flame finding code returned a flame edge location inside the burner. If it did not, that data point was discarded. The X and Y positions were averaged (*Figures 7.5-6*), and the standard deviations were recorded (*Figures 7.7-8*). The average flame edge locations were all found to be within 1 mm of the center of the burner, except for the case 40:220, in which the average position was found to be approximately 2 mm to the left of the center plane of the burner. This could be due to an insufficient number of samples with an incomplete representation of the flames located to the right of the splitter plate. This is due to the fogging of the right side of the burner window with seed in many of the experimental trials. The average flame edge locations were found to be between 19.5 mm and 23 mm downstream from the splitter plate. There is a trend of higher jet velocities leading to flame extinction farther upstream in the burner. This agrees with the jet trajectory studies in Chapter 5. The standard deviation of the flame edge positions in the X direction appears to increase with side jet

velocity. This suggests increased turbulence at the flame edge, which was hypothesized in Chapter 6. This will be quantified later in the chapter. In the Y direction, the standard deviation decreased with increasing jet velocity. This suggests that the scalar dissipation rate in the region in which the flame edge is found is closer to steady state in the region of the burner closer to the splitter plate.

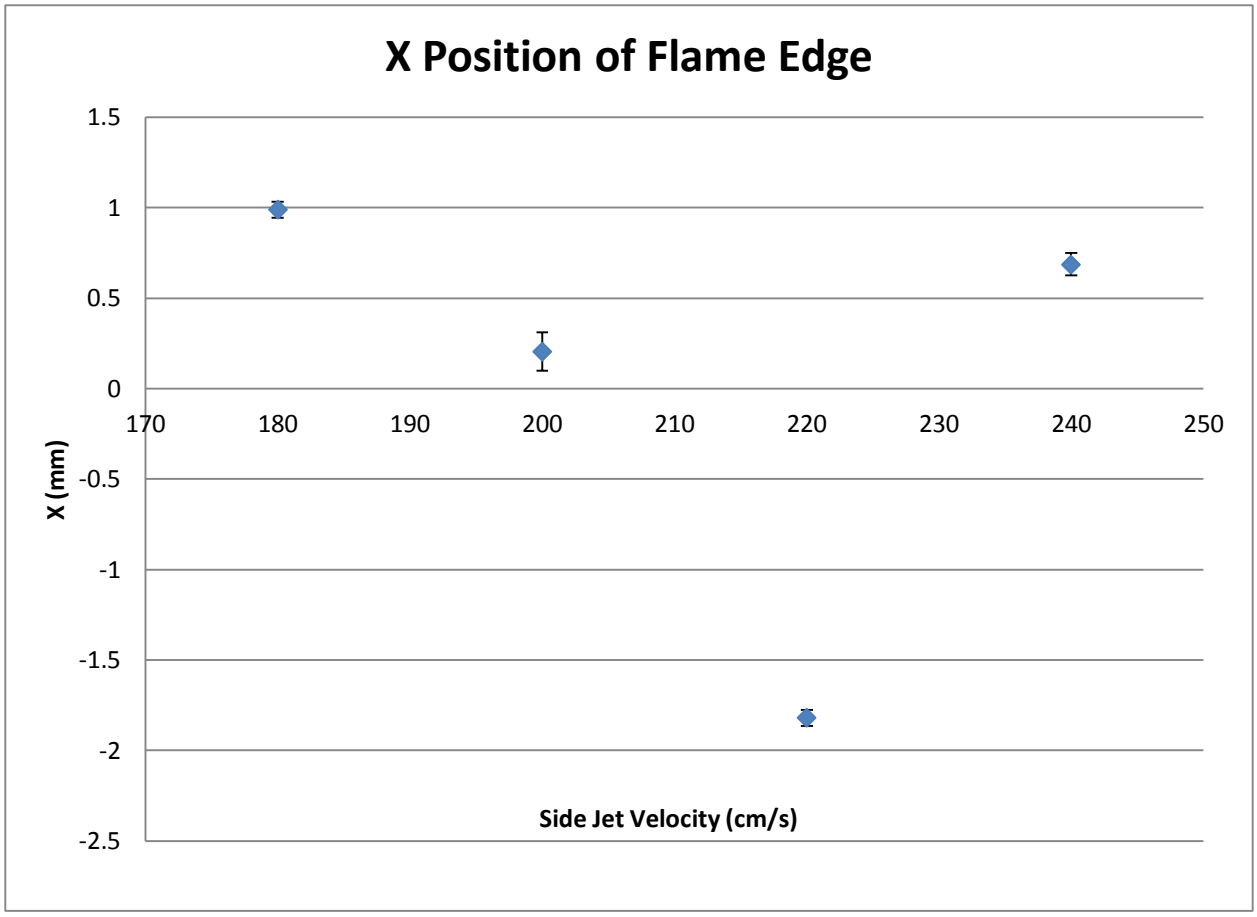

Figure 7.5 Average X position of the flame edge with constant 40 cm/s upstream velocity. Error bars are standard error of the mean.

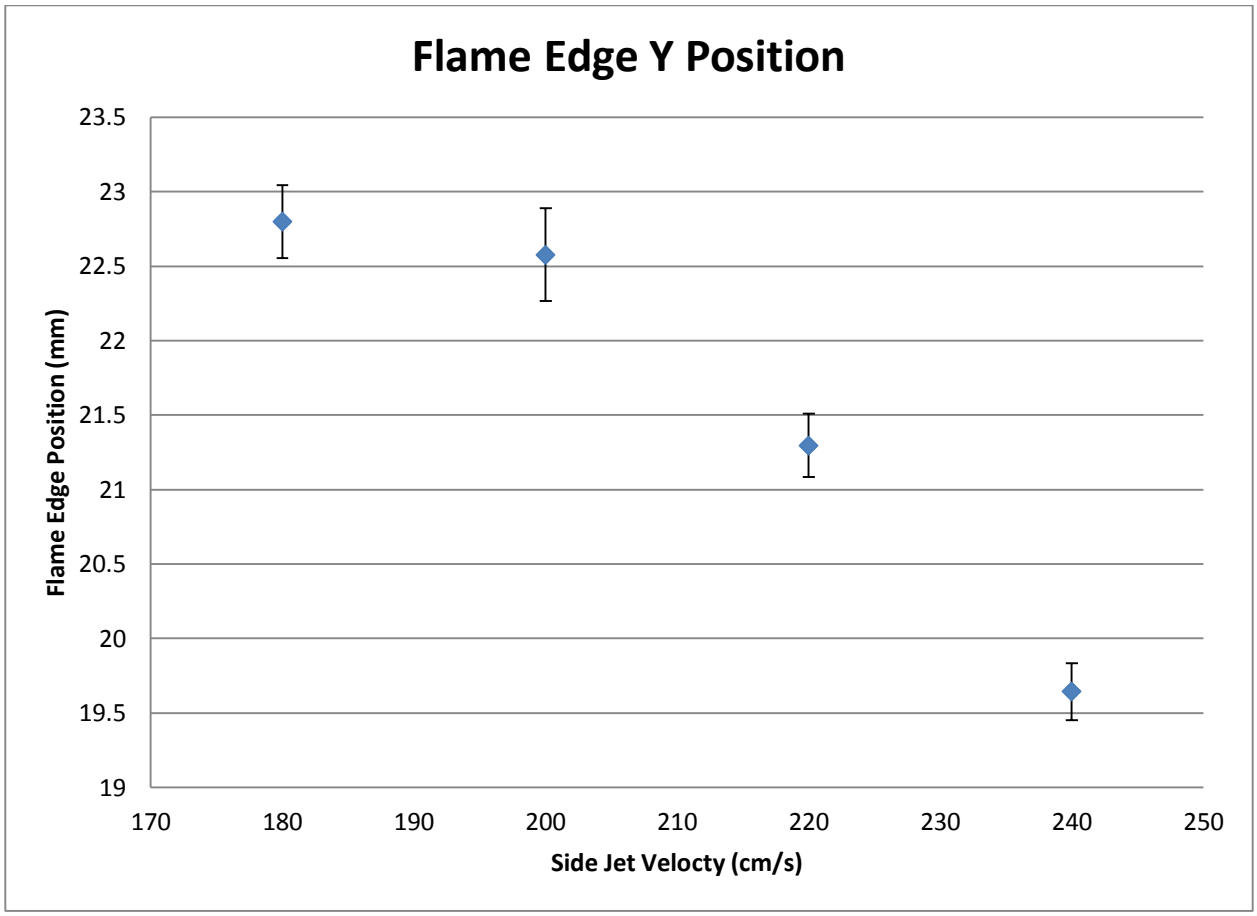

Figure 7.6 Average Y position of flame edge with constant 40 cm/s upstream velocity. Error bars are standard error of the mean

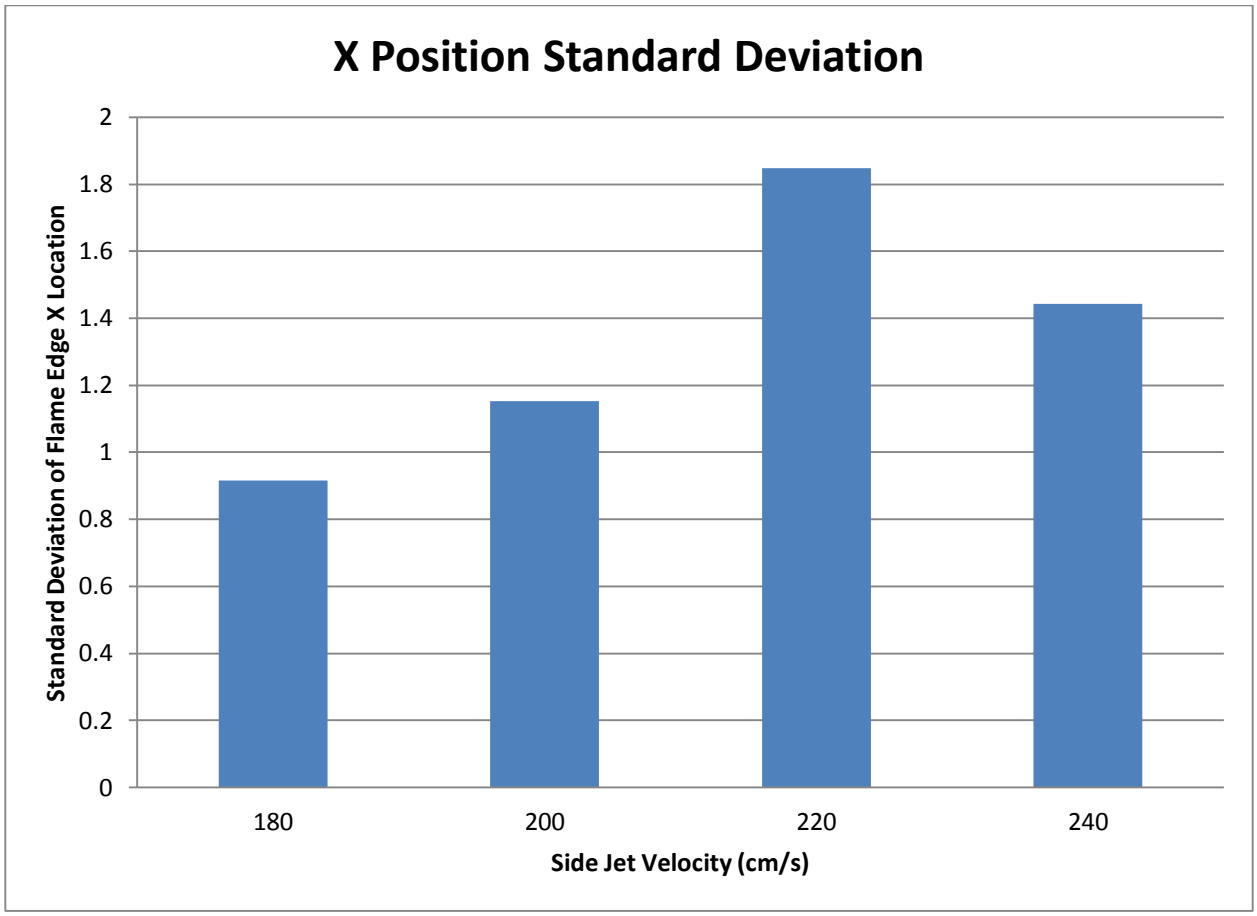

Figure 7.7 Standard deviation of X position for constant upstream velocity of 40 cm/s

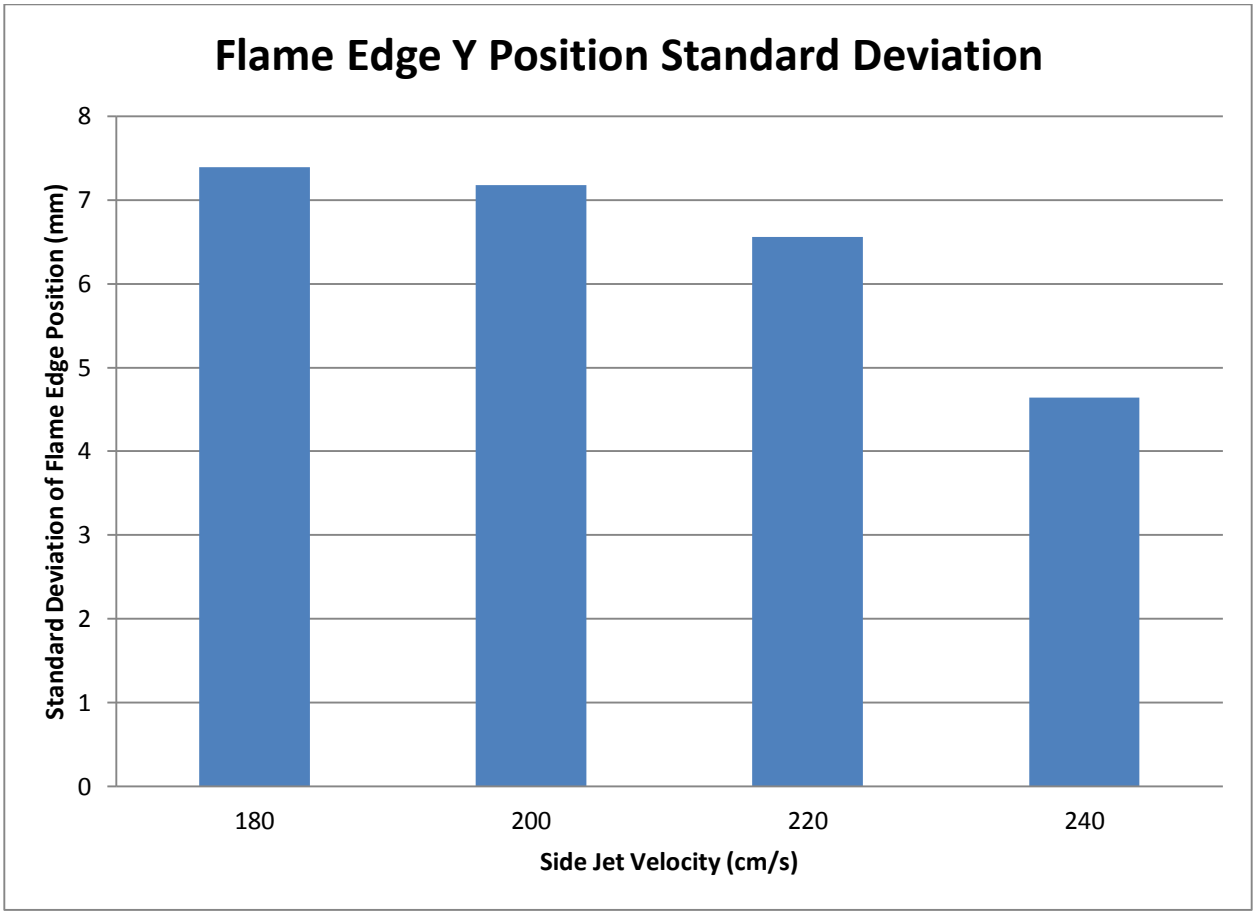

Figure 7.8 Standard deviation of the y position of the flame edge for constant upstream velocity of 40 cm/s

Flame Edge Velocities

The instantaneous velocities at the flame edge location were next obtained using nearest neighbor interpolation on the PIV vector field from the instantaneous flame edge locations found in the previous section. Since the flame sheet appears to be parallel to the burner center plane in most images, the V velocity is equivalent to the velocity through the flame edge, and the U velocity can be assumed to be normal to the flame sheet. The average U velocity component at the flame edge was observed to be within 0.1 m/s of zero for all experimental cases (*Figure 7.9*) except for the case 40:220. In this case, the x position was found to be at least twice as far off the centerline as any of the other cases. The difference in U velocity could be due to this observation. This would explain the positive velocity of 0.3 m/s observed, as the average velocity to the left of the splitter is positive (left to right). The average V

velocity component was found to be approximately equal to 1.2 m/s for all cases except for the case 40:240 (*Figure 7.10*). This exceptional case was found to have an average velocity at the edge of approximately 1.05 m/s. This is of particular interest, because this flame also extinguished the farthest upstream of all the cases, suggesting a link between the flame length and flame edge velocity. This could be due to varying heat fluxes through the edge, as a longer flame will have a higher adventive heat flux (Carnell 2006). The standard deviation of the flame edge velocities (*Figures 7.11-12*) appears to be increasing in both directions for increasing jet velocities. The exception to this is the U velocity standard deviation for the case 40:240, which is lower than both cases 40:200 and 40:220.

It is interesting to note that the average velocity magnitude appears relatively constant for all of the experimental cases, except for the case 40:220 where the flame was observed significantly farther away from the center plane than the other cases (*Figure 7.12*). This velocity magnitude does not necessarily truly represent the velocity through the flame edge, as the U velocity is seldom zero at any instantaneous flame edge. The higher observed velocity at the flame edge in the case 40:220 is due to the higher observed U velocities due to being located away from the center plane of the burner. The standard deviation of the velocity magnitude appears to increase as jet velocity increases, further suggesting that the flame edge exists in more turbulent conditions as the side jet velocity increases.

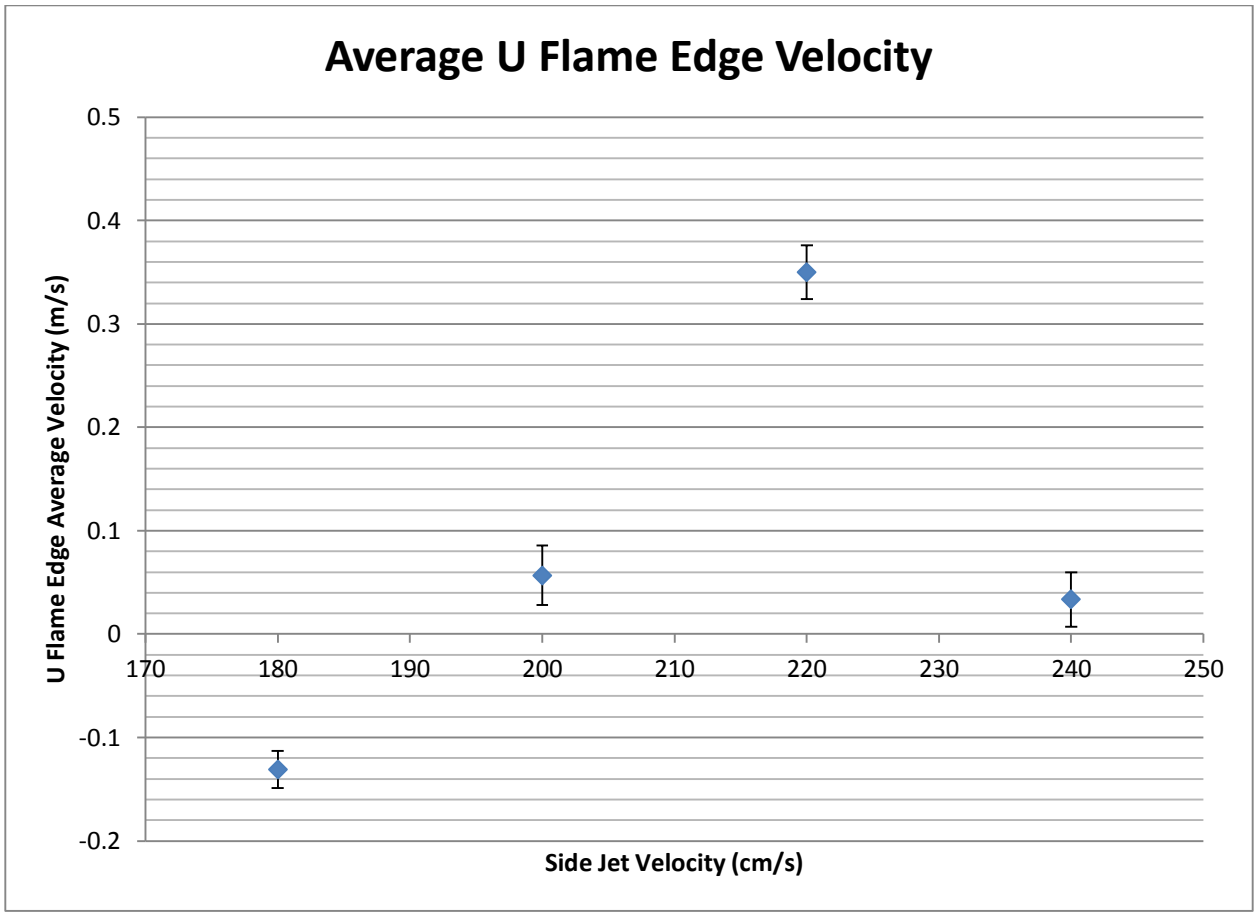

Figure 7.9 Average x-component velocities at flame edge locations for varying side jet velocities and constant 40 cm/s upstream velocity.

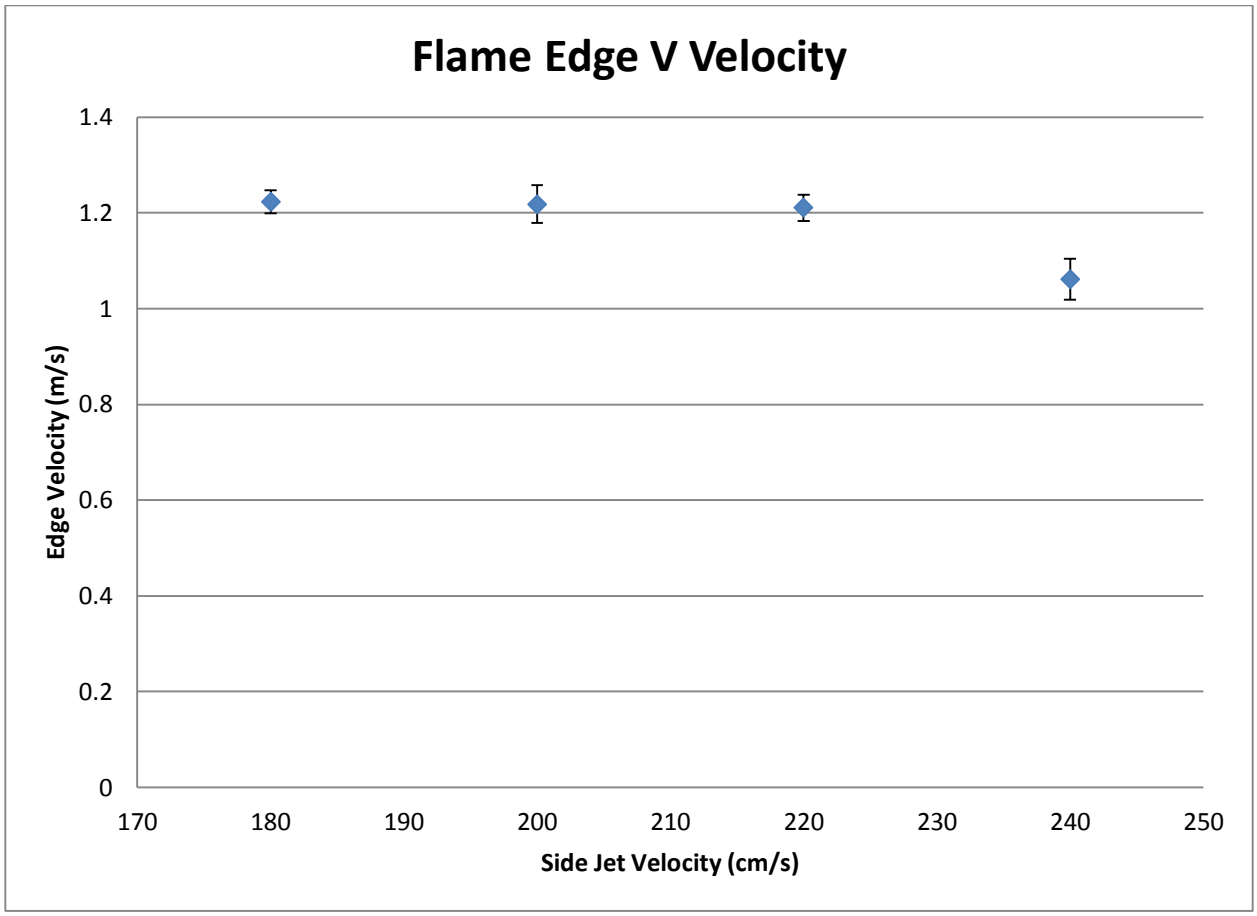

Figure 7.10 Y direction velocity components for varying downstream jet velocities with constant upstream velocity of 40 cm/s.

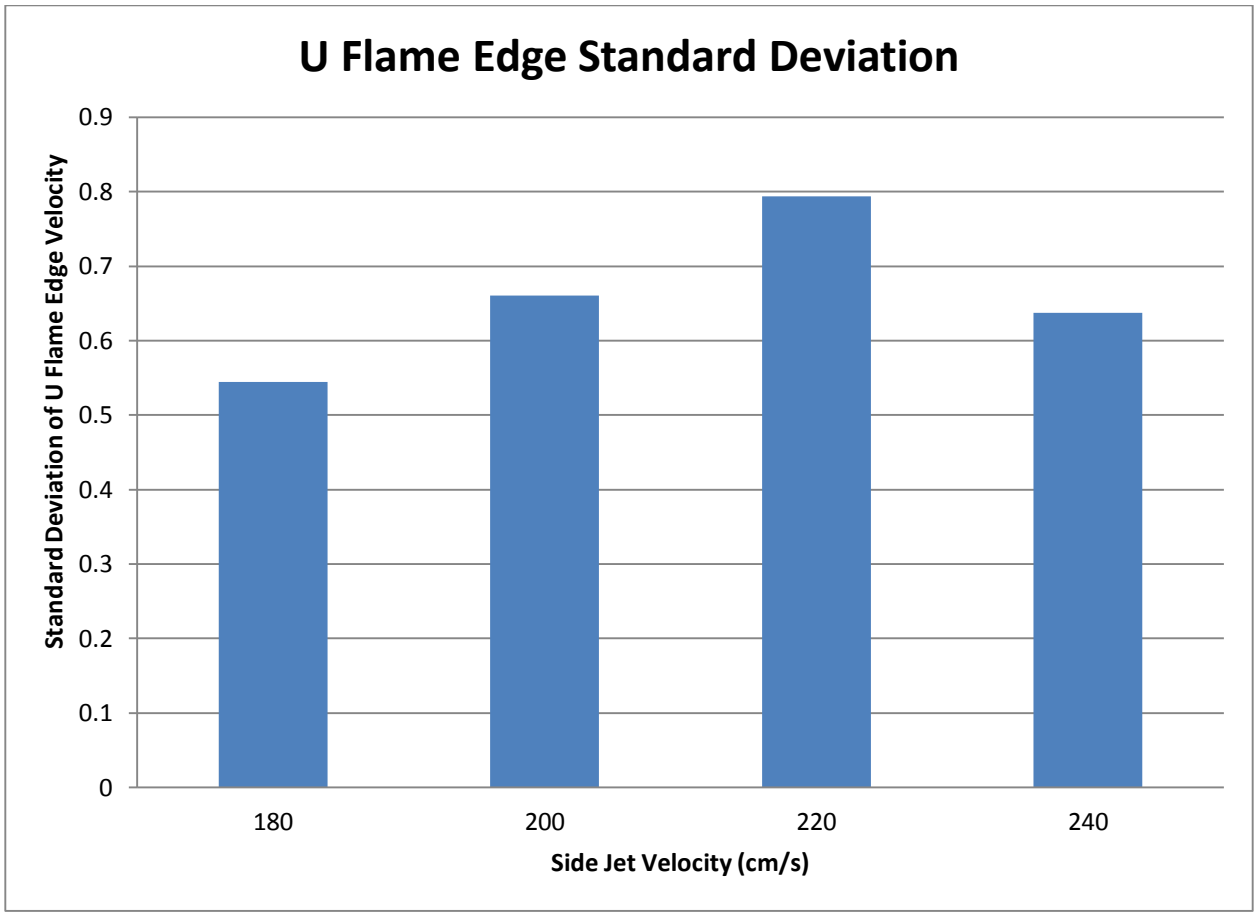

Figure 7.11 X direction velocity component standard deviations at flame edge locations for varying side jet velocities and constant upstream velocity of 40 cm/s

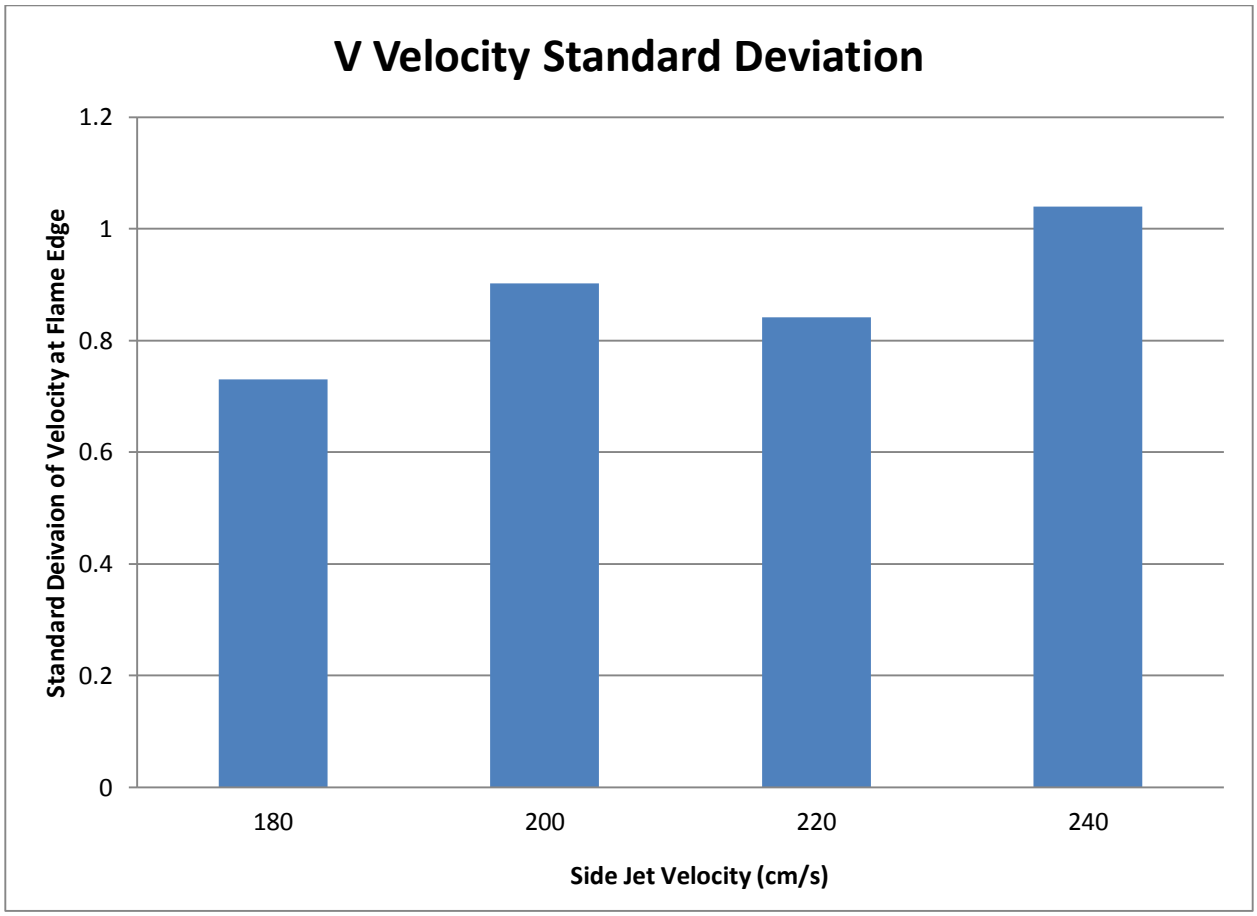

Figure 7.12 Y direction velocity component standard deviations at flame edge locations for varying side jet velocities and constant upstream velocity of 40 cm/s

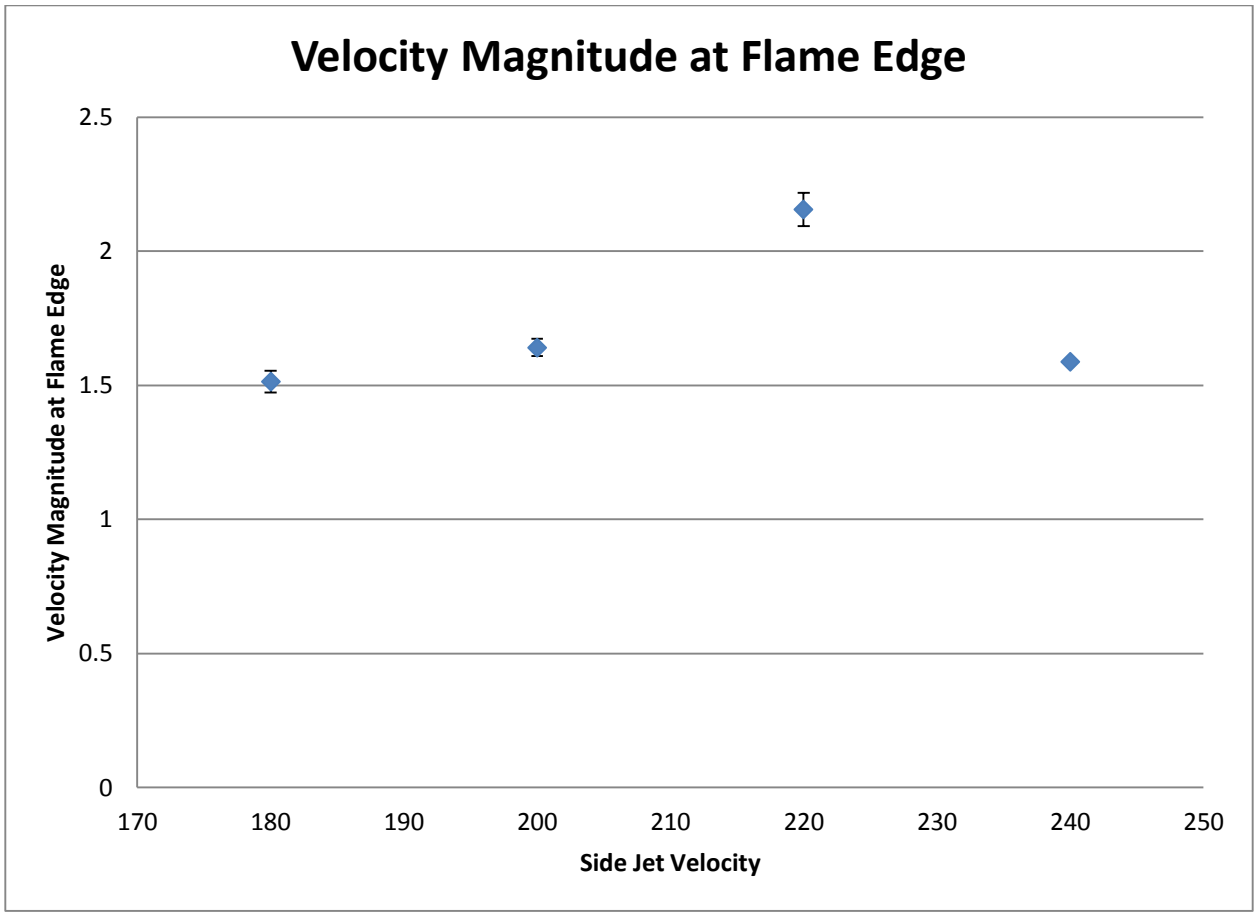

Figure 7.12 Average velocity magnitudes at flame edge locations for varying side jet velocities and constant upstream velocity of 40 cm/s

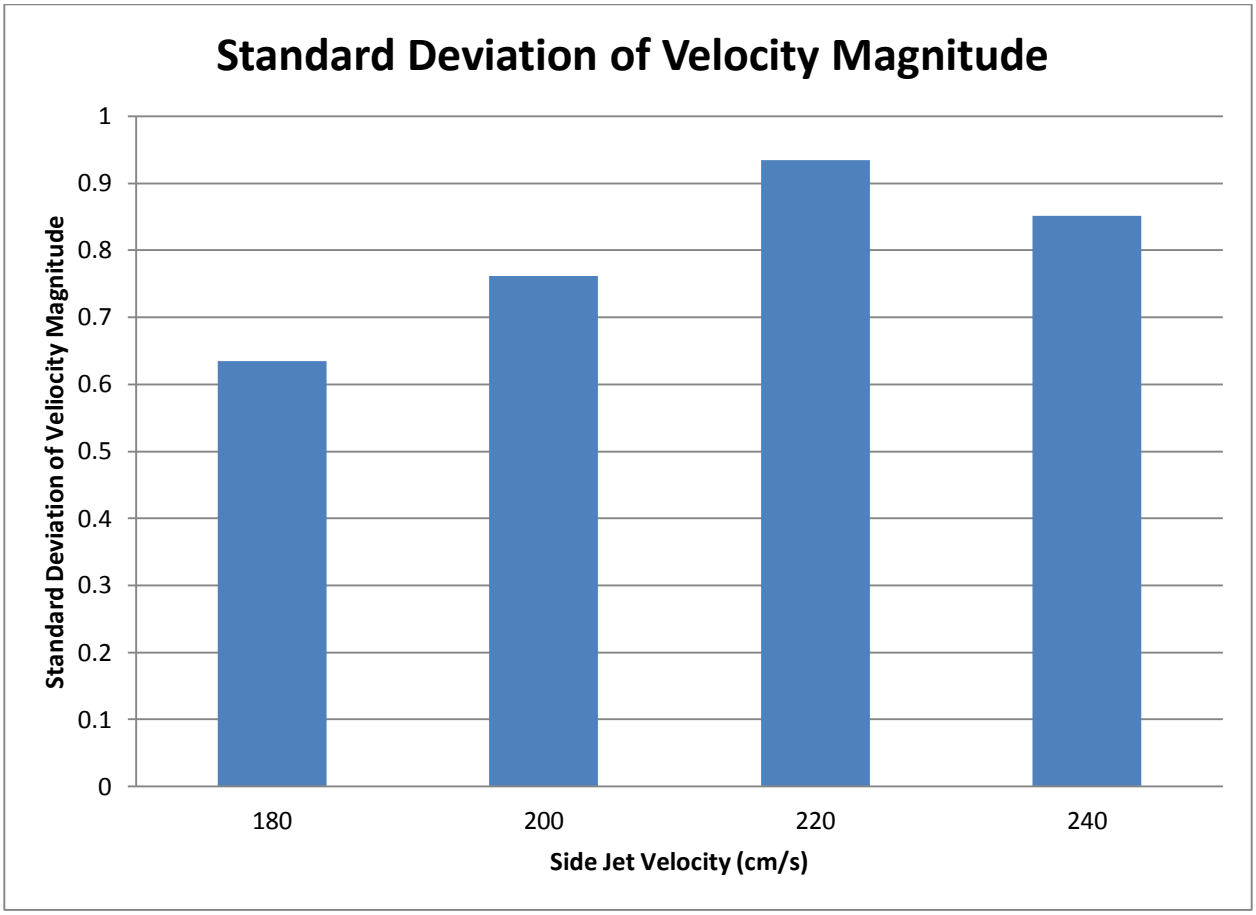

Figure 7.13 Standard deviations of velocities at flame edges for varying side jet velocities and constant upstream velocity of 40 cm/s

Coupled Velocity-Location Statistics

For future comparison to numerical simulations of this flame, it is of interest to determine if the velocity of the flame edge and the position of the flame edge are correlated. The correlation coefficient for the X position and U velocity was computed for all four experimental cases (*Table7.1*). A sample scatter plot is shown to illustrate the weak to moderate negative correlation between the U velocity and X position (*Figure 7.14*). This is expected, as the average field has positive U velocities for negative X coordinates and negative U velocities for positive U coordinates. The weakest correlation appears to be in the 40:180 case, in which the flame edge is the farthest downstream. The V velocities and the Y position also exhibit a weak to moderate correlation, but this correlation is observed to be positive. This suggests that flames farther downstream in the burner tend to have higher edge velocities than those

found farther upstream in the burner. The correlation appears to increase in strength with the side jet velocity, as the 40:240 case exhibits a significantly higher coefficient than the other cases.

Table 7.1 Covariance and Correlation Coefficient of X Position and U Velocity

Side Jet Velocity	Covariance	Correlation Coefficient
180	-0.08	-0.14
200	-0.36	-0.39
220	-0.55	-0.37
240	-0.34	-0.30

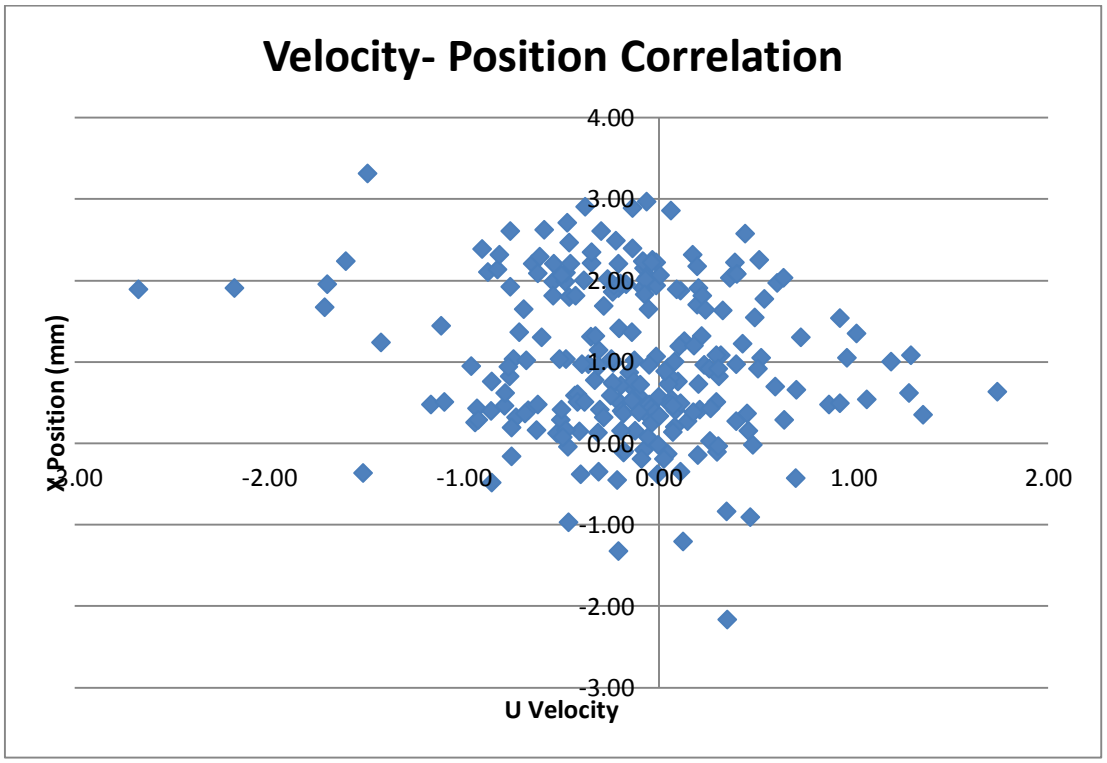

Figure 7.14 Velocity- Position plot for the case 180:40. This case shows the least strong correlation between U Velocity and X position.

Table 7.2 Covariance and Correlation Coefficient between Y Position and V Velocity

Side Jet Velocity	Covariance	Correlation Coefficient
180	0.49	0.30
200	0.67	0.34
220	0.56	0.30
240	0.76	0.42

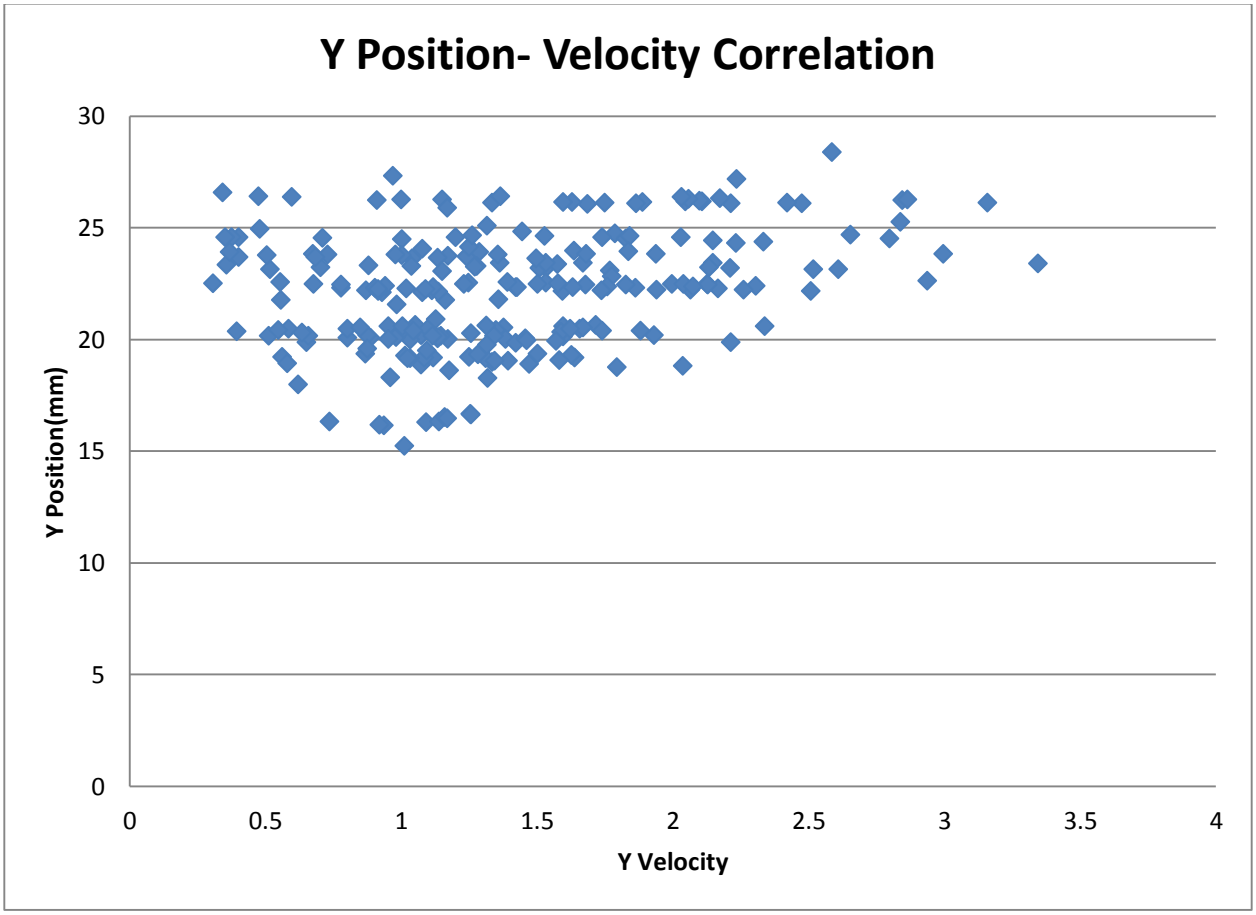

Figure 7.15 Y position velocity correlation for the case 40:180. This data shows a weak to moderate positive correlation

Average Flame Edge Statistics

The turbulent kinetic energy was calculated at the average position of each of the flames. Interestingly, this data showed no clear trend between side jet velocity and turbulent kinetic energy at the average flame location (*Figure 7.16*). This is in contrast to the values of standard deviation for V velocity and velocity magnitude presented in the previous section. Both of these parameters predicted

an increase in the turbulence at the flame edge with increasing jet velocity. This suggests that the average flow field is not a good representation of the conditions at the flame edge if the average flame edge position is used to obtain data. Instead, instantaneous velocities at the instantaneous locations must be compiled.

In the same way, if the averaged U and V velocities collected from the flame edges are compared to the average U and V velocities at the average flame positions the results are different. The sampling at the average flame edge location tends to over-predict the velocity by approximately 25%. This has important implications in the modeling of this type of flame, as a RANS model will not predict the flame edge appropriately.

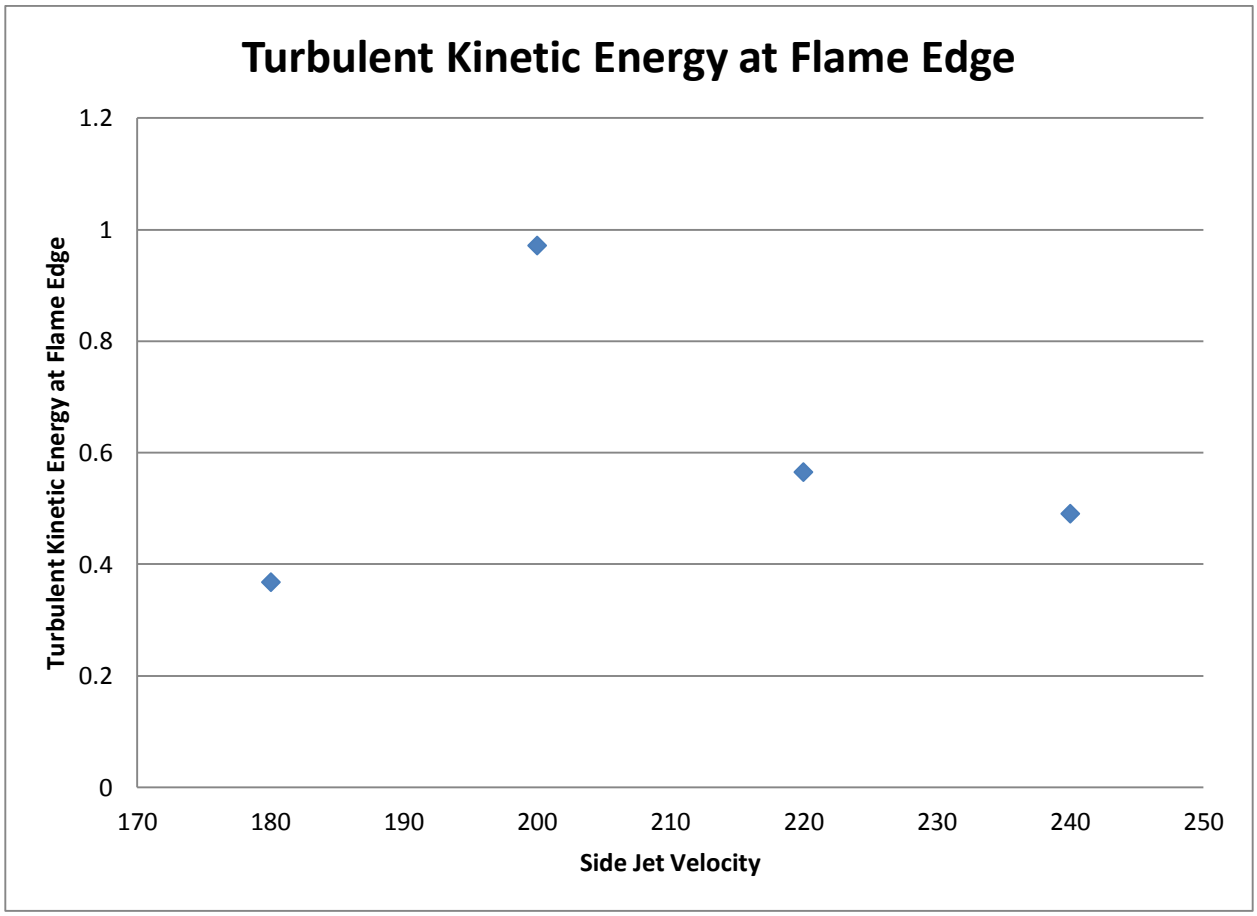

Figure 7.16 Turbulent kinetic energy at the average flame edge location for varying side jet velocities with constant upstream velocity of 40 cm/s

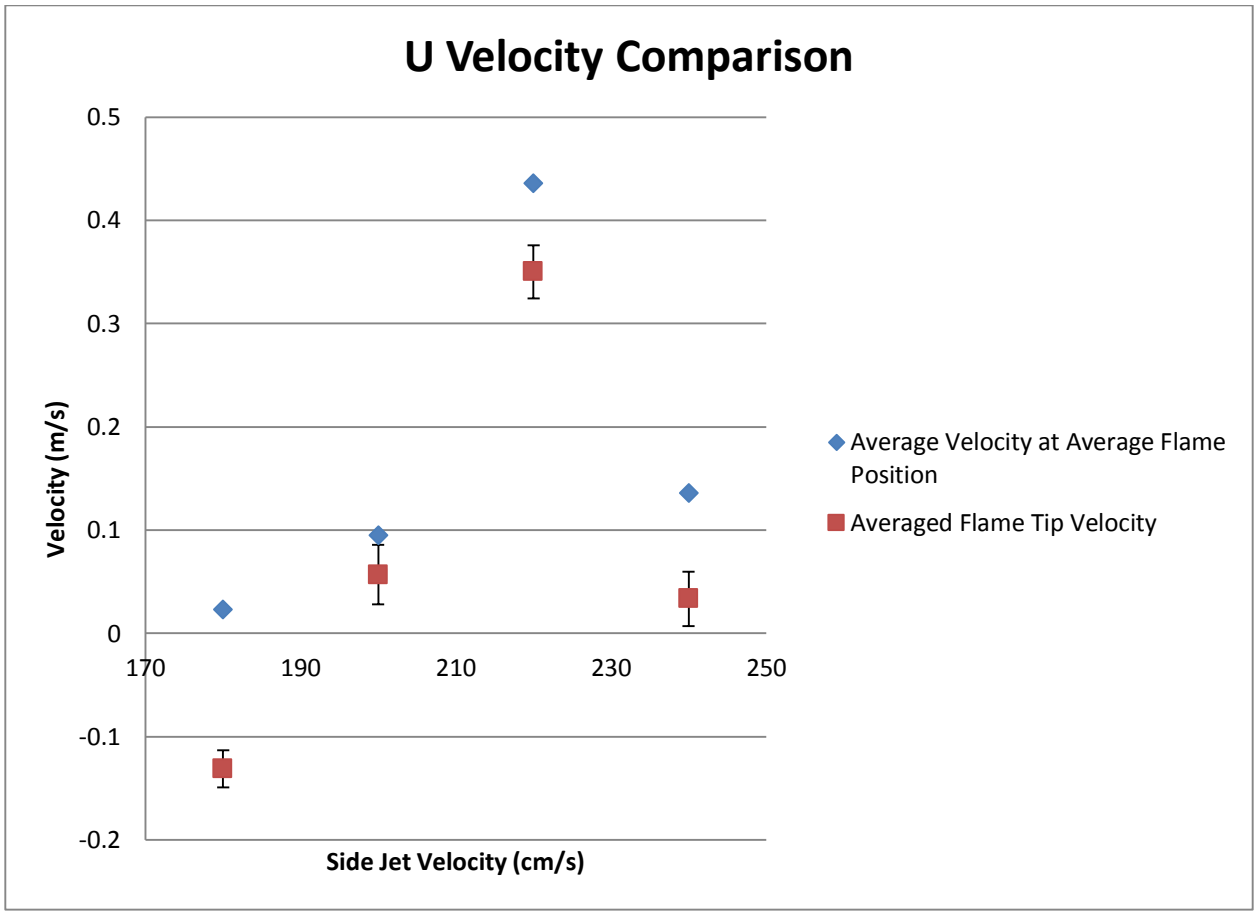

Figure 7.17 Comparison of the averaged flame edge U Velocities and the average velocity at the average flame edge location

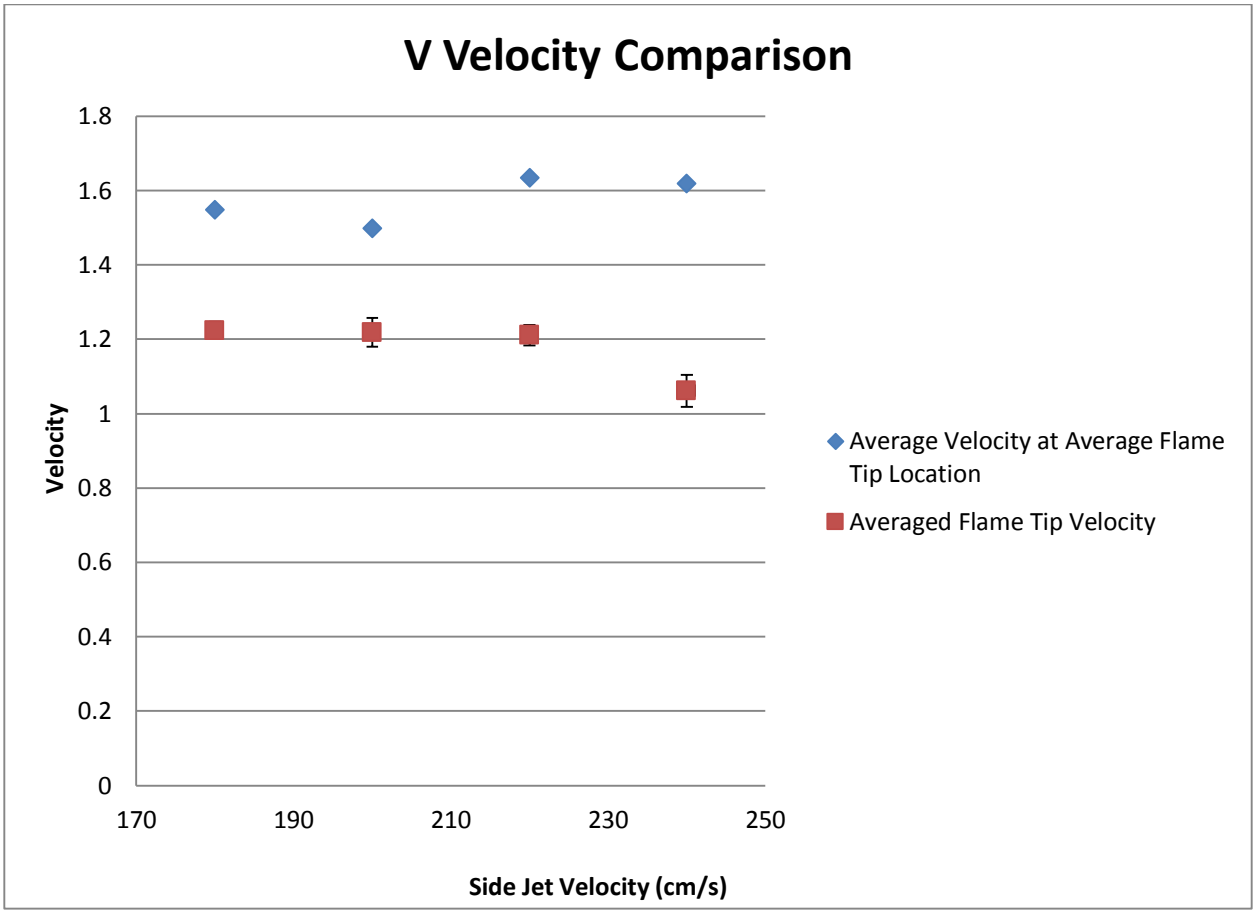

Figure 7.18 Comparison of the averaged flame edge V Velocities and the average velocity at the average flame edge location

Summary

In this chapter, a novel method for extracting a flame profile from PIV Mie scattering imaging pairs is presented. Using this method, average flame locations are provided for each experimental condition tested. The averaged velocities at the flame edge were calculated and presented. This velocity was found to be near constant for all cases except for the highest side jet velocity case, which exhibited a lower average edge velocity. A weak to moderate negative correlation between X position of the flame edge and the U velocity was found. In addition, a weak to moderate positive correlation between Y position of the flame and V velocity was found. Values for turbulent kinetic energy at the average flame location were presented, and velocity components from these locations were also presented. The average velocities at the average flame location were compared to the averaged velocities from the

individual flame edges, and a discrepancy between the two was noted. The average flow field data seems to be able to predict trends in the x direction, but is unreliable in the y direction. This suggests coupling between the flow field and chemistry, as is expected in a reacting flow.

Chapter 8: Conclusions

Commercial CFD codes were used to perform parametric analyses on burner geometries to create a statistically stationary negative flame edge in a laboratory setting. Both reacting and non-reacting simulations were used to predict the extinction of a flame edge in the burner. Final slot burner geometry was selected and constructed. This geometry was shown to create a negative flame edge using impinging jets on a diffusion flame sheet.

Particle imaging velocimetry (PIV) experiments were performed to characterize the boundary conditions at the inlet for the impinging jets. Polynomial fits for the mean velocity profile and turbulent kinetic energy were presented.

PIV was performed to characterize the flow field in the burner. The jet penetration and deflection were analyzed, in addition to the average velocity field and the turbulent kinetic energy.

A novel algorithm to extract chemiluminescence imaging from PIV image pairs was presented, and velocity and position statistics were presented at the flame edge. Negative edge velocities on the order of 1 m/s were found in this burner. This is in agreement with the studies performed on laminar flames reporting edge velocities between 1 and 6 m/s (Carnell and Renfro 2006). In addition, this is in agreement with edge velocities simulated between 0 and 2 m/s in DNS studies (Pantano and Pullin 2004)

Future Work

In order to fully understand the effects of turbulent kinetic energy on flame edge behavior, the experiments in this thesis should be repeated using different inlet turbulence conditions. This will allow the isolation of the effects of inlet turbulence intensity and inlet velocity on the flame edge statistics. In addition, different fuels and dilution ratios should be studied to quantify the effects of these variables on the turbulence-chemistry interaction that leads to flame hole formation.

Turbulent simulations should be performed using the boundary conditions provided in this thesis to analyze the effectiveness of existing models in predicting extinction flame edges in turbulent combustion.

In order to validate the accuracy of the flame edge finding algorithm, results from planar induced florescence (PLIF) imaging should be compared to the chemiluminescence images acquired in this thesis. Radicals important to the combustion process such as CH* and OH* should be imaged along with formaldehyde to provide reaction rate contours to compare with simulations. This will also reduce the uncertainty involved in chemiluminescence imaging, as there is no out of plane contributions in a PLIF measurement. Simultaneous PLIF and PIV measurements would provide a direct comparison to the statistical information at the flame edge provided in this thesis.

Works Cited

Amantini, Giuliano, Jonathan H. Frank, Alessandro Gomez, Hong G. Im, Suresh Aggarwal, and Jacqueline H. Chen. 2005. "Experiments on Standing and Traveling Edge Flames around Flame Holes." *Proceedings of the Combustion Institute* 30 I (1). The Combustion Institute: 313–21. doi:10.1016/j.proci.2004.08.230.

Bergmann, V., W. Meier, D. Wolff, and W. Stricker. 1998. "Application of Spontaneous Raman and Rayleigh Scattering and 2D LIF for the Characterization of a Turbulent CH 4 /H 2 /N 2 Jet Diffusion Flame." *Applied Physics B: Lasers and Optics* 66 (4): 489–502.

Bilger, RW, SH Stårner, and RJ Kee. 1990. "On Reduced Mechanisms for Methane Air Combustion in Nonpremixed Flames." *Combustion and Flame*. http://www.sciencedirect.com/science/article/pii/0010218090901228.

Biswas, Sayan, Kristin Kopp-Vaughn, Michael W. Renfro, and Baki M. Cetegen. 2013. "Phase Resolved Characterization of Conical Premixed Flames near and far from Blowoff." *Combustion and Flame* 160: 2843–55. doi:10.1016/j.combustflame.2013.06.014.

Boulanger, Joan, Luc Vervisch, Julien Reveillon, and Sandip Ghosal. 2003. "Effects of Heat Release in Laminar Diffusion Flames Lifted on Round Jets." *Combustion and Flame* 134 (4): 355–68. doi:10.1016/S0010-2180(03)00114-7.

Boxx, I., C. Heeger, R. Gordon, B. Böhm, M. Aigner, a. Dreizler, and W. Meier. 2009. "Simultaneous Three-Component PIV/OH-PLIF Measurements of a Turbulent Lifted, C3H8-Argon Jet Diffusion Flame at 1.5 kHz Repetition Rate." *Proceedings of the Combustion Institute* 32 I (1): 905–12. doi:10.1016/j.proci.2008.06.023.

Brockhinke, Andreas, Andreas Bülter, Juan C. Rolon, and Katharina Kohse-Höinghaus. 2001. "Ps-LIF Measurements of Minor Species Concentration in a Counterflow Diffusion Flame Interacting with a Vortex." *Applied Physics B: Lasers and Optics* 72: 491–96. http://link.springer.com/article/10.1007/s003400100535.

, W. F., and M. W. Renfro. 2006. "Influence of Advective Heat Flux on Extinction Scalar Dissipation Rate and Velocity in Negative Edge Flames." *Combustion Theory and Modelling* 10 (5): 815–30. doi:10.1080/13647830600719969.

Carnell, W.F. Jr. 2006. "Experimental and Numerical Study of Extinction in Negative Edge Laminar Flames."

Carnell, W.F. Jr., and M W Renfro. 2007. "Measurement of Temperature Gradients through Local Extinction Using Raman Scattering Spectroscopy." *International Journal of Alternative …*. http://inderscience.metapress.com/index/D04832V781812780.pdf.

Carnell, William F, Kathryn R Gosselin, Michael W Renfro, and Auditorium Rd. 2009. "Comparison of Measured and Simulated OH and CH 2 O Distributions through a Local Extinction", no. 2: 1–9.

Carnell, William F., and Michael W. Renfro. 2005. “Stable Negative Edge Flame Formation in a Counterflow Burner.” *Combustion and Flame* 141 (4): 350–59. doi:10.1016/j.combustflame.2005.01.010.

Cha, Min Suk, and Paul D. Ronney. 2006. “Propagation Rates of Nonpremixed Edge Flames.” *Combustion and Flame* 146 (1-2): 312–28. doi:10.1016/j.combustflame.2006.02.010.

Chen, Yung Cheng, and Robert W. Bilger. 2000. “Stabilization Mechanisms of Lifted Laminar Flames in Axisymmetric Jet Flows.” *Combustion and Flame* 123 (1-2). Elsevier Science Publ Co Inc: 23–45.

Daou, R., J. Daou, and J. Dold. 2002. “Effect of Volumetric Heat Loss on Triple-Flame Propagation.” *Proceedings of the Combustion Institute* 29 (2): 1559–64.

Favier, Valérie, and Luc Vervisch. 2001. “Edge Flames and Partially Premixed Combustion in Diffusion Flame Quenching.” *Combustion and Flame* 125 (1-2): 788–803.

Hult, J., U. Meier, W. Meier, a. Harvey, C. F. Kaminski, Graham Nathan, Mohy S. Mansour, Heinz Pitsch, and Alesandro Gomez. 2005. “Experimental Analysis of Local Flame Extinction in a Turbulent Jet Diffusion Flame by High Repetition 2-D Laser Techniques and Multi-Scalar Measurements.” *Proceedings of the Combustion Institute* 30 I (1): 701–9. doi:10.1016/j.proci.2004.08.069.

Im, H. G., and J. H. Chen. 1999. “Structure and Propagation of Triple Flames in Partially Premixed Hydrogen-Air Mixtures.” *Combustion and Flame* 119 (4). Elsevier Science Publ Co Inc: 436–54.

Jr, S Kostka, WF Carnell Jr, and MW Renfro. 2007. “Numerical Study of Neighboring Edge Flame Interactions.” *A Collection of the Technical Papers 45th AIAA Aerospace Sciences Meeting. Reno, Nevada, 8-11 January, 2007* 1-24: 4613–21. http://arc.aiaa.org/doi/pdf/10.2514/6.2007-377.

Kĩoni, P. N., K. N C Bray, D. a. Greenhalgh, and B. Rogg. 1999. “Experimental and Numerical Studies of a Triple Flame.” *Combustion and Flame* 116 (1-2): 192–206.

Kioni, PN, B Rogg, KNC Bray, and A Linán. 1993. “Flame Spread in Laminar Mixing Layers: The Triple Flame.” *Combustion and Flame*. http://www.sciencedirect.com/science/article/pii/001021809390132M.

Lee, J., S. H. Won, S. H. Jin, and S. H. Chung. 2003. “Lifted Flames in Laminar Jets of Propane in Coflow Air.” *Combustion and Flame* 135 (4): 449–62. doi:10.1016/S0010-2180(03)00182-2.

Li, Z. S., B. Li, Z. W. Sun, X. S. Bai, and M. Aldén. 2010. “Turbulence and Combustion Interaction: High Resolution Local Flame Front Structure Visualization Using Simultaneous Single-Shot PLIF Imaging of CH, OH, and CH2O in a Piloted Premixed Jet Flame.” *Combustion and Flame* 157 (6). The Combustion Institute. 1087–96. doi:10.1016/j.combustflame.2010.02.017.

Meyer, T. R., G. J. Fiechtner, S. P. Gogineni, J. C. Rolon, C. D. Carter, and J. R. Gord. 2004. “Simultaneous PLIF/PIV Investigation of Vortex-Induced Annular Extinction in H 2 -Air Counterflow Diffusion Flames.” *Experiments in Fluids* 36 (2): 259–67. doi:10.1007/s00348-003-0698-6.

Nguyen, Quang Viet, and Phillip H. Paul. 1996. “The Time Evolution of a Vortex-Flame Interaction Observed via Planar Imaging of CH and OH.” *Symposium (International) on Combustion* 26: 357–64. doi:10.1016/S0082-0784(96)80236-0.

Nicolaides, D, D Honnery, and J Soria. 2004. “Autocorrelation Functions and the Determination of Integral Length with Reference to Experimental and Numerical Data”, no. December.

Pantano, C. 2004. “Direct Simulation of Non-Premixed Flame Extinction in a Methane–air Jet with Reduced Chemistry.” *Journal of Fluid Mechanics* 514 (September): 231–70. doi:10.1017/S0022112004000266.

Pantano, C., and D.I. Pullin. 2004. “A Statistical Description of Turbulent Diffusion Flame Holes.” *Combustion and Flame* 137 (3): 295–305. doi:10.1016/j.combustflame.2004.02.001.

Pearce, Philip, and Joel Daou. 2013. “The Effect of Gravity and Thermal Expansion on the Propagation of a Triple Flame in a Horizontal Channel.” *Combustion and Flame* 160 (12). The Combustion Institute. 2800–2809. doi:10.1016/j.combustflame.2013.06.017.

Phillips, H. 1965. “Flame in a Buoyant Methane Layer.” In *Symposium (International) on Combustion*, 10:1277–83. doi:10.1016/S0082-0784(65)80262-4.

Pitsch, Heinz, Chong M Cha, and Sergei Fedotov. 2003. “Flamelet Modelling of Non-Premixed Turbulent Combustion with Local Extinction and Re-Ignition Flamelet Modelling of Non-Premixed Turbulent Combustion with Local Extinction and Re-Ignition.” *Combustion Theory and Modelling* 7 (x): 317–32.

Rolon, J. 1995. “Experiments on the Interaction between a Vortex and a Strained Diffusion Flame.” *Combustion and Flame* 100 (3): 422–26.

Ruetsch, G. R., L. Vervisch, and A. Liñán. 1995. “Effects of Heat Release on Triple Flames.” *Physics of Fluids* 7: 1447–54. doi:10.1063/1.868531.

Santoro, VS, A Liñán, and A Gomez. 2000. “Propagation of Edge Flames in Counterflow Mixing Layers: Experiments and Theory.” *Proceedings of the Combustion Institute*. http://www.sciencedirect.com/science/article/pii/S0082078400806116.

Shay, Michael L., and Paul D. Ronney. 1998. “Nonpremixed Edge Flames in Spatially Varying Straining Flows.” *Combustion and Flame* 112 (1-2): 171–80.

Watson, K A, K M Lyons, J M Donbar, and C D Carter. 1999. “Scalar and Velocity Field Measurements in a Lifted CH 4 – Air Diffusion Flame” 2180 (98).

Watson, K. a., K. M. Lyons, J. M. Donbar, and C. D. Carter. 2000. “Simultaneous Rayleigh Imaging and CH-PLIF Measurements in a Lifted Jet Diffusion Flame.” *Combustion and Flame* 123 (1-2). Elsevier Science Publ Co Inc: 252–65.

XU, Y, and MD SMOOKE. 1993. “Primitive Variable Modeling of Multidimensional Laminar Flames.” *Combustion Science and …*. http://www.tandfonline.com/doi/abs/10.1080/00102209308907619.

Yamamoto, Kazuhiro, Shinji Isii, and Masahiro Ohnishi. 2011. “Local Flame Structure and Turbulent Burning Velocity by Joint PLIF Imaging.” *Proceedings of the Combustion Institute* 33 (1). Elsevier Inc. 1285–92. doi:10.1016/j.proci.2010.06.087.

Yang, S. Y., S. K. Ryu, B. K. Lee, and S. H. Chung. 2009. “Extinction of Interacting Nonpremixed Flames and Existence of Stationary Retreating Edges in Twin-Jet Counterflow.” *Combustion Theory and Modelling* 13 (2): 235–50. doi:10.1080/13647830802578411.

Zhang, Huiqiang, Fan Yang, and Xilin Wang. 2012. “The Effects of Soret Diffusion on Extinction Limit in Premixed and Diffusion Counterflow N-Butane/Air Flames.” *Combustion Science and Technology* 184 (4): 517–32. doi:10.1080/00102202.2011.648035.

Appendix 1:

Processing Codes for PIV Image Pairs and Extraction of Chemiluminescence

Main Shell Program

```
%stats
%big for loop to make the b* and get out the velocity components
%Calls all of the other functions
%start frame
startval=30;
%end frame
endval=1000;
numels=endval-startval+1;
%initialize variables
x=zeros(1,numels);
y=x;
u=x;
v=x;
%Make filenames and call the other routine to gather the statistics
for i=startval:endval
    %make the filename
    if i <10
        filename=strcat('B0000',num2str(i));
    elseif i <100
        filename=strcat('B000',num2str(i));
    elseif i <1000
        filename=strcat('B00',num2str(i));
    elseif i<10000
        filename=strcat('B0',num2str(i));
    end
    fprintf(filename);
    fprintf('\n');
    %call sender to get the values of everything
    [x(i) y(i) u(i) v(i)]=sender(filename);
end

save('Run4.mat');
quit
```

Sub-Shell Program to Extract Image Data, Calls Nearest Neighbor Interpolator to Get Edge Speed Data

```
function [ x y u v ] = sender( framename )
%Sender Returns the values of x,y,u,v for the current frame
frame=framename;
%make the full path for the flame finder and velocity extractor
miename=strcat('Mie\Run4\',frame,'.IM7');
vecname=strcat('Vectors\Run4\',frame,'.VC7');
%run the flame finder
[y x]=flameextract(miename);
%knowing that this works now, we need to extract the velocity field
%information
[u v]=velgrab(vecname,x,y);
end
```

Program to Extract Flame Position

```
function [ pixelrow,pixelcol ] = flameextract( filepath )
%flameextract Returns the x and y positions of the flame edge
%     NonLinear Diffusion Filter called in this code
a=readimx(filepath);
%extract frames
first=a.Data(:,1:2048);
second=a.Data(:,2049:end);
img=second(600:1400,:);
%normalize
img=double(img)./double(max(max(img)));
[n x]=hist(reshape(img,1,numel(img)),25);
%Find a good filter value
%max of the histogram and location
[val loc]=max(n);
for i= loc:numel(n)
    if n(i)<= val*.05
        filval=x(i);
        break
    end
end
%filter out the top portion of the image intensity
img(img>filval)=0;
%Perform Non-Linear Diffusion Using Wickert Kernel
h=NonLinAnisoDiff2D(img,500,.2,'wckrt',[15,3,4,3.31488,1]);
%Do it again with different filter size and constants
j=NonLinAnisoDiff2D(h,50,.2,'wckrt',[50,2,4,3.314888,0]);

%filter by anything that's more the 75% of the standard deviation
k=j;
filval=mean(mean(k))+.75*std(reshape(k,1,numel(k)));
k(k>filval)=1;
k(k<=filval)=0;
%figure
%select the flame
k=bwselect(k,2000,350);
%figure
%imshow(k', [0 1])
%loop through the matrix to find the first flame value(from the top)
for i=2000:-1:1
    if max(k(:,i)) == 0
        pixelrow=i+1;
        temp=k(:,i+1);
        %Calculate the center of the edge
            a=sum(temp);
            b=sum(temp.*(1:length(temp))');
            pixelcol=b./a;
            pixelcol=pixelcol+600;
        break
    end

end

end
```

Non-Linear Diffusion Filter

```
function diff_im = NonLinAnisoDiff2D(varargin)
%Nonlinear anisotropic diffusion filter for 2-dimensional domains.
% diff_im = NonLinAnisoDiff2D(im,num_iter,dt);
%   Default input form
%   im:         2D-image
%   num_iter:   Number of iterations
%   dt:         Time step
% diff_im = NonLinAnisoDiff2D(im,num_iter,dt,flag,[input]);
%   flag,[input]
% diff_im = NonLinAnisoDiff2D(im,num_iter,dt,'perona');
% diff_im = NonLinAnisoDiff2D(im,num_iter,dt,'perona',[kappa option]);
%    'perona',[kappa option]    Default, applies the diffusion kernel from
%       Perona and Malik, which is applied to the gradient of the image
%       intensity. Requires the input arguments of kappa, that determines
%       the gradient normalization, or the amount of weighting that the
%       gradient drives the image diffusion. The option argument is ether 1
%       or 0, where 1 emphasizes wide regions and 0, the default,
%       emphasizes high contrast edges over low-contrast edges.
% diff_im = NonLinAnisoDiff2D(im,num_iter,dt,'wckrt',[wid sigma m Cm lam])
%    'wckrt',[wid m Cm lam]     Applies the diffusion kernel of Weickert
%       applied to the gradient of the Gaussian convolution of the image
%       intensity. The input options must be defined, please see the papers
%       by Weickert and Malm et al. for details and application.
%       wid:    Gaussian kernel width, integer, must be odd. Specifies
%               how far from each pixel the Gaussian convolution, a
%               smoothing filter, is applied.
%       sigma:  Normalized standard deviation for the Gaussian convolution
%               filter.
%       m:      A positive integer exponent that is appied to the local
%               gradient of the gaussian convolution
%       Cm:     Some positive number that is applied to the kernel
%       lam:    Some positive number, a contrast parameter that amplifies
%               or attenuates the gradient.
% diff_im = NonLinAnisoDiff2D(im,num_iter,dt,flag,[input],diff);
%    diff:      *'cent'  Default central differencing, is faster but has a
%                        tendency to produce pixel-scale visual
%                        oscillations.
%               'bkfw'   Backward and forward differencing: this is the
%                        same approach used for simple finite volume heat
%                        transfer calcuations. It requires a few more
%                        calculations, but the result is smoother.
% diff_im = NonLinAnisoDiff2D(im,num_iter,dt,flag,[input],diff,diag)
%    diag:      0       Default, no diagonal differencing
%               1       Diagonal differencing
%
%
% As described in the papers:
% Catte, F.; Lions, P.-L.; Morel, J.-M.; Coll, T., Image Selective
%   Smoothing and Edge Detection by Nonlinear Diffusion, SIAM Journal of
%   Numerical Analysis, 29:1:182-193, 1992.
% Malm,H.; Sparr,G.; Hult,J.; Kaminski, C., Nonlinear Diffusion filtering
%   of images obtained by planar laser-induced fluorescence spectroscopy,
%   Journal of the Optical Society of America, 17:12:2148-256, 2000.
% Perona,P.;Malik,J., Scale-Space and Edge Detection Using Anisotropic
%   Diffusion, IEEE Transactions on Pattern Analysis and Machine
```

```
%   Intelligence, 12:7:629-639,1990.
% Weickert, J., Anisotropic Diffusion in Image Processing, PhD
%   Dissertation, , Universitat Kaiserslautern, Kaiserslautern, 1996.
%
% Created:  August 22, 2007
%           Steven G. Tuttle
%           steven.g.tuttle@gmail.com
%           sgt03002@engr.uconn.edu

im              = varargin{1};
num_iter        = varargin{2};
dt              = varargin{3};
if nargin >= 4,
    flag        = varargin{4};
    if strcmp(flag,'perona'),
        if nargin >=5,
            kappa   = varargin{5}(1);
            option  = varargin{5}(2);
        else
            kappa   = varargin{5}(1);
            option  = varargin{5}(2);
        end
    elseif strcmp(flag,'wckrt'),
        wid     = varargin{5}(1);
        sigma   = varargin{5}(2);
        m       = varargin{5}(3);
        Cm      = varargin{5}(4);
        lam     = varargin{5}(5);
    end
else
    flag        = 'perona';
    kappa       = 10;
    option      = 0;
end
if nargin >= 6,
    diff = varargin{6};
else
    diff = 'cent';
end
if nargin == 7,
    diag = varargin{7};
else
    diag = 0;
end
if nargin > 7,
    disp('Fatal Error: Too many input variables. Please review the help');
    return
end


% Convert input image to double.
im = double(im);
% PDE (partial Differential equation) initial condition.
diff_im = im;
DuNS = zeros(size(im));
DGNS    = DuNS;
```

```
DGEW    = DuNS;
DGNE    = DuNS;
DGSE    = DuNS;
DuNE    = DuNS;
DuSE    = DuNS;
DgNE    = DuNS;
DgSE    = DuNS;

dy      = 1;
dd      = sqrt(2);
% [M,N]   = size(diff_im);
% direct = 0;
if strcmp(diff,'cent'),
    % 2D convolution masks - finite, central differences.
    hNS             = [ 0  1  0;  0  0  0;  0 -1  0];
    hEW             = [ 0  0  0; -1  0  1;  0  0  0];
    hNE             = [ 0  0  1;  0  0  0; -1  0  0];
    hSE             = [-1  0  0;  0  0  0;  0  0  1];
    %gaussimGL       = zeros(size(diff_im));
    % Begin Iteration
*********************************************************
    for kk = 1:num_iter,
        % Finite Differences.
        DuNS        = conv2(diff_im,hNS,'same')/2;
        DuEW        = conv2(diff_im,hEW,'same')/2;
        if diag,
            DuNE    = conv2(diff_im,hNE,'same')/2;
            DuSE    = conv2(diff_im,hSE,'same')/2;
        end
        if strcmp(flag,'perona'),
            Du      = (DuNS.^2 + DuEW.^2 + DuNE.^2 + DuSE.^2).^0.5;
            if option == 0,
                g   = exp(-(Du/kappa).^2);
            else
                g   = 1./(1 + (Du/kappa).^2);
            end
        else
            % Gaussian Convolution Filter
            if wid == 1,
                gaussimGL   = diff_im;
            else
                hg          = fspecial('gaussian',wid,sigma);
                gaussimGL   = conv2(diff_im,hg, 'same');
            end
            % Convolve the Gaussian with the gradient
            DGNS        = conv2(gaussimGL,hNS,'same')/2;
            DGEW        = conv2(gaussimGL,hEW,'same')/2;
            if diag,
                DGNE    = conv2(gaussimGL,hNE,'same')/2;
                DGSE    = conv2(gaussimGL,hSE,'same')/2;
            end
            DG          = (DGNS.^2 + DGEW.^2 + DGNE.^2 + DGSE.^2).^0.5;
            % Calculate gDu & Differentiate gDu
            g       = 1.-exp(-Cm./(DG./lam).^m);
        end
        DgNS        = conv2(g.*DuNS,hNS,'same')/2;
        DgEW        = conv2(g.*DuEW,hEW,'same')/2;
```

```
        if diag,
            DgNE    = conv2(g.*DuNE,hNE,'same')/2;
            DgSE    = conv2(g.*DuSE,hSE,'same')/2;
        end
        % Discrete PDE solution.
        diff_im     = diff_im + dt*(DgNS + DgEW + DgNE + DgSE);
    end
    % End Iteration**********************************************************
elseif strcmp(diff,'bkfw'),
    % 2D convolution masks - backward and forward differencing
    hN      = [ 0  1  0;  0 -1  0;  0  0  0];
    hS      = [ 0  0  0;  0 -1  0;  0  1  0];
    hE      = [ 0  0  0;  0 -1  1;  0  0  0];
    hW      = [ 0  0  0;  1 -1  0;  0  0  0];
    hNE     = [ 0  0  1;  0 -1  0;  0  0  0];
    hSE     = [ 0  0  0;  0 -1  0;  0  0  1];
    hSW     = [ 0  0  0;  0 -1  0;  1  0  0];
    hNW     = [ 1  0  0;  0 -1  0;  0  0  0];
    % Begin Iteration
**********************************************************
    for kk = 1:num_iter,
        % Finite Differences.
        DuN         = conv2(diff_im,hN, 'same');
        DuS         = conv2(diff_im,hS, 'same');
        DuE         = conv2(diff_im,hE, 'same');
        DuW         = conv2(diff_im,hW, 'same');
        if diag,
            DuNE    = conv2(diff_im,hNE,'same');
            DuSE    = conv2(diff_im,hSE,'same');
            DuNW    = conv2(diff_im,hNW,'same');
            DuSW    = conv2(diff_im,hSW,'same');
        end
        if strcmp(flag,'perona'),
            if option == 0,
                gN  = exp(-(DuN/kappa).^2);
                gS  = exp(-(DuS/kappa).^2);
                gW  = exp(-(DuW/kappa).^2);
                gE  = exp(-(DuE/kappa).^2);
                if diag,
                    gNE = exp(-(DuNE/kappa).^2);
                    gSE = exp(-(DuSE/kappa).^2);
                    gSW = exp(-(DuSW/kappa).^2);
                    gNW = exp(-(DuNW/kappa).^2);
                end
            else
                gN  = 1./(1 + (DuN/kappa).^2);
                gS  = 1./(1 + (DuS/kappa).^2);
                gW  = 1./(1 + (DuW/kappa).^2);
                gE  = 1./(1 + (DuE/kappa).^2);
                if diag,
                    gNE = 1./(1 + (DuNE/kappa).^2);
                    gSE = 1./(1 + (DuSE/kappa).^2);
                    gSW = 1./(1 + (DuSW/kappa).^2);
                    gNW = 1./(1 + (DuNW/kappa).^2);
                end
            end
        else
```

```
            % Gaussian Convolution Filter
            if wid == 1,
                gaussimGL   = diff_im;
            else
                hg          = fspecial('gaussian',wid,sigma);
                gaussimGL   = conv2(diff_im,hg, 'same');
            end
            % Convolve the Gaussian with the gradient
            DGN         = conv2(gaussimGL,hN, 'same');
            DGS         = conv2(gaussimGL,hS, 'same');
            DGE         = conv2(gaussimGL,hE, 'same');
            DGW         = conv2(gaussimGL,hW, 'same');
            if diag,
                DGNE    = conv2(gaussimGL,hNE,'same');
                DGSE    = conv2(gaussimGL,hSE,'same');
                DGNW    = conv2(gaussimGL,hNW,'same');
                DGSW    = conv2(gaussimGL,hSW,'same');
            end
            % Calculate g at each face, which a propagation rate
            if diag == 0,
                DG      = (DGN.^2+DGS.^2+DGE.^2+DGW.^2).^0.5;
            else
                DG      =
(DGN.^2+DGS.^2+DGE.^2+DGW.^2+DGNE.^2+DGSE.^2+DGNW.^2+DGSW.^2).^0.5;
            end
            g           = 1.-exp(-Cm./(DG./lam).^m);
            gN          = conv2(g, hN,'same')/2;
            gS          = conv2(g, hS,'same')/2;
            gE          = conv2(g, hE,'same')/2;
            gW          = conv2(g, hW,'same')/2;
            if diag,
                gNE     = conv2(g,hNE,'same')/2;
                gSE     = conv2(g,hSE,'same')/2;
                gNW     = conv2(g,hNW,'same')/2;
                gSW     = conv2(g,hSW,'same')/2;
            end
        end

        % Discrete PDE solution.
        diff_im     = diff_im + dt*(gN.*DuN + gS.*DuS + gE.*DuE + gW.*DuW
)/dy^2;
        if diag,
            diff_im = diff_im + dt*(gNE.*DuNE + gSE.*DuSE + gNW.*DuNW +
gSW.*DuSW )/dd^2;
        end
    end
    % End Iteration*********************************************************
end
```

Nearest Neighbor Interpolation for Velocity Extraction

```
function [ xvel,yvel ] = velgrab( filename,x,y )
%velgrab gives the velocity at the nearest neighbor to a specified point
%   im7only
field=loadvec(filename);
%find the nearest neighbor
xvel=interp2(field.y,field.x,field.vx,y,x,'nearest');
yvel=interp2(field.y,field.x,field.vy,y,x,'nearest');


end
```